

박 사 학 위 논 문

Ph.D. Dissertation

오차 아웃라이어 기법을 이용한 광섬유 FBG 센서
기반의 복합재료 날개 구조물 실시간 충격 모니터링

Novel Error Outlier Method and FBG Sensor Based Real-Time
Low Velocity Impact Monitoring of Composite Wing Structure

2017

Pratik Shrestha (प्रतिक श्रेष्ठ)

한 국 과 학 기 술 원

Korea Advanced Institute of Science and Technology

박 사 학 위 논 문

오차 아웃라이어 기법을 이용한 광섬유 FBG 센서
기반의 복합재료 날개 구조물 실시간 충격 모니터링

2017

Pratik Shrestha

한 국 과 학 기 술 원

항공우주공학과

오차 아웃라이어 기법을 이용한 광섬유 FBG 센서
기반의 복합재료 날개 구조물 실시간 충격 모니터링

Pratik Shrestha

위 논문은 한국과학기술원 박사학위논문으로
학위논문 심사위원회의 심사를 통과하였음

2016년 11월 10일

심사위원장 김 천 곤



심 사 위 원 한 재 흥



심 사 위 원 이 정 룰



심 사 위 원 권 일 범



심 사 위 원 강 동 훈



Novel Error Outlier Method and FBG Sensor Based Real-Time Low Velocity Impact Monitoring of Composite Wing Structure

Pratik Shrestha

Advisor: Chun-Gon Kim

A dissertation submitted to the faculty of
Korea Advanced Institute of Science and Technology in
partial fulfillment of the requirements for the degree of
Doctor of Philosophy in Aerospace Engineering

Daejeon, Korea

November 10, 2016

Approved by



Chun-Gon Kim

Professor of Aerospace Engineering

The study was conducted in accordance with Code of Research Ethics¹⁾.

1) Declaration of Ethical Conduct in Research: I, as a graduate student of Korea Advanced Institute of Science and Technology, hereby declare that I have not committed any act that may damage the credibility of my research. This includes, but is not limited to, falsification, thesis written by someone else, distortion of research findings, and plagiarism. I confirm that my dissertation contains honest conclusions based on my own careful research under the guidance of my advisor.

Dedicated To My

Dearest Dad, Prachanda Man Shrestha

Dearest Mom, Radhika Shrestha

&

Loving Sister, Pratibha Shrestha Baidhya

मूकं करोति वाचालं पङ्क्तुं लङ्घयते गिरिम् ।

यत्कृपा तमहं वन्दे परमानन्दमाधवम् ॥

DAE
20135397

Pratik Shrestha. 오차 아웃라이어 기법을 이용한 광섬유 FBG 센서 기반의 복합재료 날개 구조물 실시간 충격 모니터링. 항공우주공학과. 2017년. 136+vii 쪽. 지도교수: 김천곤. (영문 논문)

Pratik Shrestha. Novel Error Outlier Method and FBG Sensor Based Real-Time Low Velocity Impact Monitoring of Composite Wing Structure. Department of Aerospace Engineering. 2017. 136+vii pages. Advisor: Kim, Chun-Gon. (Text in English)

초 록

복합재료 구조에 저속 충격이 일어나면 대부분 겉표면에서는 육안으로 확인하기 어려운 점이 있어 이에 대한 실시간 구조건전성모니터링 시스템은 민간 및 군용 항공기 구조의 안전성 및 을 확보할 수 있게 한다. 본 연구에서는 충격위치 검출을 위한 오차 아웃라이어 기법을 제안하였고 이 개념을 이용한 다양한 알고리즘을 개발하였다. 1D 배열 fiber Bragg grating (FBG) 광섬유 센서 구성을 이용한 충격 위치 검출 연구를 실물 크기의 Jabiru UL-D 항공기 복합재 주익 날개에 수행되었다. 충격 신호는 고속 FBG 인터로게이터를 이용하여 100 kHz로 취득되었으며 연한 충격과 단단한 충격을 구분할 수 있는 기법을 개발하고 다양한 강성을 갖는 임팩트해머를 이용한 충격의 위치 검출을 통해 검증하였다. 제안된 기법을 이용하여 학습된 높은 강성의 충격에 대한 구분 및 위치 검출이 수행되었고 평균 오차 18.5 mm와 최대 오차 41.5 mm의 결과를 얻었으며 학습된 낮은 강성 충격의 경우 평균 오차 48.5 mm와 최대 오차 111.0 mm의 결과를 보였다. 반면, 학습되지 않은 충격들의 경우 충격 위치 검출의 평균 오차는 80.7 mm 그리고 최대 오차는 217.2-303.1 mm로 나타났다. 본 연구는 제안된 오차 아웃라이어 기법을 이용한 다양한 강성의 학습된 그리고 학습되지 않은 충격에 대한 저속 충격 모니터링의 적합함을 실험을 통해 보였다.

핵심 낱말: 복합재 주익, FBG 센서, 충격 위치 검출, 오차 아웃라이어, 구조 건전성 모니터링

Abstract

Real-time structural health monitoring system (SHM) to monitor low velocity impact on composite structure, which can cause barely visible impact damage, can ensure the safety and structural integrity of civil/military aircraft structure. In this dissertation, a novel error outlier method for localizing impact was proposed and several algorithms using this concept were developed. Impact localization study using 1D array fiber Bragg grating (FBG) sensor configuration were performed on a full scale composite wing of Jabiru UL-D aircraft. Impact signals were sampled using a high speed FBG interrogator at a frequency of 100 kHz. Furthermore, soft and hard-impact classification technique was developed and validated by localizing impacts delivered using trained and non-trained hammer with varying impactor hardness. The proposed method successfully classified and localized the trained hard-impacts with average error of 18.5 mm and maximum error of 41.5 mm, and the trained soft-impacts were localized with average error of 48.5 mm and maximum error of 111.0 mm. Whereas, the various non-trained impact cases were localized with average error of 80.7 mm and the maximum error ranged from 217.2 mm to 303.1 mm. The present study demonstrates the suitability of the proposed novel error outlier method based low velocity impact monitoring of trained or non-trained impact cases.

Keywords: Composite Wing, FBG Sensors, Impact Localization, Error Outlier, SHM

Table of Contents

Table of Contents	i
List of Tables	iii
List of Figures	v
 Chapter 1. Introduction	 1
1.1 Research Background	1
1.2 Literature Survey	4
1.2.1 SHM of Composite Structure	4
1.2.2 SHM using FBG sensors	4
1.2.3 Impact Localization on Composite Structures	5
1.3 Research Objective and Scope	7
 Chapter 2. Data Acquisition and Localization	 9
2.1 Overview of Fiber Optic Sensors	9
2.1.1 Fiber Bragg Grating Sensors	10
2.1.2 FBG Strain Temperature and Sensing Principle	11
2.2 Low Velocity Impact	12
2.3 Real-Time Impact Localization	14
 Chapter 3. 1D Array FBG Sensor Configuration and RMS/Correlation Based Impact Localization	 16
3.1 Correlation Based Reference Database Impact Localization Algorithm	16
3.2 RMS Based Reference Database Impact Localization Algorithm	17
3.3 Composite Plate Impact Localization	18
3.3.1 Materials and Methods	18
3.3.2 Composite Plate 1D and 2D Array Localization Results	20
3.4 Composite Wing Impact Localization	24
3.4.1 Materials and Methods	24
3.4.2 Baseline 1D Array FBG Sensor Configuration Impact Localization	27
3.4.3 Parametric Study of 1D Array FBG Sensor by Varying the Number of FBG Sensors	30
 Chapter 4. Novel Error Outlier Method Based Low Velocity Impact Localization	 36
4.1 Introduction	36
4.2 Development of Outlier Method Based Impact Localization Algorithm	38
4.2.1 Impact Localization on Composite Plate using Outlier Method	39

4.2.2 Error Threshold Set-up	40
4.2.3 Results and Discussions	42
4.3 Enhanced Outlier Method using Euclidean Distance Threshold	45
4.3.1 Overview	45
4.3.2 Impact Localization on Composite Plate	47
4.3.3 Impact Localization on Composite Wing	51
4.3.4 NAO Parametric Study	58
4.3.5 OM1 and OM2 Localization with 'k' Limit	63
4.3.6 Application of OM1 and OM2 Algorithm with k Limit on Complex Wing Surface	70
4.3.7 Results and Discussion	73
4.4 OM3: Simplified Error Outlier Based Localization Algorithm	77
4.4.1 Overview of OM3 Based Impact Localization Algorithms	78
4.4.2 Application of OM3 Algorithms on Complex Wing Test Region	82
4.4.3 Impact Localization Under Simulated Wing Loading Condition	91
4.5 Single Sensor Impact Localization Parametric Study	94
4.5.1 OM2: Single Sensor Parametric Study	94
4.5.2 OM3 with Weighted MAD Threshold Algorithm: Single Sensor Parametric Study	99
4.5.3 Results Comparison and Discussions	103
4.6 Summary	104
Chapter 5. Soft and Hard-Impact Classification and Localization	106
5.1 Introduction	106
5.2 Soft-Body Impact Localization	107
5.2.1 Data Length Parametric Study	108
5.2.2 Localization Performance Comparison	109
5.3 Localization of Impact Delivered with Varying Impactor Hardness	110
5.3.1 Overview	110
5.3.2 Classification of Trained Soft and Hard-Impact Cases	113
5.3.3 Classification and Localization of Non-Trained Impact Cases	114
5.3.4 Impact Localization Using Reduced Data Points	121
5.4 Summary	122
Chapter 6. Conclusions	123
Bibliography	126
Acknowledgements	132
Curriculum Vitae	133

List of Tables

Table 2.1	Impact signal comparison for varying drop heights.	13
Table 3.1	Impact test point coordinates.....	20
Table 3.2	Comparison between 1D and 2D array FBG sensor configuration for impact localization using RMS and Correlation based reference database algorithms.	21
Table 3.3	Impact test points on upper surface of the composite wing.	26
Table 3.4	RMS and correlation based impact localization results.....	27
Table 3.5	Two FBG sensors combination cases.....	31
Table 3.6	Three FBG sensors combination cases.....	31
Table 3.7	Two FBG sensors parametric study optimal sensor combinations.	34
Table 3.8	Three FBG sensors parametric study optimal sensor combinations.....	35
Table 4.1	Impact localization under varying error threshold parameter.....	41
Table 4.2	RMS, correlation, and OM localization results comparison.	43
Table 4.3	Localization results comparison.....	48
Table 4.4	Impact localization on composite panel results comparison.	49
Table 4.5	OM1 and OM2 inner wing localization.	52
Table 4.6	Comparison of composite plate and composite wing OM impact localization results.....	54
Table 4.7	OM1 and OM2 localization performance comparison.....	56
Table 4.8	Comparison of impact localization results obtained using various localization methods.	58
Table 4.9	Optimal localization results based on the NAO parametric study.....	62
Table 4.10	N. of detected locations for 3 and 120 NAO.....	63
Table 4.11	OM with limited number of selected location based impact localization results comparison with RMS and Correlation localization results.	68
Table 4.12	Upper and lower surface impact test point coordinates.....	72
Table 4.13	OM1 and OM2 based predicted impact location coordinates.	73
Table 4.14	Impact localization on upper and lower surface using 1D array sensor configuration.....	75
Table 4.15	Localization results comparison.....	77
Table 4.16	OM3 impact localization results.	83
Table 4.17	OM3 with SD threshold impact localization results.....	85

Table 4.18	OM3 with MAD threshold impact localization results.	86
Table 4.19	OM3 with weighted MAD threshold based impact localization results.	88
Table 4.20	OM localization results summary.	90
Table 4.21	Impact localization under simulated wing loading.	93
Table 4.22	Single FBG sensor parametric study based impact localization results using OM2 algorithm. ...	95
Table 4.23	OM2 impact localization parametric study using error threshold value of 1.0 nm.	97
Table 4.24	OM3 with weighted MAD threshold: parametric study using error threshold value of 1.5 nm.	100
Table 4.25	OM3 with weighted MAD threshold: parametric study using error threshold value of 1.0 nm.	101
Table 4.26	Single sensor based OM vs. cross-correlation localization results comparison.	103
Table 4.27	Impact localization on complex composite structure results comparison.	105
Table 5.1	Soft-body impact localization performance for varying response signal data length.	109
Table 5.2	Summary of soft-impact localization results.	110
Table 5.3	Overview of $Length_h$ and $Length_s$ at various impact test points.	111
Table 5.4	Localization results for Case 1 and Case 2 impact hammer.	118
Table 5.5	Localization results for impact hammer Case 3~6.	119
Table 5.6	Computation time comparison.	122

List of Figures

Figure 1.1	Trend in the usage of composites in aircraft designs [2].	2
Figure 1.2	Illustration of damage occurrence in Airbus 330 horizontal stabilizer [11].	2
Figure 2.1	Classification of fiber optic sensor technology [90].	10
Figure 2.2	Fundamentals of FBG sensor.	11
Figure 2.3	Impact response signal for mass dropped from 50~400 mm.	12
Figure 2.4	Normalized impact response signals obtained for mass dropped from height of 50~400 mm.	13
Figure 2.5	Real-time impact localization.	15
Figure 2.6	Real-time impact visualization GUI program.	15
Figure 3.1	Correlation based reference database impact localization algorithm flow chart.	17
Figure 3.2	RMS based reference database impact localization algorithm flow chart.	18
Figure 3.3	Experimental set-up.	19
Figure 3.4	Illustration of 2D and 1D array FBG configurations on composite plate.	19
Figure 3.5	Composite plate 1D and 2D array FBG sensor impact localization results using RMS based reference database algorithm.	22
Figure 3.6	Composite plate 1D and 2D array FBG sensor impact localization results using correlation based reference database algorithm.	23
Figure 3.7	Jabiru UL-D aircraft.	24
Figure 3.8	Experimental set-up.	25
Figure 3.9	Visualization of impact localization results on composite wing.	28
Figure 3.10	RMS and correlation based reference database impact localization results comparison.	29
Figure 3.11	Parametric study results of 1D array configuration with two FBG sensors.	32
Figure 3.12	Parametric study results of 1D array configuration with three FBG sensors.	33
Figure 4.1	Applications of outlier detection.	36
Figure 4.2	Illustration of error outlier based impact localization concept.	37
Figure 4.3	Outlier based impact localization algorithm flow chart.	38
Figure 4.4	Illustration of impact test points on the composite plate.	40
Figure 4.5	N. of Outliers counted at each of the reference point for Impact Test Point 4.	41
Figure 4.6	Impact Test Point 19: N. of Outliers corresponding to color-mapped figures.	44

Figure 4.7	Visualization of detected range and location.	45
Figure 4.8	OM2 impact localization algorithm flowchart.	46
Figure 4.9	Comparison results of OM1 and OM2.	47
Figure 4.10	OM2 detected location visualization.	49
Figure 4.11	Improved processing time by pre-processing the reference signals.	50
Figure 4.12	Visualization of impact test points on the inner wing section.	51
Figure 4.13	OM1 and OM2 inner wing predicted impact location visualization.	53
Figure 4.14	Error threshold parametric study at Impact Test Point 1 using FBG1 sensor.	55
Figure 4.15	N. of Outliers at each reference point for varying error threshold values using FBG1.	55
Figure 4.16	Predicted impact location using OM1 and OM2 using error threshold value of 1.0 nm.	57
Figure 4.17	OM1 impact localization results for varying NAO.	59
Figure 4.18	OM1 impact localization visualization for varying NAO cases.	59
Figure 4.19	OM2 impact localization results for varying NAO.	60
Figure 4.20	OM2 impact localization visualization for varying NAO cases.	61
Figure 4.21	Visualization of detected impact locations.	64
Figure 4.22	N. of Outliers computed for signals from FBG1 and FBG6 at various Reference Point N.	65
Figure 4.23	Modified Step 3 for limited number of detected location per FBG sensor.	65
Figure 4.24	Modified OM1 and OM2 algorithm flowchart.	66
Figure 4.25	OM1 with k number of selected location impact localization results for varying NAO.	67
Figure 4.26	OM2 with k number of selected location impact localization results for varying NAO.	67
Figure 4.27	Visualization of OM with limited number of selected location based localization results.	69
Figure 4.28	Experimental set-up.	71
Figure 4.29	Schematics of the upper and lower wing surface impact test section.	71
Figure 4.30	Visualization of upper and lower surface impact test points.	72
Figure 4.31	Visualization of impact location detected on wings' upper and lower surface.	74
Figure 4.32	Locations selected for Impact Test Point 10 by OM1 algorithm.	76
Figure 4.33	OM3 impact localization flowchart.	78
Figure 4.34	OM3 with SD threshold impact localization algorithm flowchart.	79
Figure 4.35	OM3 with MAD threshold impact localization algorithm flowchart.	81
Figure 4.36	OM3 with weighted MAD threshold impact localization algorithm.	82
Figure 4.37	OM3 algorithms impact localization results comparison.	89
Figure 4.38	Experimental set-up.	91
Figure 4.39	Lambda variation due to simulated wing loading.	92

Figure 4.40	Visualization of impact localization under simulated wing loading condition.	92
Figure 4.41	Visualization of single FBG sensor parametric study based predicted impact locations.	96
Figure 4.42	OM2: single sensor based predicted impact location visualization.	98
Figure 4.43	OM3 with weighted MAD threshold: single sensor based predicted impact location visualization using error threshold value of 1.5 nm.	102
Figure 4.44	OM3 with weighted MAD threshold: single sensor based predicted impact location visualization using error threshold value of 1.0 nm.	102
Figure 5.1	Hard-body and soft-body impact signal comparison.	106
Figure 5.2	Soft and hard-impact periodogram plot.	107
Figure 5.3	Impact hammer with soft rubber used for reference database construction.	108
Figure 5.4	Soft-body impact test points visualization.	108
Figure 5.5	Visualization of predicted impact locations.	110
Figure 5.6	Comparison of $Length_h$ and $Length_s$	111
Figure 5.7	OM3 with Weighted MAD threshold algorithm for soft and hard-impact localization.	112
Figure 5.8	Overview of training signal selection process.	112
Figure 5.9	Visualization of impact test points for trained and non-trained impact localization study.	113
Figure 5.10	Impact test hammers.	114
Figure 5.11	Trained impact cases classification results.	114
Figure 5.12	Impact hammer with small contact area.	115
Figure 5.13	Impact hammer with large contact area.	115
Figure 5.14	FBG1 response signal for impact hammer with small contact area.	116
Figure 5.15	Periodogram comparison of FBG1 signal for impact hammer with small contact area.	116
Figure 5.16	FBG1 response signal for impact hammer with large contact area.	116
Figure 5.17	Periodogram comparison of FBG1 signal for impact hammer with large contact area.	117
Figure 5.18	Visualization of localization results for Case 1 and Case 2 impact hammer.	118
Figure 5.19	Visualization of localization results for impact hammer Case 3~6.	119
Figure 5.20	Localization performance comparison.	121

Chapter 1. Introduction

1.1 Research Background

Composite materials, consisting of fibrous material in resin matrix, are widely being used as an alternative to conventional materials for primary structures in aerospace structures because of their superior material properties, namely higher specific strength and stiffness, and low weight properties [1]. Development of improved manufacturing technology and reduction in operational costs have also helped in increasing the applicability of composites in aircraft structures. Various research have shown that the usage of composite materials in both civil and military aircrafts have been rising and is expected to continue increasing [2], [3]. Figure 1.1 shows the content of composites in percentage from 1960 to 2015. 50% of the structure of B787 Dreamliner, latest addition to Boeing airliner family, is constructed using composite materials and similarly Airbus's latest aircraft, A350 XWB, constitutes more than 50% composite materials.

Although the composite materials have numerous advantages making them highly desirable for various applications, one of the serious drawback of composite materials is that they are subjected to complex damage characteristics [4], [5] in comparison to isotropic materials. Low velocity impact [6], [7] on composite structure may result in damages which are not easily visible to naked eye. Such kind of damage, known as the Barely Invisible Impact Damage (BVID) [8], [9], can cause degradation of structural properties. Furthermore, failing to identify such kind of damage in time can result in structural failure due to fatigue loading caused by continuous operation of the structure [10]. Aircraft structure can be subjected to BVID as a result of tool-drop, ground vehicles hitting the aircraft, runway debris at take-off etc. One such incident in which the horizontal stabilizer of Airbus A330 collided with ground unit resulting in sub-surface damage, shown in Figure 1.2, was returned to service as the damage was not apparent from the skin surface [11]. This incident highlights the danger of BVID on composite structures. With tremendous growth in the use of composite materials, BVID possess a huge threat to the safety and integrity of aircraft manufactured using composite materials.

Conventionally, aircraft safety and efficiency are ensured through periodic non-destructive testing (NDT) [12]; such as ultrasonic technique [13], infrared thermography [14], X-ray radiography [15]. Though this method is effective for assessing the state of isotropic material such as aluminum it may not be as suitable for composite materials which are subjected to complex damage characteristics. Additionally, NDT of large scale components is a huge challenge, since it requires assembly and disassembly of the structural components for inspection in a lab environment. Occurrence of accidental damage is one of the major drawback of such inspection technique which can occur during the assembly and disassembly procedure. Furthermore, because BVID can occur prior to the scheduled maintenance, a real-time health assessment of the composite structure is needed to monitor low velocity impacts and detect the occurrence of damage due to low velocity impacts.

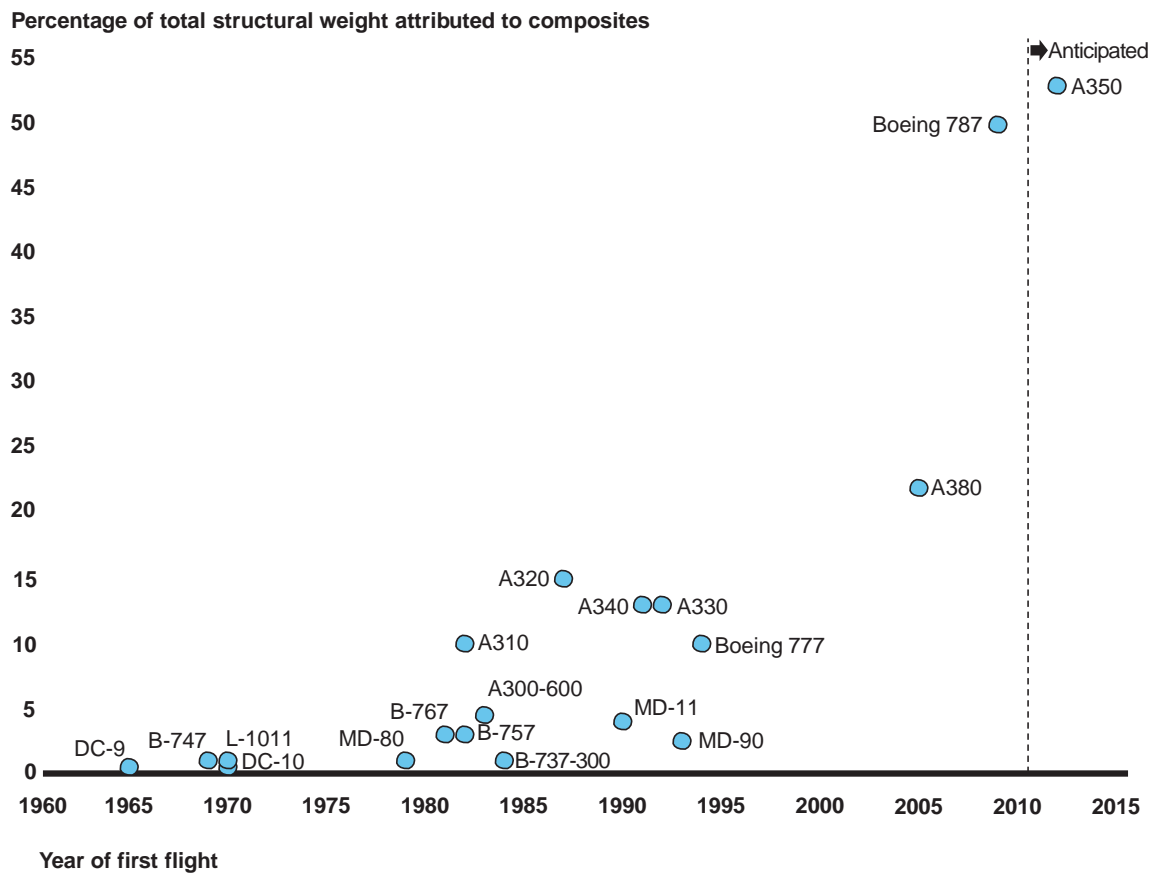


Figure 1.1 Trend in the usage of composites in aircraft designs [2].

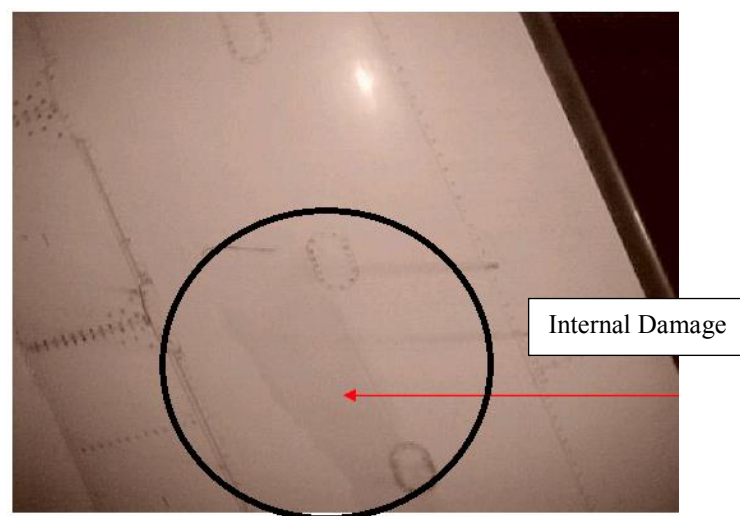


Figure 1.2 Illustration of damage occurrence in Airbus 330 horizontal stabilizer [11].

Smart structure [16], [17] development is the next necessary technological step for a key solution to overcome the challenges faced when using composite materials for aircraft structures. A smart structure can be designed to detect changes in mechanical properties, impacts, damage occurrence, etc. Furthermore, smart structures concept would also be capable of self-repairing any damage that might occur [18], [19]. Preliminary step in realizing such smart structure is the development of a structural health monitoring (SHM) [20], [21] system which consists of attached or embedded sensors in the composite structure to continuously monitor the health state of the structure using an automated system, in contrast to conventional NDT techniques. Application of SHM in aircraft involves operational load monitoring and impact/damage detection and quantification [22]. The key motivations for SHM are optimal use of the structure, performance based maintenance instead of scheduled or periodic maintenance inspection, consequently, reduced labor and human errors since assembly and disassembly of components can be avoided for components with no defect, and constant maintenance costs and reliability compared to conventional structures without SHM [23]. Moreover, SHM can aid in global reduction of accidents.

SHM can be classified into passive or active SHM systems. Passive SHM system involves structure monitoring using embedded or attached sensors. Whereas, active SHM system consists of actuators which can induce structural excitation and sensors which can monitor the structural response. For instance, use of sensors for acoustic emission detection falls into the passive SHM system, and an active SHM system involves use of actuator such as a PZT for ultrasonic wave generation and sensors for monitoring the response signals. Several different types of sensors, such as lead zirconate titanate (PZT), strain gage, fiber optic sensors (FOSs), etc., can be used for aircraft SHM applications [24]–[26]. There is a high interest in FOSs for SHM since they can be embedded in the composite materials. Among the many different FOSs available for SHM, fiber Bragg grating (FBG) sensors have large scale multiplexing capability. FBG sensors are also immune to electromagnetic interference therefore, making them highly desirable for aerospace applications.

In case of composite structures, SHM system needs to be developed in order to detect and localize any impact which can potentially cause BVID damages. It can tremendously help in detecting the impact and the location of the impact, and an automated system can then alert the ground engineers and the pilot of such events for immediate inspection on the specific impact area. Thereby, such SHM system can aid the maintenance engineers in reducing the risk of structure failures. Detecting BVID damage is of utmost concern for composite aircraft structures. Therefore, the overall focus of the present research is on the use of sensing devices for SHM of aircraft structure for low velocity impact detection and localization which can result in damage. The following section presents the researches which have been done on impact/damage detection and damage quantification.

1.2 Literature Survey

1.2.1 SHM of Composite Structure

Key aspects of the aircraft SHM are operational load monitoring and impact/damage detection. Several research on load monitoring have been done. Steve et al. developed a fully autonomous, platform independent, quick and easy to calibrate, mount and remove system which is able to record strain and temperature or acceleration and temperature for a small number of flights using accelerometer, semiconductor gauge, electrical resistance foil gauge, pressure sensor and thermistor [27]. Schmidt et al. performed strain monitoring of Cessna C207A wing spar using fiber optic interferometric strain gauges [28]. Kim et al. [29] implemented and verified FBG based aircraft health and usage monitoring system on Jabiru UL-D light weight aircraft for fatigue life estimation and usage monitoring application through in-flight strain measurement.

Numerous research on impact/damage detection and quantification on composite structures have been done. Sung et al. [30] used wavelet transform to decompose the acoustic emission signal acquired using PZT in time and wavelet scale domain to detect damage due to impact. An et al. [31] presented Integrated Impedance and Guided wave (IIG) damage detection technique using permanently embedded PZT transducers for online monitoring of critical hot spots within a composite airplane wing structure. Applicability of the IIG damage detection technique has been shown on the bolt loosening and debonding in the wing segment under varying temperature and loading conditions. Chul et al. [32] proposed a new damage detection technique using PZT network for detection of delamination in composite plate by comparing pitch catch Lamb wave signals. The proposed damage detection technique extracts the anti-symmetric mode, which slows down when it passes through delamination area, in order to identify any delamination occurrence in the composite structure. Ogisu et al. [33] developed a hybrid sensor system that can detect the elastic waves launched from the PZT actuator using a high-speed and high-accuracy FBG sensor for damage monitoring. They demonstrated data acquisition of elastic wave generated by PZT with a frequency of 300 kHz using a fiber sensor bonded 5 cm apart from the PZT on an aluminum sheet and CFRP cross-ply laminate for damage monitoring purpose.

1.2.2 SHM using FBG sensors

Although there are several types of sensors available for SHM application, FOSs have emerged as the sensor of choice. In the late 1960's, grid of optical fibers embedded in the structure for damage detection was proposed by Kinard et al. [34]. A grid of optical fibers embedded in the structure detects damage due to crack opening or delamination which breaks the light path through the optical fiber. Subsequently, several research demonstrated the structural damage detection capability of optical fibers based SHM system [35]–[37]. Since then many different optical fiber sensors, such as FBG, intensity-based optical fibers, interferometric sensors based on Fabry-Perot, Mach-Zehnder, etc., have been developed [38]–[40] for SHM applications. Optical fiber

sensors can be used for SHM of composite structures for application such as low velocity impact damage detection [41], impact localization [42], delamination detection [43]–[45], load monitoring [46], transverse cracks detection [47], [48], fatigue induced damage detection [49], etc. PZT actuator/FBG sensor hybrid system was developed by Ogisu et al. for damage monitoring of aircraft structure [33].

FBG sensors due to their inherent signal stability and multiplexibility are highly desirable for SHM applications. Several studies have been performed to demonstrate the feasibility of using FBG sensors for SHM application. Takahashi et al. [50] proposed and tested SHM technology based on strain mapping of composite airframe structures throughout their life cycle using FBG sensors. They investigated detection of debonding using FBG sensors through the strain monitoring test of CFRP skin-stiffener panel and showed that 5 mm debonding damage on the stiffener can be detected using FBG sensors. Similarly, Kang et al. [51] presented strain monitoring of a filament wound composite tank using FBG sensors during hydrostatic pressurization and demonstrated the use of FBG sensor system for large structures which require large number of sensor arrays. Mrad et al. [52] performed load monitoring and damage detection using FBG sensors and found that the results were similar compared to the conventional resistive strain gages.

Furthermore, the FBG sensor was able to detect acoustic waves generated by the PZT, 1.32 m away from the FBG. Panopoulou et al. [53] presented SHM of aerospace composite structure using real-time dynamic strain measurements from FBG sensors. Wavelet transform was used for feature extraction and artificial neural network for identifying the damage size and location. Lee et al. used a re-coated FBG connected in an FBG sensor system as a longitudinal strain sensor for the measurement of dynamic strain [54]. They experimentally demonstrated the capability of FBG to detect flutter through the wind tunnel test of the subscale smart wing. Chandler et al. presented an FBG sensors based on-line SHM and fire detection system [55]. Kressel et al. presented load monitoring based SHM system for the composite tail booms of a UAV using an array of embedded FBG sensors to reduce periodic grounding of airborne platforms and to develop condition-based maintenance [56]. Lee et al. [57] applied strain-free mobile FBG ultrasonic receiver, which can detect acousto-ultrasonic wave without any complex feedback controlling technique to follow up the strain-induced Bragg wavelength change, to detect damage on CFRP plate.

1.2.3 Impact Localization on Composite Structures

As mentioned in the Section 1.1, despite of several advantages of composite materials, rising trend in composite materials usage is also of concern since, upon impact, these materials are subjected to complex damage characteristics [4], [5] which occur internally. Composite structures' transverse damage resistance is weak due to a lack of through thickness reinforcement. Consequently, barely visible impact damage (BVID), matrix cracking and delamination can be caused by a low velocity impact, resulting in significant reduction in

the strength of the structure [58]–[60]. Aircraft structures are vulnerable to BVID from low velocity impact events, which can occur from unexpected impact loads as a result of mishandling during ground operation, or foreign object impact during operation and maintenance. Therefore, automated detection and localization of low velocity impact occurrence on aircraft structure can detect and localize low velocity impacts, and attract the attention of aircraft engineers to conduct a detailed inspection of impact regions for possible BVID due to the impact.

Many research on impact localization techniques have also been done. In general, for anisotropic material the time of impact detected by different sensors has been used to estimate the impact point through triangulation method [61]. However, in case of composite material, in which the wave propagation varies according to the fiber direction, alternative techniques have to be used to localize the impact location; these include the time reversal method [62], [63], stress waves analysis using wavelet transforms [64]–[66], minimization of a non-linear objective function or error function [67], and reference database methods [68]–[70]. Maseras et al. [71] collected impulse strain response using PZT sensor and localized impact using neural network which used standard multi-layer perceptron trained with backpropagation learning rule. Ruiz et al. [72] proposed and successfully demonstrated the partial/least square projection to latent structures to predict the impact location on aircraft structures. Park et al. [73] computed the correlations between the impact response and the impulse response function in the training data using time reversal concept to localize impact on composite wing structure. Yuan et al. [74] proposed a near-field multiple signal classification impact localization algorithm and used it to localize impact on aircraft composite oil tank.

Several impact localization studies have reported the use of FBG sensors for low velocity impact monitoring. Park et al. [75] estimated the impact location on composite panel using neural network algorithm and strain signals from FBG sensors. Frieden et al. approximated the impact location through interpolation of a reference data set consisting of arrays of arrival time delays and known location [76]. Impact localization algorithm developed by Kirkby et al. [77] calculated the difference in time-of-flight of ultrasonic Lamb waves at three surface-mounted sensors to estimate the impact location. Cristobal et. al., performed localization of low velocity impact using strain amplitude information from FBG sensors [78], [79]. Park et al. used neural network algorithm to estimate the location of impact on stiffened composite plate [80]. Jang et al. demonstrated the possibility of using RMS based impact localization algorithm and 2D array FBG sensors for impact detection under dynamic loading [81]. Kim [82] utilized cross-correlation based impact localization technique to localize impacts on testbed aircraft wing structure, and also investigated the effect of sensor configuration and grid size on impact localization performance.

Most of the impact localization research have been done using SHM system with sensors arranged in 2D array configuration. Utilizing such systems on large scale structure such as an aircraft will require large number

of sensors. As a result, the data acquisition process for aircraft SHM will become complex and costly. Therefore, a versatile approach to simplify the impact localization procedure is needed to enable real world application of such SHM system.

1.3 Research Objective and Scope

The background and literature study presented in the earlier sections shows that there is high interest in SHM of composite structure in order to ensure its integrity and reliability. Such interest in SHM of composite material can be attributed to; a) considerable increase in the use of composite material in the aerospace industry which is expected to continue as such in the future and b) composite materials susceptibility to BVID due to low velocity impact. Based on the literature survey, the following areas of research can be determined to be of high interest for SHM of composite material; a) development of a quick and effective real-time impact detection and localization technique which can help to localize impacts on the composite component of the aircraft and alert the pilot and engineers of such impact for further detailed inspections, b) identify solutions to one of the major challenge related with SHM of large scale structures, such as an aircraft, i.e. it requires a sizeable number of sensors in order to perform SHM leading to higher cost and increased complexities in acquisition and processing of the data, and c) classification and localization of low velocity soft and hard-impacts.

Therefore, the objective of this research is to develop and demonstrate a novel error outlier based impact localization method to localize low velocity impact on complex composite structures. The present research focuses on application of 1D array FBG sensor configuration and novel impact localization technique based on error outliers for impact monitoring of complex composite aircraft wing structure. Furthermore, the present research also focuses on classification and localization of impacts with varying impactor hardness using error outlier based impact localization algorithm consisting of soft and hard-impact reference databases. The scope of this dissertation is organized in the following order:

Chapter 1: The research background, related literature studies and the objective and scope of the present research are introduced.

Chapter 2: Overview of fiber optic sensors, FBG theory and its fabrication techniques, and its temperature and strain sensing principles are presented. Subsequently, the low velocity impact response signals are compared for varying impact force. Finally, overview of the real-time impact localization using the FBG sensor, high-speed interrogator and the impact localization GUI developed using MATLAB are introduced.

Chapter 3: In this chapter, the 1-dimensional (1D) array FBG sensor configuration together with correlation and root mean squared (RMS) error based reference database impact localization algorithms is proposed for impact localization of impact test points on composite wing using high speed FBG interrogator. Firstly, the RMS and correlation based impact localization algorithms were used to compare the localization

results between 1D array sensor configuration and 2D array sensor configuration. Then the impact localization on the upper surface of the composite wing is done by attaching the FBG sensors on the composite wing in 1D array configuration. Additionally, parametric study of 1D array FBG sensor configuration is performed to realize the possibility of using optimized number of FBG sensors, and optimal sensor location to localize the impact on the Jabiru UL-D composite wing.

Chapter 4: Novel impact localization technique based on error outlier assessment is proposed for impact signal data processing and localization application on composite wing structure. Firstly, the error outlier based impact localization algorithms were developed and used to localize impact on composite plate. The key parameters such as error threshold value were studied to determine their effect on the localization performance. Subsequently, user-set distance threshold method and statistically determined threshold methods for selecting the likely impact locations were investigated. In case of user set distance threshold, the error outlier based impact localization algorithm with Euclidean distance threshold was used. Then, three different statistical threshold methods for likely impact location selection were investigated; 1) Standard Deviation threshold method, 2) Median Absolute Deviation threshold method and 3) weighted Median Absolute Deviation threshold method. The proposed error outlier based impact localization methods were validated by localizing impacts on composite wing structure. Additionally, impact localization was also done for impact delivered on wing under simulated wing loading condition. Finally, single sensor impact localization parametric study was performed to determine the feasibility of using the proposed error outlier based impact localization algorithms to localize low velocity impact using a single FBG sensor.

Chapter 5: Firstly, the feasibility study of localizing soft-impacts using the error outlier based impact localization algorithm was done. Subsequently, soft and hard-impact classification technique was proposed and integrated into the error outlier based impact localization algorithm. Finally, the proposed method's classifying and localizing capability were examined by localizing trained and non-trained impact delivered using several impact hammers with varying impactor hardness.

Chapter 6: Conclusions are presented.

Chapter 2. Data Acquisition and Localization

2.1 Overview of Fiber Optic Sensors

FOS are highly favorable for SHM purposes as they are light in weight, small in size, require low-power, free from electromagnetic interference and have high sensitivity. FOS can be divided into two categories; a) intrinsic sensors and b) extrinsic sensors [39], [40], [83]. In extrinsic sensors the interaction between the light and the measurement quantity takes place outside the fiber. Whereas, FOS in which the sensor action takes place within the fiber is known as the intrinsic fiber optic sensor. FOS can also be categorized into three groups, namely interferometric sensors, distributed sensors and grating based sensors. Figure 2.1 shows the sensors which fall into these three categories.

Interferometer involves the superposition of two or more beams or modes which can be configured using two single-mode fibers, one single-mode fiber, one multimode fiber or one elliptical-core highly birefringent fiber [84]. Fabry-Perot and SOFO interferometric sensors are the two widely used interferometric sensors. SOFO interferometric sensor have been widely implemented for SHM of many different civil structures because of their temperature insensitivity, high precision and stability. However, they are not suitable for impact damage detection because of their slow response time. Fabry-Perot sensor has high resolution and is compact. Therefore, it is suitable for embedding into composite structure to monitor temperature, strain and pressure. However, it lacks in multiplexing capability.

Distributed optical fiber sensor utilizes the properties of optical fiber to make simultaneous measurement of both the spatial and temporal behavior of a measurand field [85]. Optical time-domain reflectometry (OTDR) is the most typical intrinsic distributed fiber optic sensor based on Rayleigh scattering [86]. Second kind of distributed optical fiber sensor is based on the Raman scattering and therefore it is known as the Raman optical time-domain reflectometry (ROTDR) [87]. Lastly, Brillouin optical time-domain reflectometry (BOTDR) is the Brillouin scattering based fiber optic distributed sensor [88].

Finally, grating based sensors consists of UV-inscribed in-fiber gratings. Grating based sensors are inexpensive to manufacture, immune to EM interference, lightweight, small in size and self-referent with a linear response. FBG is one of the widely used grating-based sensors. Among various FOS available, there is high interest in the use of FBG for SHM due to several advantages over other FOS [89]. FBG sensors have inherent signal stability and are suitable for multiplexing. Furthermore, since FBGs are immune to power fluctuations since its sensing procedure relies on monitoring shifts in the optical wavelength, FBG has quasi-point sensing and non-uniform strain field measurement capability. FBG sensors were used for the present research, therefore, the working principle of FBG is discussed in the subsequent section.

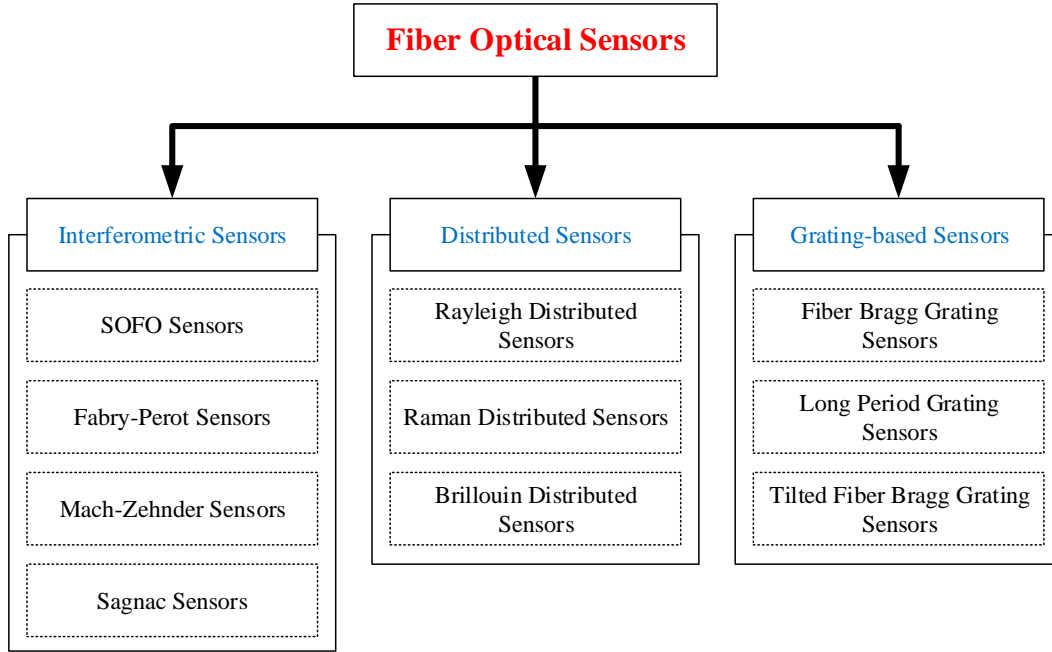


Figure 2.1 Classification of fiber optic sensor technology [90].

2.1.1 Fiber Bragg Grating Sensors

Hill et al. reported the photosensitive mechanism in a germanium doped silica fiber leading to the development of fiber grating by exposing the photosensitive core using a single-mode argon-ion laser source at 488 nm or 514.5 nm [91], [92]. Meltz et al. further improved the grating fabrication technique by exposing the core through the side of the cladding to a coherent UV two-beam interference pattern with a wavelength selected to lie in the oxygen-vacancy defect band of Germania near 244 nm [93]. FBG sensors consists of grating photo-inscribed into a silica fiber with periodic variation in the refractive index. The periodic modulation of the grating's refractive index can be done using the free-space two-beam holographic method or the diffractive phase mask technique [40], [91]–[94].

Holographic method [40] fabricates FBG using UV laser beam, from a UV source with good temporal and spatial coherence, split into two components which are recombined at the fiber to create interference pattern. Major challenge of holographic technique is its interference fringe spacing and placement is highly sensitive to the system's optical alignment. Therefore, it requires the system to be highly stable and free from external vibrations. The diffractive phase mask method [40] for FBG fabrication can overcome the limitation posed by holographic technique. Refractive index modulation can be photo-imprinted using a phase mask, a diffraction element that can be used to form an interference pattern laterally with the light beams which are spatially phase modulated and diffracted [95]. Furthermore, phase-mask method is good for mass FBG production at low cost and this technique works with inexpensive low spatial and temporal coherence lasers. In general, the grating lengths are within the range of 1~20 mm and can provide peak reflectivity near 100%.

2.1.2 FBG Strain Temperature and Sensing Principle

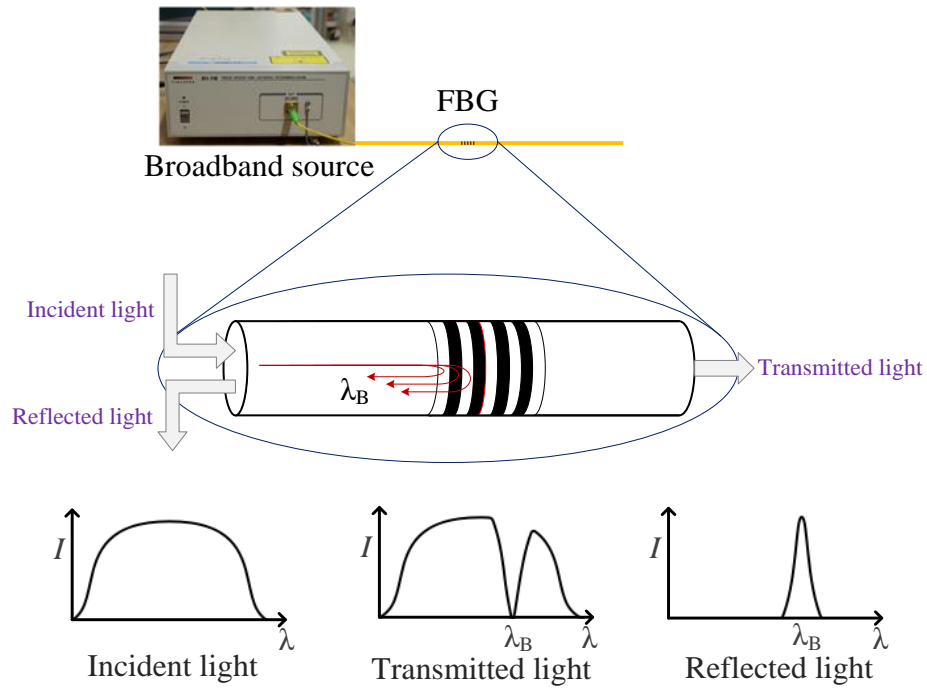


Figure 2.2 Fundamentals of FBG sensor.

When light source is transmitted from the spectral broadband source through the fiber, the grating acts as a wavelength filter which reflects certain wavelengths of light and allows the remaining wavelengths to pass through. Figure 2.2 shows the fundamental working principle of the FBG sensor. The reflected wavelength can be calculated using the Bragg wavelength

$$\lambda_B = 2n_e \Lambda \quad (1)$$

where, n_e is the grating's effective refractive index and Λ is the grating period.

Bragg wavelength is sensitive to any changes in strain or temperature as a result of physical elongation of the FBG sensor which causes changes in the grating pitch and the fiber index due to photoelastic effects. Utilizing the Bragg wavelength sensitivity, the strain response can be obtained using FBG sensor.

The changes in temperature or strain shift can be measured using the shift in Bragg wavelength

$$\Delta\lambda_B = \lambda_B [(\alpha + \xi)\Delta T + (1 - p_e)\varepsilon] \quad (2)$$

where, α is the coefficient of thermal expansion, ξ is the thermal-optic coefficient, T is the temperature, ε is the strain value, and p_e is the photo-elastic constant. The photo-elastic constant is calculated using

$$p_e = \left(\frac{n_e^2}{2} \right) [p_{12} - \nu(p_{11} + p_{12})] \quad (3)$$

where, ν is the Poisson's ratio and, p_{11} and p_{12} are the strain-optic constants.

Finally, the strain can be calculated using Equation 4, assuming there is no change in the temperature. Similarly, changes in the temperature can be obtained using Equation 5, assuming no strain is applied to the FBG sensor.

$$\varepsilon = \frac{1}{1 - p_e} \cdot \frac{\Delta\lambda_B}{\lambda_B} \quad (4)$$

$$\Delta T = \frac{1}{\alpha + \xi} \cdot \frac{\Delta\lambda_B}{\lambda_B} \quad (5)$$

One major limitation of FBG sensors is that they are sensitive to both temperature and strain. This limitation can be overcome by using reference gratings along the gratings that are in thermal contact with the structure and free from local strain changes for compensating the changes in Bragg wavelength due to changes in temperature.

2.2 Low Velocity Impact

In this research, the impacts on the composite structures were delivered using impact hammer. Although, the impact force for each impact case can vary, it was found that only the amplitude of the impact response signal changes with changes in the impact velocity/force. Figure 2.3 shows the impact response signals acquired when a 45.42 g spherical mass was repeatedly dropped eight times from heights ranging from 50 mm to 400 mm, with 50 mm interval, on the upper surface of the composite wing. For impact velocity ranging from 0.99 m/s to 2.8 m/s, it can be observed that the overall impact response signal remains the same while the amplitude increases with increase in the drop height.

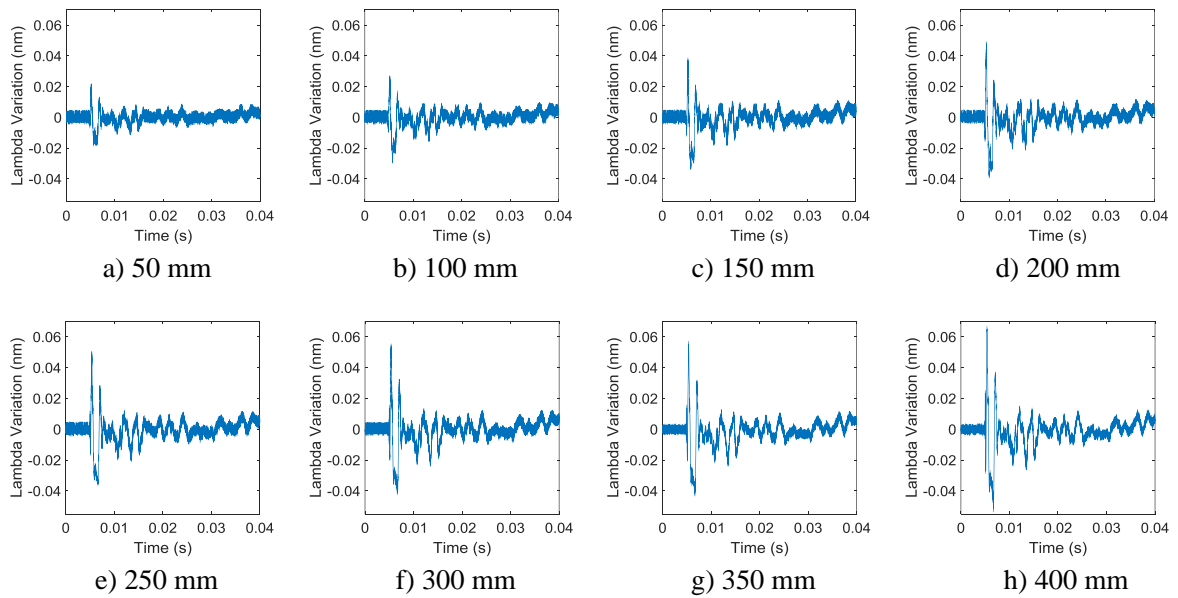


Figure 2.3 Impact response signal for mass dropped from 50~400 mm.

Such difference in the response signal due to changes in impact force can be overcome by normalizing the response signal. In Figure 2.4 the time-shifted normalized response signals, of all eight impact cases, which resulted in the maximum correlation coefficient are presented. In Figure 2.4, it can be seen that the normalized impact response signal obtained by dropping the spherical mass from 50 mm compared to each of the normalized impact response signals obtained by dropping the spherical mass from 100 mm to 400 mm signals are similar. The correlation values computed for each of the drop height are tabulated in Table 2.1. Moreover, even though the impact velocities are different, the resulting average correlation coefficient was 0.92. Therefore, the signal normalization process can help to minimize the variance in obtained impact signal due to varying impact force.

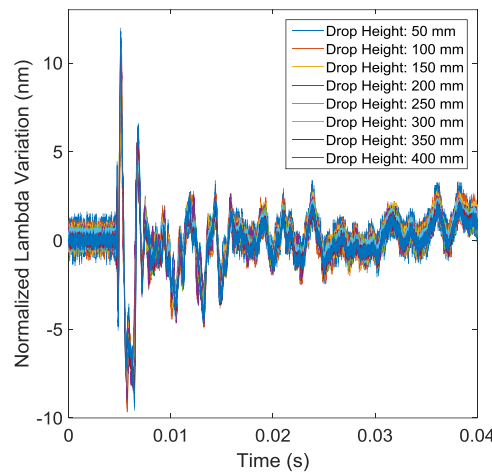


Figure 2.4 Normalized impact response signals obtained for mass dropped from height of 50~400 mm.

Table 2.1 Impact signal comparison for varying drop heights.

Signal Similarity Comparison with 50 mm Drop Height Impact Response Signal								
Drop Height (mm)	50	100	150	200	250	300	350	400
Impact Velocity (m/s)	0.99	1.4	1.71	1.98	2.21	2.42	2.62	2.8
Correlation Value	1.00	0.92	0.93	0.92	0.93	0.93	0.92	0.91

2.3 Real-Time Impact Localization

The real-time impact localization is achieved in three stages:

- 1) continuous impact monitoring,
- 2) impact data detection and data acquisition, and
- 3) data processing in order to predict the impact location.

The real-time impact localization procedure is illustrated in Figure 2.5. Continuous impact monitoring is done using attached/embedded optical fiber line, consisting of multiplexed FBG sensors, on the structure which is connected to the FBG interrogator. For the experiments presented in this dissertation, a high speed FBG interrogator SFI-710 (FIBERPRO Inc., Korea) [96] was used for continuous impact monitoring, impact detection, data acquisition and impact localization. The SFI-1710 consists of a superluminescent laser diode (SLD) broadband light source, and with wavelength accuracy of 40 pm. This high-speed interrogator has a single channel with FC/APC type connector through which it can sample the signals from the FBG sensors at maximum sampling rate of 100 kHz. It can detect wavelength ranging from 1530 nm ~ 1560 nm, its operating temperature ranges from -5°C to 50°C. If an impact is detected during the continuous monitoring process, then 0.20 s long data is acquired at 100 kHz frequency. The acquired data consists of 0.05 s data before the impact event and 0.15 s data after the impact event.

The third stage of the real-time impact localization, impact location prediction, is done using the impact localization algorithm developed using MATLAB software. Additionally, a GUI software was developed to get the signals acquired using the high speed interrogator, SFI-710, to the impact localization algorithm and then visualize the predicted impact location. The real-time impact localization visualization GUI software is presented in Figure 2.6. The real-time impact localization is done through the GUI in four steps. Firstly in Step 1 shown in Figure 2.6, the folder location where the impact signals are stored by the FBG interrogator is selected. Then the continuous monitoring can be started by clicking on the 'Start' button, Step 2 is shown in Figure 2.6. In Step 3, as long as there is no any impact on the structure being monitored, 'In Progress' status will be shown in the status window inside the 'Output Panel'. When an impact occurs, the status window inside the 'Output Panel' will change to 'Impact Detected' and the impact signals acquired by the FBG interrogator are fed to the impact localization algorithm. Finally, in Step 4, the signals acquired by the FBG interrogator will be processed using the impact localization algorithm and the predicted impact location, 'x-coordinate' and 'y-coordinate', will be shown in the 'Output Panel' > 'Impact Location', and simultaneously the impact location will be visualized in the graph. After the low velocity impact localization is completed the software will resume to continue monitoring for impact on the structure; the status will be changed to 'In Progress'. This process will be repeated by the software until the 'Stop' button is pressed.

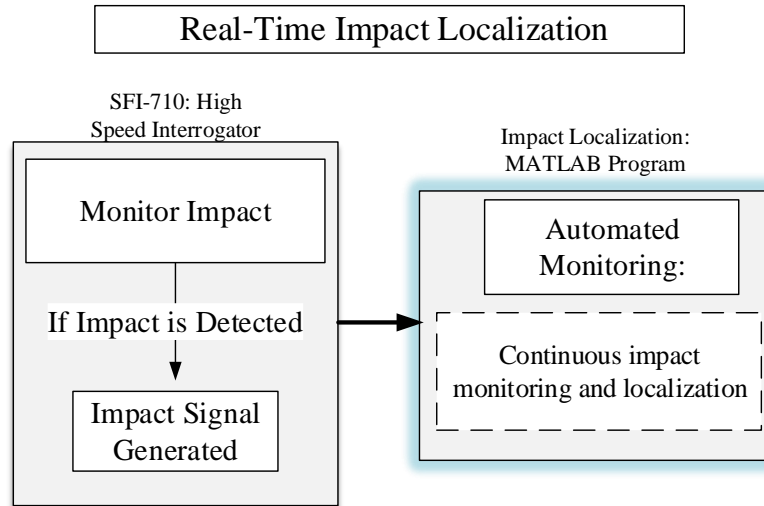


Figure 2.5 Real-time impact localization.

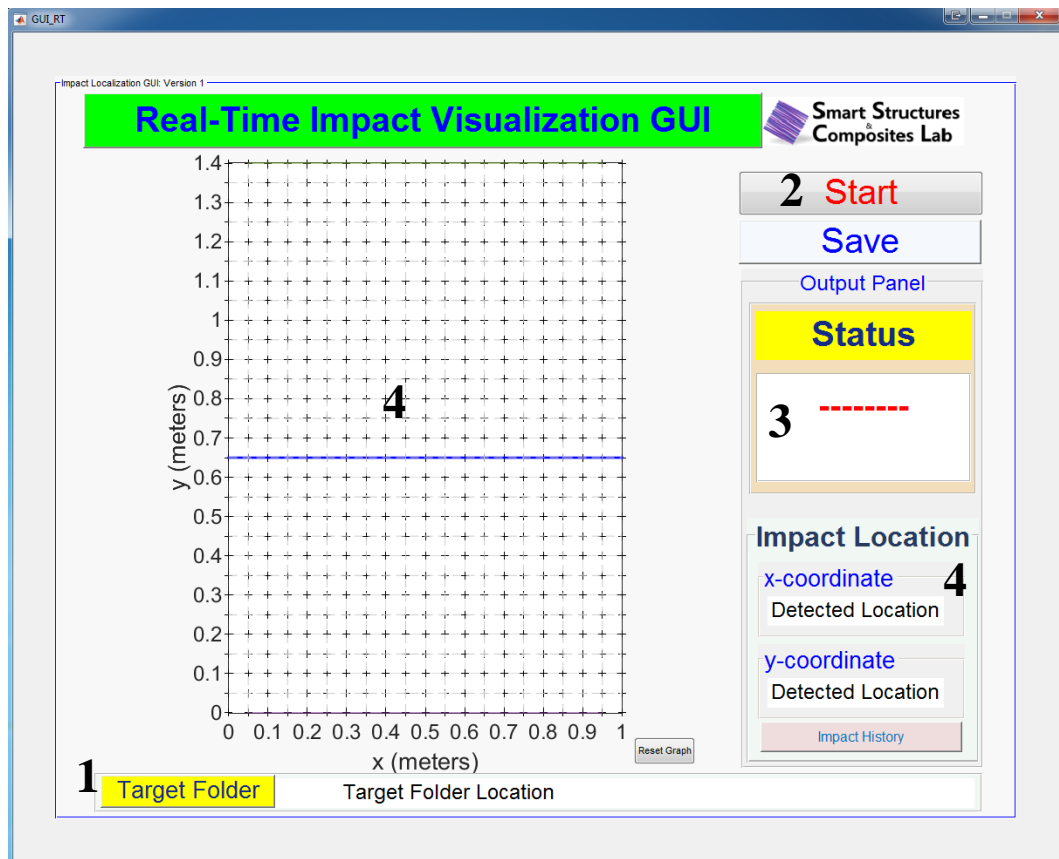


Figure 2.6 Real-time impact visualization GUI program.

Chapter 3. 1D Array FBG Sensor Configuration and RMS/Correlation Based Impact Localization

In this chapter, low velocity impacts were localized using 1D array FBG sensor configuration, and correlation and RMS [97] impact localization algorithms based on reference database impact localization concept. A reference database based impact localization algorithm utilizes training data, which are the pre-acquired reference signals, containing the information of the impact signals at training grid points to estimate the location of any impact point. The working principle of correlation and RMS based impact localization algorithm is based on comparison of the random impact signal with all the reference signals available in the database and finally estimating the location of the impact by determining the reference signal which is most similar to the impact signal.

3.1 Correlation Based Reference Database Impact Localization Algorithm

In the case of correlation based impact localization algorithm, the correlation coefficient between the reference signal, S_{ref} , and the random impact signal, S_{ran} , were calculated using Equation (6). The correlation method used for the reference database impact localization algorithm compares the two signals, reference signal and the random impact signal, and outputs the correlation value from -1 to 1. If the signals are similar to each other the correlation value tends to be closer to 1 and dissimilar signals will have low or negative correlation value.

$$Corr = \frac{\sum (S_{ref} - \overline{S_{ref}})(S_{ran} - \overline{S_{ran}})}{\sqrt{\sum (S_{ref} - \overline{S_{ref}})^2 (S_{ran} - \overline{S_{ran}})^2}} \quad (6)$$

Figure 3.1 shows the correlation based impact localization algorithm flow chart. In this algorithm firstly the data normalization of the reference signal, $S_{ref(n,i)}$, acquired by FBG sensor 'i' at training reference grid point 'n' and random impact signal, $S_{ran(i)}$, acquired by FBG sensor 'i' were done using min-max normalization method [98] to scale the signal data between 0 and 1. Subsequently, the correlation coefficient was calculated between the random impact signal, $S_{ran(i)}$, and all the reference impact signals, $S_{ref(n,i)}$, of the test specimen. In order to improve the localization results the normalized reference signal was time-shifted, $S_{ref(t_{n,i})}$, by altering the index of the signal starting point from $t=1$ to $t=200$ in increments of $t=1$, and the correlation value between each of the time-shifted reference impact signal and the random impact signal, $S_{ran(i)}$, was computed. Among all the correlation value computed at each reference point, between the time-shifted reference impact signals and the random impact signal, the maximum correlation coefficient was used for further impact localization procedure. Finally, for each sensor the impact location was determined to be the location of the reference point

whose reference impact signal was most similar to the random impact signal, corresponding to the maximum correlation value. Finally, the location of the impact was estimated by calculating the mean of the impact locations detected by each FBG sensor.

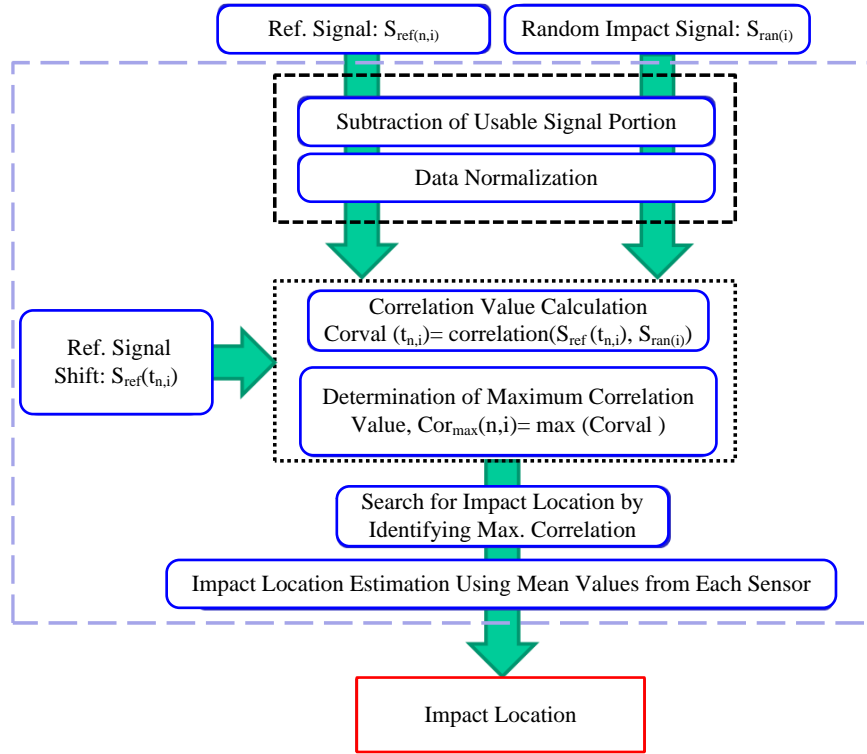


Figure 3.1 Correlation based reference database impact localization algorithm flow chart.

3.2 RMS Based Reference Database Impact Localization Algorithm

Impact location estimation procedure using RMS based reference database impact localization algorithm is illustrated using flow chart shown in Figure 3.2. RMS based 1D array impact localization algorithm works similarly as the correlation based impact localization algorithm discussed in Section 3.1. In contrast to correlation method, the normalization of reference signal, $S_{ref(n,i)}$, acquired by FBG sensor ‘i’ at training reference grid point ‘n’ and random impact signal, $S_{rand(i)}$, acquired by FBG sensor ‘i’ were done by dividing by maximum value [98] of signal $S_{ref(n,i)}$ and $S_{rand(i)}$, respectively.

$$R_{ij} = \sqrt{\frac{\sum_{k=1}^n (S_{ref,k} - S_{rand,k})^2}{n}} \quad (7)$$

RMS based impact localization algorithm calculates the RMS error between the reference and random impact signal using Equation (7). Similar to the correlation based impact localization algorithm, RMS error was calculated between each of the time-shifted reference impact signal, $S_{ref(t_n,i)}$, by altering the index of the reference signal starting point from $t=1$ to $t=600$ in increments of $t=1$, and the random impact signal, $S_{rand(i)}$. Then

the minimum RMS error value among all the RMS errors calculated between the time-shifted reference impact signal for each reference point and the random impact signal was used to determine the impact location. The algorithm searches for the location of the grid point with minimum mean RMS error results and the impact location detected by each FBG sensor corresponds to the grid point location which has the most similar impact waveform as that of the random impact signal. Lastly, the algorithm approximates the impact location by calculating the mean of the location found by each FBG sensor.

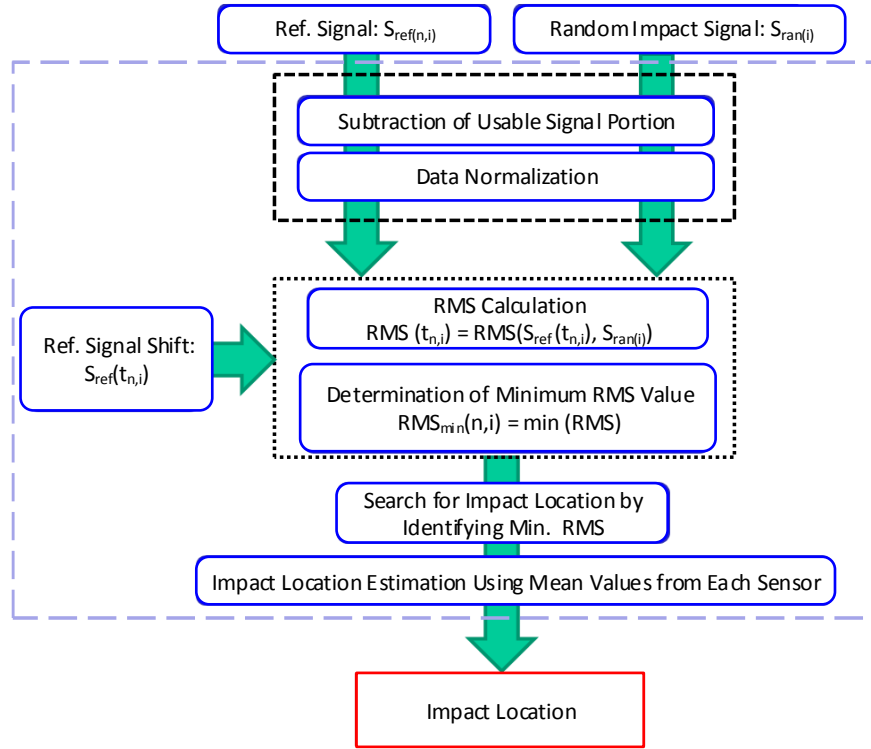


Figure 3.2 RMS based reference database impact localization algorithm flow chart.

3.3 Composite Plate Impact Localization

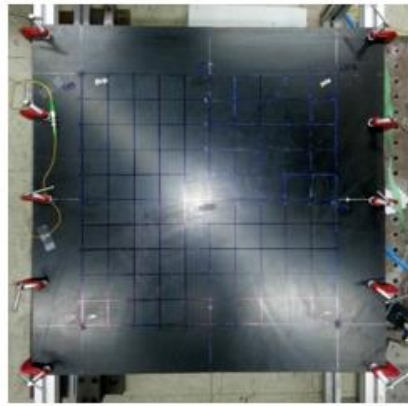
3.3.1 Materials and Methods

The impact localization performance comparison between the 2D and 1D array FBG sensor configuration was performed using a 690 mm × 690 mm composite plate structure. The test specimen is a quasi-isotropic composite with stacking sequence $[45/90/-45/0_2/-45/0/90/0/-45/0/45/90/-45/0]_s$ and with a thickness of 4.7 mm. The two edges of the composite plate were bounded by a total of 10 point clamps. 2D and 1D FBG array configuration impact localization experiments were performed in 500 mm × 500 mm test section of the composite flat plate. Figure 3.3 shows the experimental set-up of the present experiment.

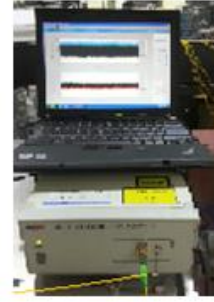
Present impact localization experiment on the composite plate was performed using acrylic coated FBG sensors (FIBERPRO Inc., Korea [96]) with 10 mm grating length attached to the surface of the composite using cyanoacrylate adhesive. The 2D array FBG sensor configuration consists of four multiplexed FBG sensors, with

center wavelength of about 1532 nm, 1536 nm, 1538 nm and 1552 nm, attached on the bottom surface of the composite plate, one FBG at each of the four corners of the impact coverage area, as shown in Figure 3.4 (a).

The grating of FBG sensors were aligned at 45° angle facing towards the center of the composite plate. The 1D array FBG sensor configuration used for the impact localization experiment consists of two multiplexed FBG sensors, with center wavelength of about 1535 nm and 1541 nm, attached at the bottom surface of the composite plate, one FBG at each of the two mid-sections of the edges of the coverage area. Figure 3.4 (b) shows the 1D array FBG sensor configuration used for the present experiment. Both of the FBG sensors used for the 1D array FBG configuration set-up were oriented at 45° angle.

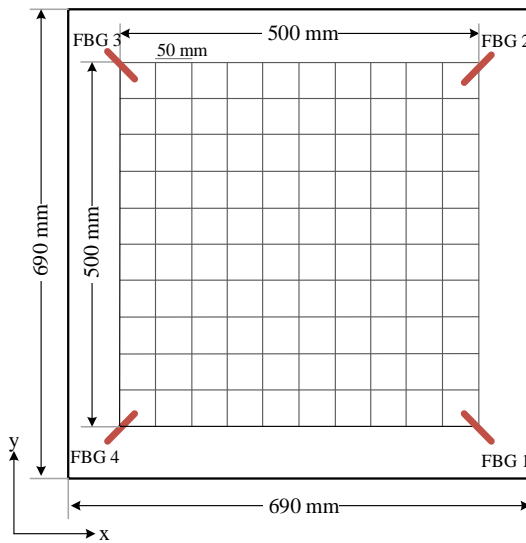


a) Composite plate test specimen

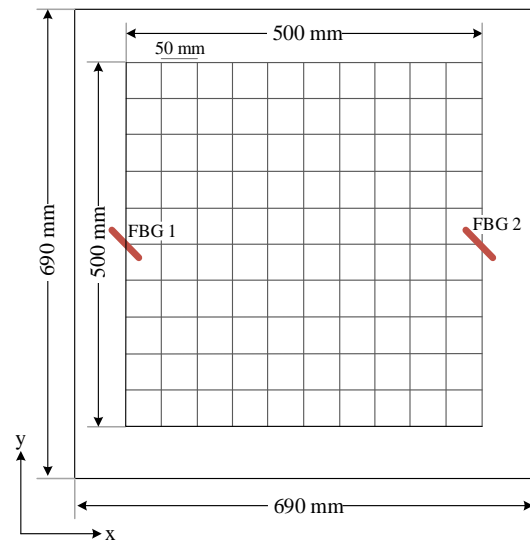


b) Data acquisition system

Figure 3.3 Experimental set-up.



a) 2D FBG array, 4 sensors configuration



b) 1D FBG array, 2 sensors configuration

Figure 3.4 Illustration of 2D and 1D array FBG configurations on composite plate.

Table 3.1 Impact test point coordinates.

Impact Test Point Location on Composite Plate					
N.	x (mm)	y (mm)	N.	x (mm)	y (mm)
1	25	25	11	325	275
2	25	325	12	325	425
3	25	475	13	375	475
4	75	275	14	425	175
5	100	75	15	475	125
6	125	325	16	475	275
7	225	275	17	450	225
8	250	475	18	500	25
9	250	125	19	500	125
10	325	225	20	500	225

The training data for the reference database impact localization algorithms were acquired from 121 training points, which are 50 mm apart from each other. FBG sensor signal acquisition was done using high speed FBG interrogator, SFI-710 (FIBERPRO Inc., Korea) consisting of a superluminescent laser diode (SLD) broadband light source, and with wavelength accuracy of 40 pm [96]. The impact on the composite structure was induced using impact hammer and the signals from all the sensors were sampled at frequency of 100 kHz. Table 3.1 shows the coordinates of the 20 impact test points on the composite plate used for impact localization performance comparison between 2D and 1D array FBG sensor configurations.

3.3.2 Composite Plate 1D and 2D Array Localization Results

Using the training data collected from the composite plate, impact location of 20 different random impacts were localized by means of RMS and correlation based reference database impact localization algorithms. Comparison between the results obtained between 1D and 2D array FBG sensors are tabulated in Table 3.2 and visualized in Figure 3.5 and Figure 3.6.

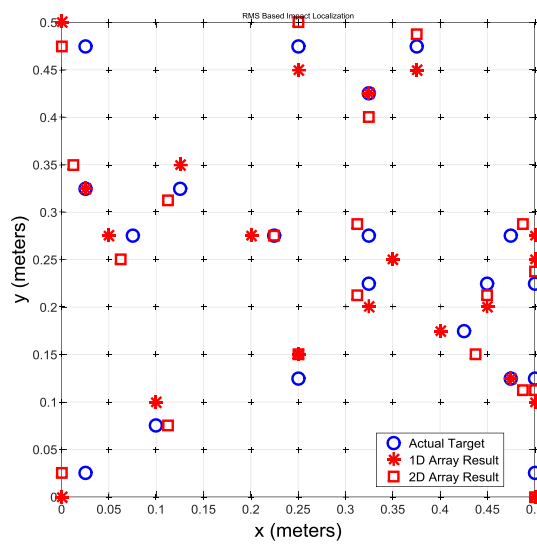
Table 3.2 shows the maximum localization error, average localization error and its standard deviation (SD). In the case of RMS based impact localization, the difference between 1D and 2D array FBG sensor configuration average localization error was found to be less than 4.0 mm, whereas using correlation based impact detection technique resulted in a difference of about 6.0 mm. Both of the impact localization method estimated the impact test points within the range of 35.4 mm for 1D array FBG configuration and 28.0 mm for 2D array FBG configuration, respectively.

Table 3.2 Comparison between 1D and 2D array FBG sensor configuration for impact localization using RMS and Correlation based reference database algorithms.

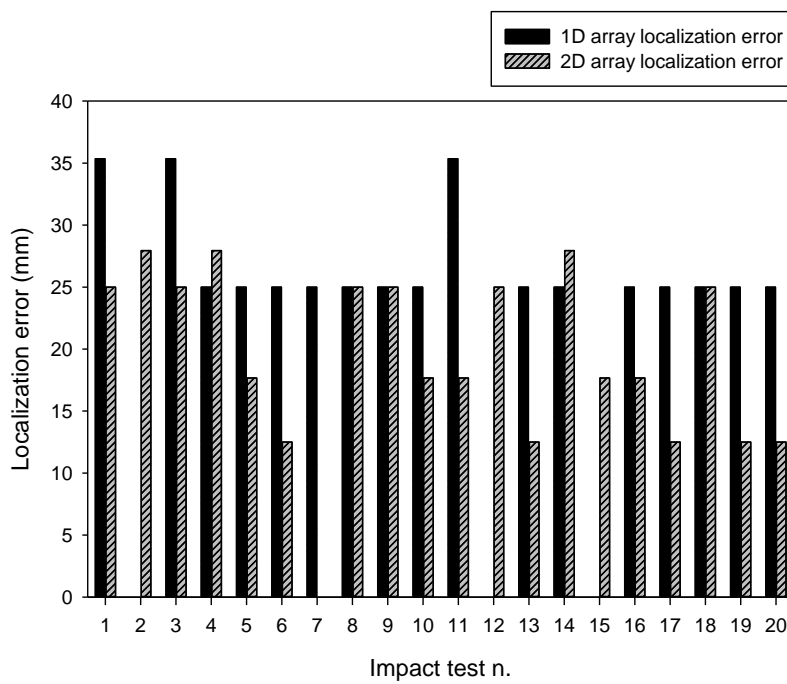
	RMS Method		Correlation Method	
	1D Array FBG	2D Array FBG	1D Array FBG	2D Array FBG
Maximum Error (mm)	35.4	28.0	35.4	28.0
Average Error (mm)	22.8	19.2	26.3	20.1
SD (mm)	10.2	7.2	7.5	7.1

From the present results, it can be observed that the impact location of the impact test point detected by RMS and correlation based impact localization algorithms are very similar to each other. Therefore, it can be concluded that the obtained results are reliable and either of the algorithms can be used for impact location detection purpose for simple composite structure SHM purposes. Furthermore, the experimental results demonstrate that 1D array FBG configuration is as effective as the 2D array FBG configuration for impact localization.

Utilizing the 1D array configuration coupled with the reference database based impact localization algorithm can help reduce the number of sensors required for SHM purpose. Thereby, this configuration also helps to lessen the complexity involved in data acquisition process and decreases the related costs. Therefore, there is a great scope for the implementation of 1D array sensor for SHM of large scale structures such as aircraft, spacecraft, bridges, etc.

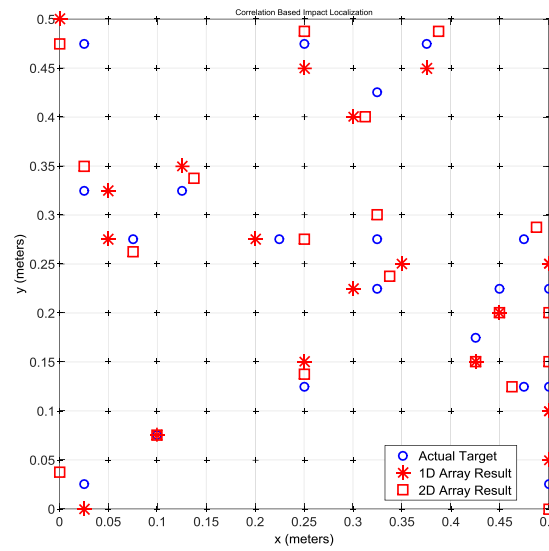


a) RMS based reference database impact localization visualization

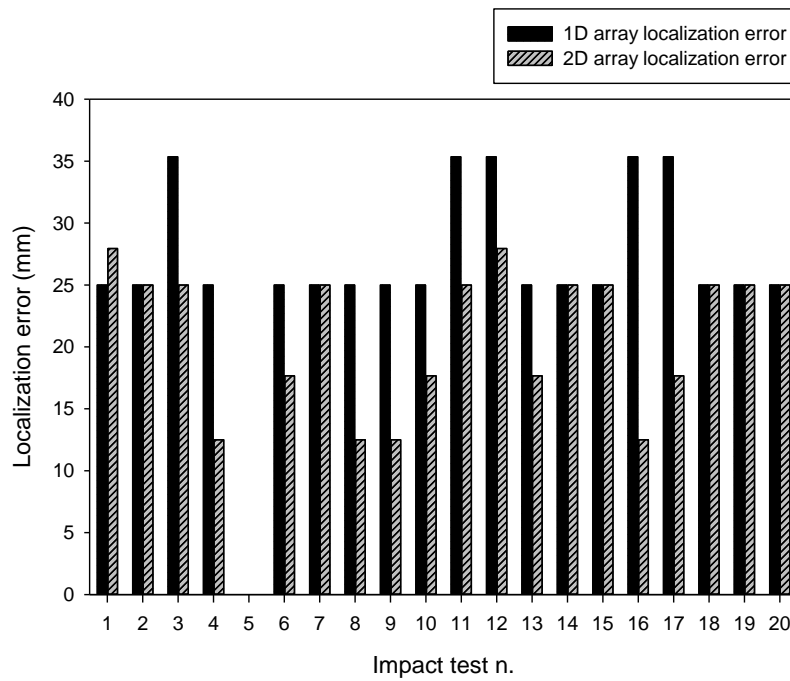


b) RMS based reference database impact localization error

Figure 3.5 Composite plate 1D and 2D array FBG sensor impact localization results using RMS based reference database algorithm.



a) Correlation based reference database impact localization visualization



b) Correlation based reference database impact localization error

Figure 3.6 Composite plate 1D and 2D array FBG sensor impact localization results using correlation based reference database algorithm.

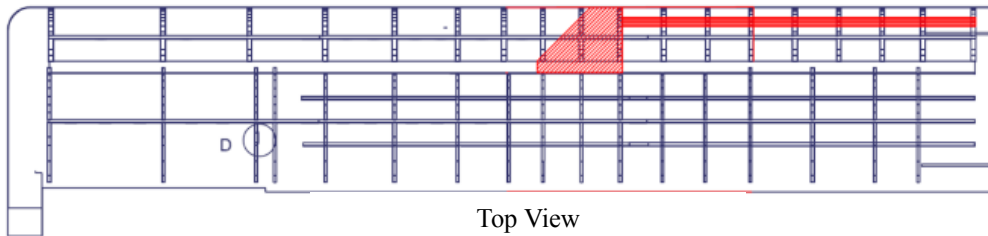
3.4 Composite Wing Impact Localization

3.4.1 Materials and Methods

Jabiru UL-D aircraft's (Jabiru Aircraft Pty Ltd, Australia) composite wing, shown in Figure 3.7, was used to implement and test the 1D array FBG sensor configuration SHM system for impact localization experiment. The schematics of the composite wing specimen and the experiment set-up used for the 1D array impact localization are shown in Figure 3.8.



a) Jabiru UL-D aircraft



b) Jabiru UL-D half-span wing structure illustration

Figure 3.7 Jabiru UL-D aircraft.

The wing structure of Jabiru UL-D consists of a strut, therefore the wing section is categorized into two regions which are separated along by the cross-section fixed with strut: inner region, from the fuselage to the cross-section of the wing where one end of the strut is attached, and the outer region, from the cross-section of the wing where the strut is joined till the tip of the wing.

Six multiplexed acrylic coated FBG sensors (FIBERPRO Inc., Korea), with center wavelength of about 1532 nm, 1535 nm, 1538 nm, 1541 nm, 1544 nm and 1547 nm, were attached 600 mm apart from each other on the upper surface of the composite wing using cyanoacrylate adhesive. All of the FBG sensors were attached on the wing surface with 45° angle orientation. Impact localization was performed on a 600 mm by 600 mm test area on the upper surface of the inner and outer wing region in order to investigate the differences in impact

localization performance in these two regions. In case of the inner wing region the impact test was performed from 600 mm to 1200 mm from the root and for the outer wing region the impact test was done from 2400 mm to 3000 mm from the root.

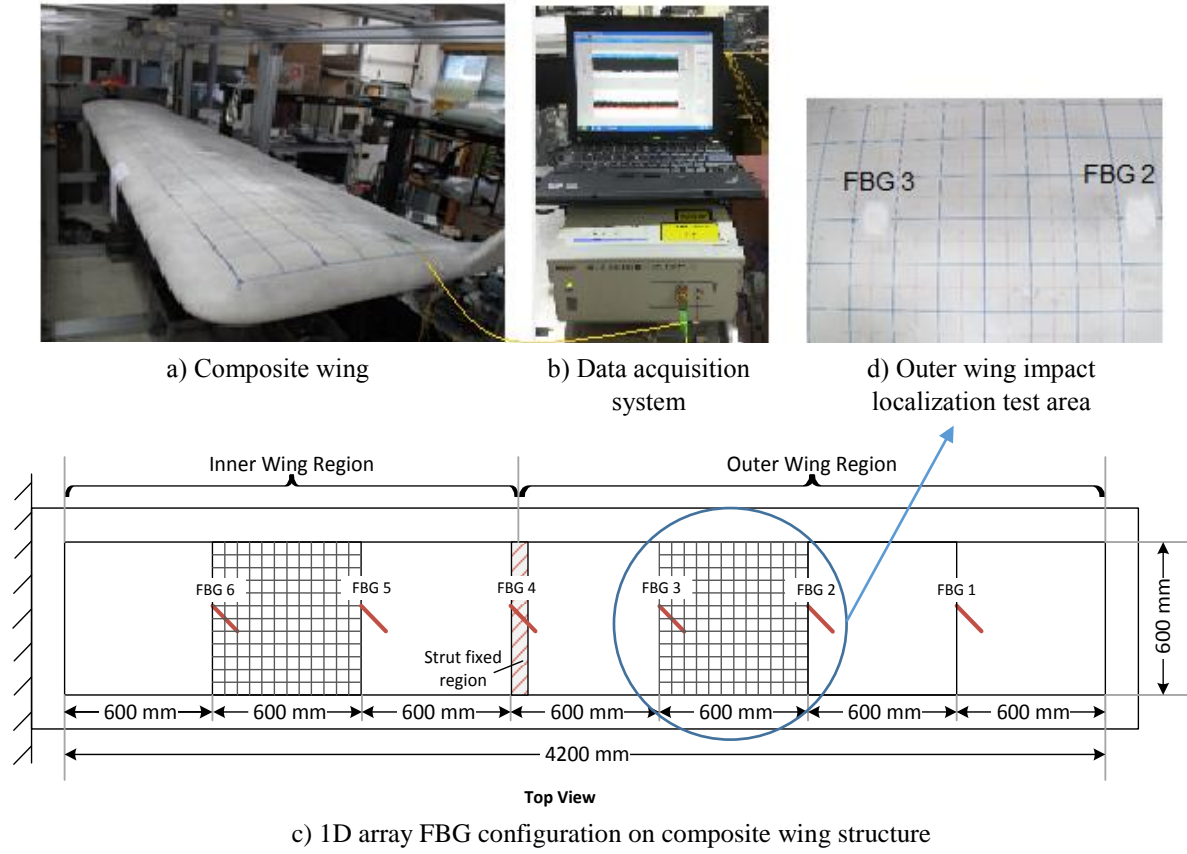


Figure 3.8 Experimental set-up.

Training data for the RMS and correlation based reference database localization algorithms were collected from 169 reference points from both the inner and outer wing section. The reference points used for obtaining the training data are 50 mm apart from each other. Impact localization of 22 random impact cases, 11 impact test points on each inner and outer wing section were performed. Impact signals obtained using the FBG sensor were sampled at 100 kHz using high speed FBG interrogator, SFI-710 (FIBERPRO Inc., Korea). The coordinates of the impact test points used for the impact localization test is shown in Table 3.3.

In the subsequent section, the baseline impact localization study done using 1D array FBG sensor configuration with six FBG sensors to localize the impact location on composite wing structure is presented. Next, the impact localization capability of 1D array FBG sensor configuration with reduced number of FBG sensors along with reference database impact localization algorithm is demonstrated through parametric study of 1D array FBG sensor configuration done by varying the number of FBG sensors from three FBG sensors to two FBG sensors, respectively.

Table 3.3 Impact test points on upper surface of the composite wing.

a) Inner Wing Section		
Impact Test Point	x (mm)	y (mm)
1	625	25
2	625	225
3	725	425
4	850	275
5	875	575
6	975	175
7	975	375
8	1000	125
9	1050	325
10	1125	150
11	1175	375

b) Outer Wing Section		
Impact Test Point	x (mm)	y (mm)
1	2425	25
2	2425	225
3	2525	425
4	2650	275
5	2675	575
6	2775	175
7	2775	375
8	2800	125
9	2850	325
10	2925	150
11	2975	375

3.4.2 Baseline 1D Array FBG Sensor Configuration Impact Localization

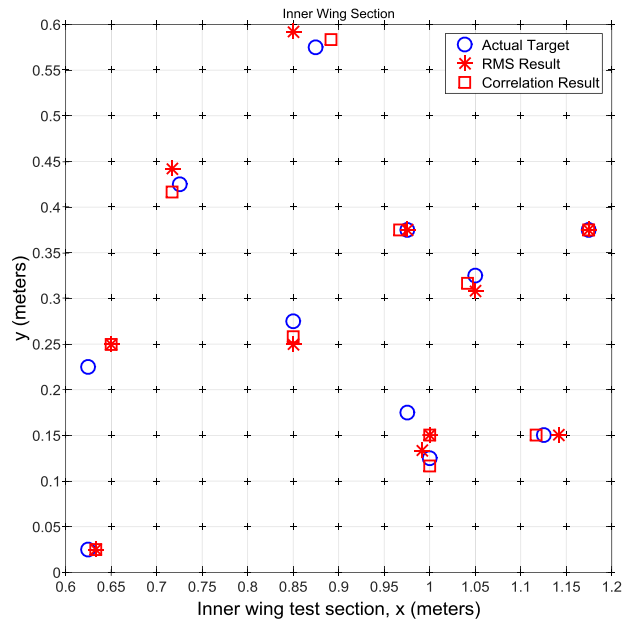
Baseline impact location detection of 22 random points, tabulated in Table 3.3, was done using the impact signals obtained from all six FBG sensors of the 1D array FBG sensor configuration attached on the upper surface of the composite wing. The impact localization results are visualized in Figure 3.9 and the localization errors are presented in Figure 3.10.

Despite of the complex structure form of the composite wing, using the impact signal obtained from the 1D array FBG configuration, the RMS and correlation based impact localization algorithms estimated the location of all the random points with localization error less than the training grid size of 50.0 mm. The localization error of the estimated location of the impact test points are presented in Table 3.4. Similar trend among inner and outer wing average localization error can be observed i.e., the larger localization error values can be seen for the outer wing case than for the inner wing case, when either RMS or correlation based impact localization method was used for impact location prediction.

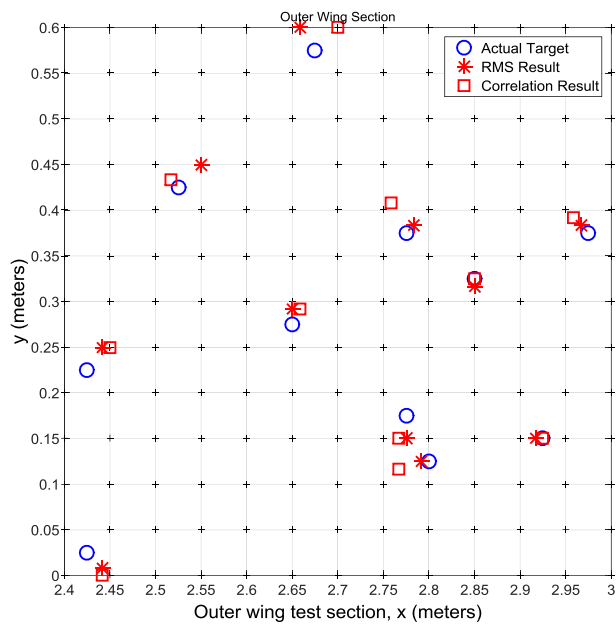
The localization error for both inner and outer wing impact tests was estimated to about 35 mm from the actual impact point. For the inner wing region, the RMS and correlation based impact localization result had an average localization error of 18.0 mm and 14.8 mm with standard deviation of 12.0 mm and 10.3 mm, respectively. Whereas, the outer wing region had average localization error of 14.8 mm and 22.5 mm with standard deviation of 10.7 mm and 12.8 mm, respectively.

Table 3.4 RMS and correlation based impact localization results.

	RMS Based Localization		Correlation Based Localization	
	Inner Wing	Outer Wing	Inner Wing	Outer Wing
Maximum Error (mm)	35.4	35.4	35.4	37.3
Average Error (mm)	18.0	19.5	14.8	22.5
SD (mm)	12.0	10.3	10.7	12.8

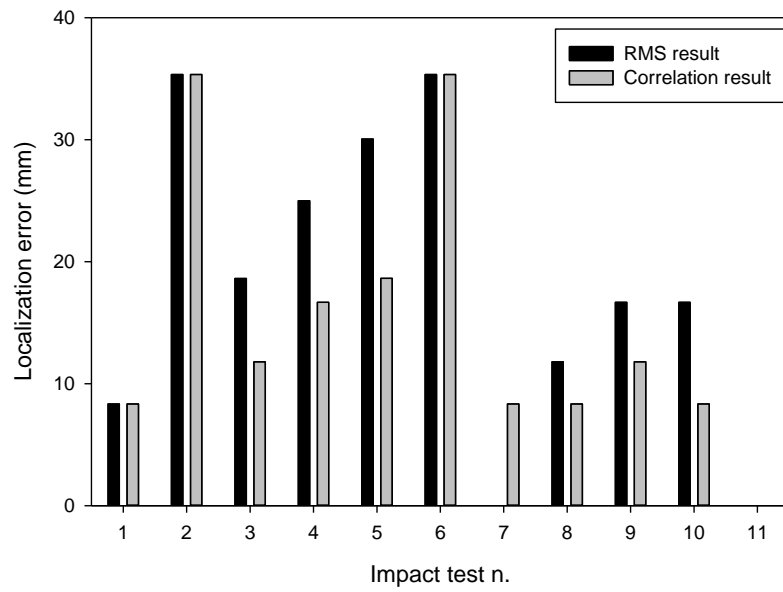


a) Inner wing section detected impact location visualization

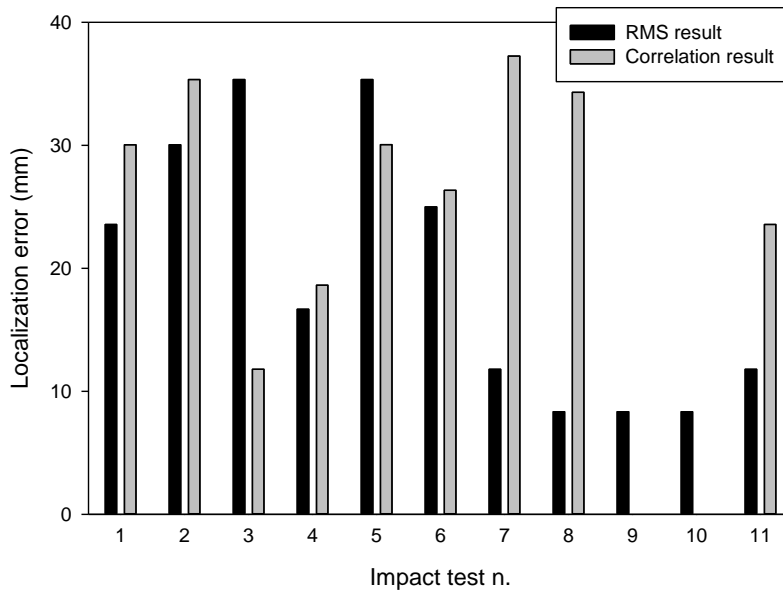


b) Outer wing section detected impact location visualization

Figure 3.9 Visualization of impact localization results on composite wing.



a) Inner wing section localization error



b) Outer wing section localization error

Figure 3.10 RMS and correlation based reference database impact localization results comparison.

3.4.3 Parametric Study of 1D Array FBG Sensor by Varying the Number of FBG Sensors

The present parametric study was done to demonstrate the possibility of localizing impact test points using fewer number of FBG sensors for 1D array FBG sensor configuration together with reference database impact localization algorithm. Among the six sensors attached on the upper surface of the wing, parametric study was performed firstly by using a combination of two FBG sensors and followed by three FBG sensors. The optimal sensor combination was determined based on the localization results of the impact test points listed in Table 3.3.

Parametric study of 1D array configuration with two FBG sensors was done using combinations of FBG sensors shown in Table 3.5. Similarly, for impact localization with 1D array configuration with three FBG sensors, parametric study was done using combinations of FBG sensors shown in Table 3.6. Localization results of the parametric study done using 1D array configuration with two and three FBG sensor combination cases are shown in Figure 3.11 and Figure 3.12, respectively. Optimal sensor combination was determined by searching for sensor combinations which gives the location of all the 22 impact test points with localization error of less than the grid size of 50.0 mm.

In case of parametric study of 1D array configuration with two FBG sensors, it was found that using RMS based impact localization technique, 6 different sensor combinations could localize all the 22 impact test points with localization error of less than 50.0 mm. Using sensor combination number 3, 4, 10 or 11 resulted in the maximum localization error of 35.4 mm, and 50.0 mm when combination number 7 and 8 were used. Optimal sensor combinations for the 1D array configuration with two FBG sensors are shown in Table 3.7. However, correlation based localization resulted in maximum localization error larger than the grid size. For the 22 random impact cases, among the 15 different combinations of FBG sensors, combination number 1 and 14 were found to be the best combination cases with maximum localization error of 55.9 mm.

1D array configuration with three FBG sensor parametric study shows that the number of optimal sensor combination increases to 14 combinations out of 20 cases for RMS based reference database localization. The best sensor combinations are 8, 9, 14 and 17 with maximum localization error of 35.4 mm. The other 10 optimal combinations cases resulted in maximum localization error of 48.6 mm. The optimal three sensor combinations found through the parametric study for 1D array configuration with three FBG sensors are tabulated in Table 3.8.

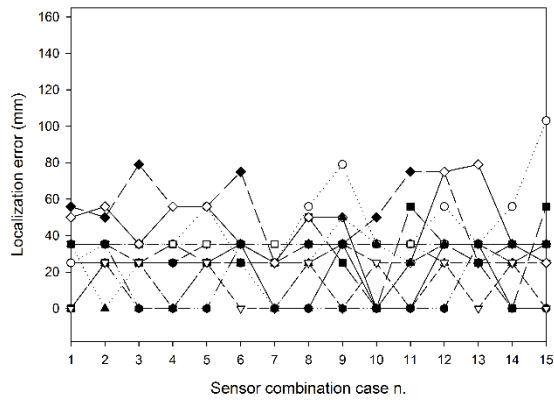
Correlation method based impact localization performed better with three FBG sensors based parametric study. At least 2 optimal combinations cases of FBG sensors were determined, case n., 3 and 4 respectively. Using either of these two combination cases, the maximum localization errors of all the random impact tests were limited to 48.6 mm.

Table 3.5 Two FBG sensors combination cases.

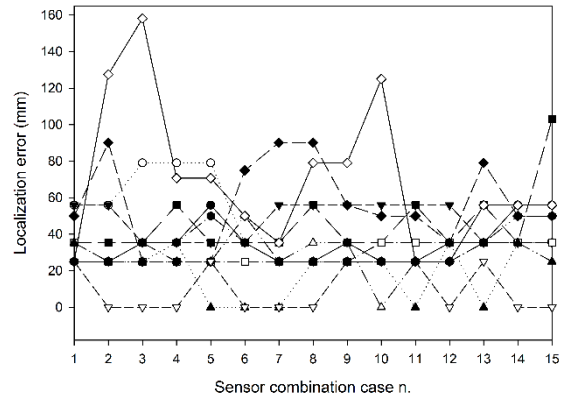
Case N.	Sensor Combination (FBG)	
1	1	2
2	1	3
3	1	4
4	1	5
5	1	6
6	2	3
7	2	4
8	2	5
9	2	6
10	3	4
11	3	5
12	3	6
13	4	5
14	4	6
15	5	6

Table 3.6 Three FBG sensors combination cases.

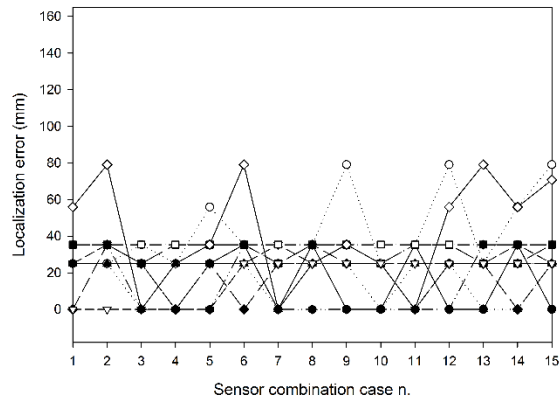
Case N.	Sensor Combination (FBG)			Case N.	Sensor Combination (FBG)		
1	1	2	3	11	2	3	4
2	1	2	4	12	2	3	5
3	1	2	5	13	2	3	6
4	1	2	6	14	2	4	5
5	1	3	4	15	2	4	6
6	1	3	5	16	2	5	6
7	1	3	6	17	3	4	5
8	1	4	5	18	3	4	6
9	1	4	6	19	3	5	6
10	1	5	6	20	4	5	6



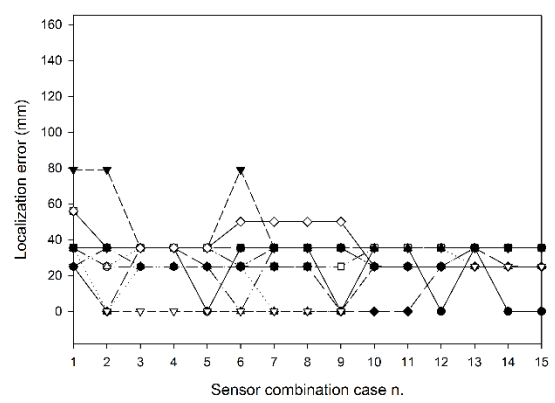
a) Inner wing section parametric study using correlation algorithm



b) Outer wing section parametric study using correlation algorithm



c) Inner wing section parametric study using RMS algorithm



d) Outer wing section parametric study using RMS algorithm

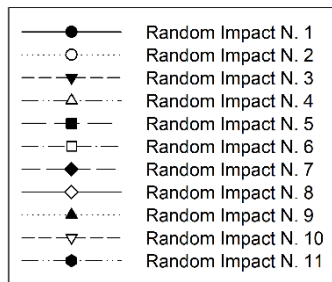
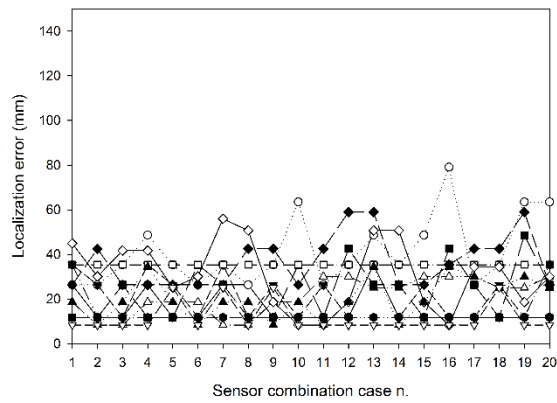
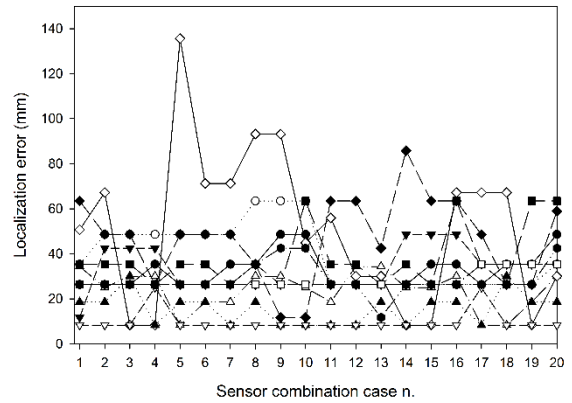


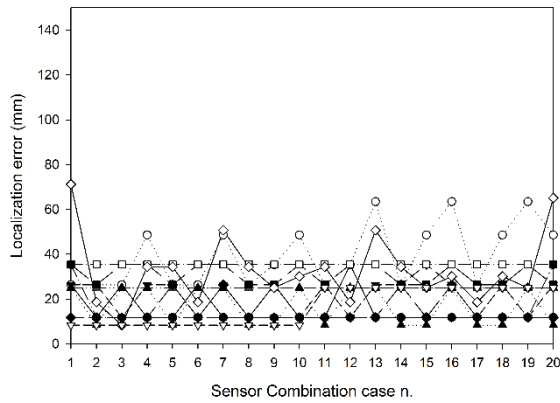
Figure 3.11 Parametric study results of 1D array configuration with two FBG sensors.



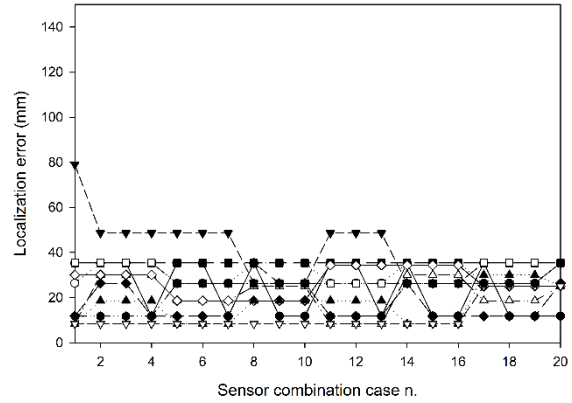
a) Inner wing section parametric study using correlation algorithm



b) Outer wing section parametric study using correlation algorithm



c) Inner wing section parametric study using RMS algorithm



d) Outer wing section parametric study using RMS algorithm

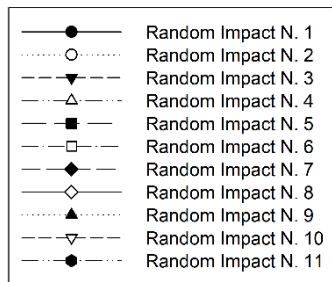


Figure 3.12 Parametric study results of 1D array configuration with three FBG sensors.

Table 3.7 Two FBG sensors parametric study optimal sensor combinations.

RMS Based Two Sensor Optimal Combinations		
Sensor Combination Case N.	Sensor Combination (FBG)	Maximum Error (mm)
3	[1,4]	35.4
4	[1,5]	35.4
7	[2,4]	50.0
8	[2,5]	50.0
10	[3,4]	35.4
11	[3,5]	35.4

From the present results, it can be observed that RMS based impact localization technique performs better than the correlation based method for estimating the impact location when fewer than 6 FBG sensors are used on 1D array FBG configuration. Furthermore, from the present results it has been demonstrated that RMS based reference database impact localization technique along with 1D array configuration SHM system with only two FBG sensor combination cases such as case n., 3, 4, 10 or 11, shown in Table 3.7, can deliver similar impact localization performance as shown by 1D array configuration with six FBG sensors, and 1D array configuration with three sensors combination case n., 8, 9, 14 or 17. Therefore, it can be concluded that using 1D array FBG configuration SHM system with reference database based impact localization algorithm can help to significantly reduce the number of FBG sensors while maintaining the impact localization performance.

The main aim of this parametric study was to demonstrate that impact localization using 1D array FBG sensor configuration and reference database algorithm can be performed using fewer number of sensors to obtain localization error similar to that when all six FBG sensors were used. Additionally, from the present parametric results it was possible to determine the suitable number of sensors and its locations in order to monitor large surface area of a strut based composite wing structure.

It was found that attaching multiple FBG sensors at the same region of the wing did not provide the optimal localization result. Based on the three FBG sensor parametric study, we can conclude that at least one FBG sensor at the outer wing section, one FBG sensor at the strut fixed region and one FBG sensor at the inner wing region results in the impact location predicted with the least localization error. Furthermore, from the two FBG sensor parametric study it was seen that there should be at least one FBG sensor attached to the outer wing region and one FBG sensor attached either in the inner wing region near to the strut fixed region or at the strut fixed region in order to estimate the impact location with the lowest possible overall localization error.

The results not only showed the possibility of using very few number of FBG sensors for monitoring impacts on large area but also showed that the sensor attachment area is dependent on the location of the region

of the wing where the strut was fixed. However, more flexibility in terms of the sensor attachment location is expected for wing structures without the strut. Further research is needed to study the optimal sensor location for varying types of wing structures.

Table 3.8 Three FBG sensors parametric study optimal sensor combinations.

a) Correlation Based Three Optimal Sensor Configurations		
Sensor Combination Case N.	Sensor Combination (FBG)	Maximum Error (mm)
3	[1,2,5]	48.6
4	[1,2,6]	48.6
b) RMS Based Three Optimal Sensor Configurations		
Sensor Combination Case N.	Sensor Combination (FBG)	Maximum Error (mm)
2	[1,2,4]	48.6
3	[1,2,5]	48.6
4	[1,2,6]	48.6
5	[1,3,4]	48.6
6	[1,3,5]	48.6
8	[1,4,5]	35.4
9	[1,4,6]	35.4
10	[1,5,6]	48.6
11	[2,3,4]	48.6
12	[2,3,5]	48.6
14	[2,4,5]	35.4
15	[2,4,6]	48.6
17	[3,4,5]	35.4
18	[3,4,6]	48.6

Chapter 4. Novel Error Outlier Method Based Low Velocity Impact Localization

4.1 Introduction

In this chapter, a novel impact localization technique is developed and its feasibility is demonstrated by detecting and localizing test impact locations on composite plate [99], as well as on aircraft wing structure [100]. The basis of the novel impact localization technique concept is the assessment of error outlier to determine the location of low velocity impact. In the data mining and statistics literature, the term outliers is also used to refer to abnormalities or anomalies [101]. The detection of outliers has a wide range of applications such as medical diagnosis, credit card fraud, etc. Additionally, outlier analysis has also been used for damage detection applications [32], [102].

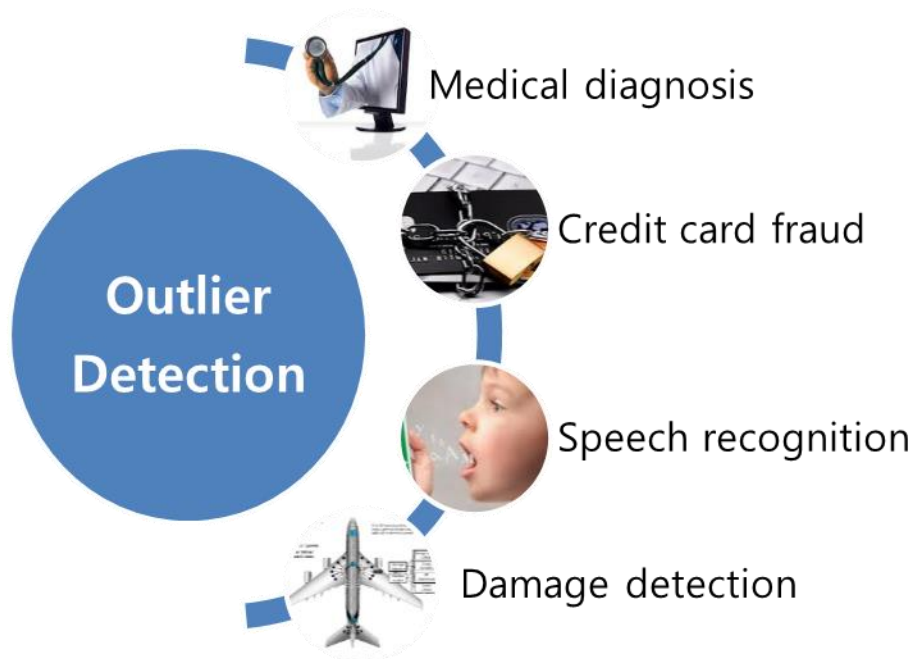
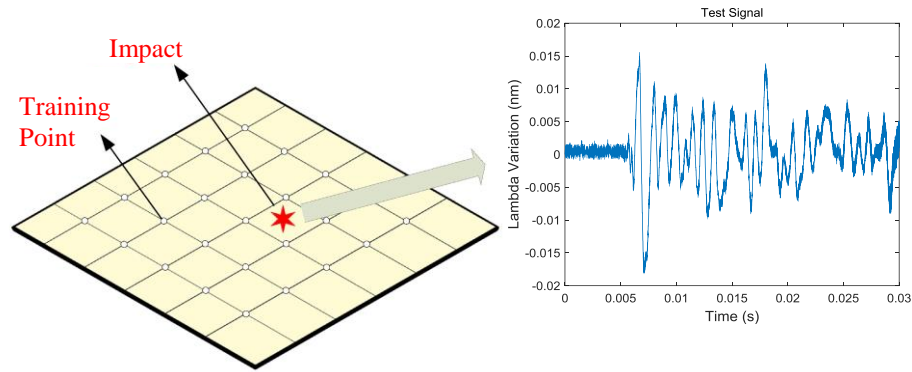


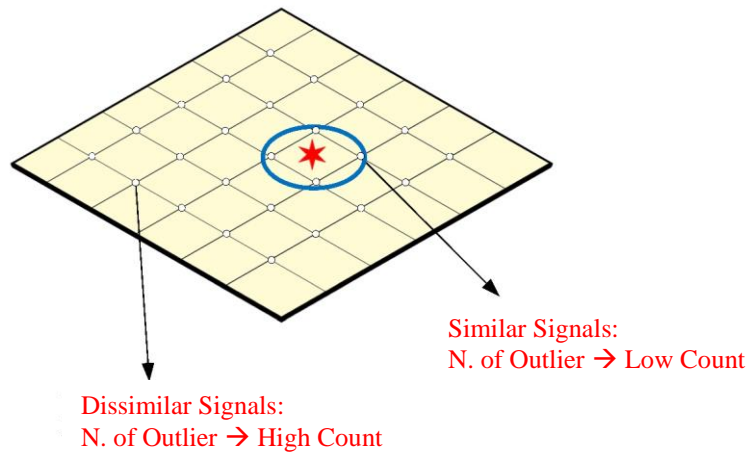
Figure 4.1 Applications of outlier detection.

Error outlier based impact localization concept is illustrated in Figure 4.2. As in the case of the other signal similarity comparing algorithms, when two signals are compared, if the signals are similar then it is highly likely that the computed error values will be low and likewise dissimilar signal will have larger error values. In the RMS and correlation algorithm, the signals comparison between reference points near to the impact location will have lower RMS error values and high correlation coefficients, respectively, and vice versa. Similarly, it can be assumed that the signals comparison between reference points near to the impact location will result in fewer number of error outliers and large number of error outliers when the reference point is farther away from the actual impact location, as illustrated in Figure 4.2 (b). Figure 4.2 (c) shows the

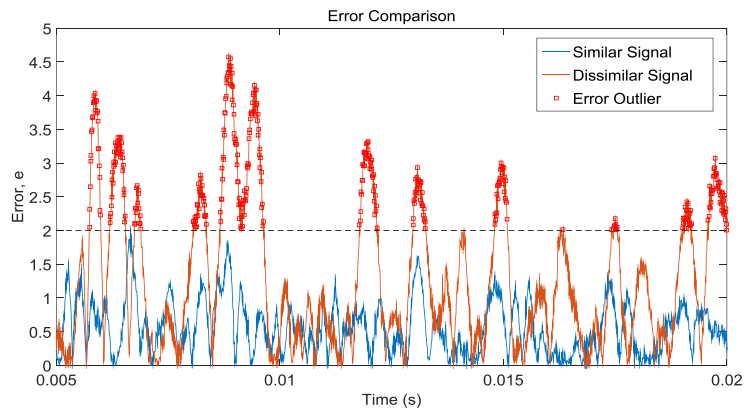
comparison of the error values computed between dissimilar and similar signals. It is clearly evident that dissimilar signals have larger error peak values in comparison to the similar signals error values. Therefore, by setting an error threshold, error value which is larger than the error threshold can be classified as an error outlier as shown in Figure 4.2 (c). It is evident from Figure 4.2 (c) that error values computed between dissimilar signals results in large number of outliers.



a) Impact response signal acquisition



b) Trend in outlier counted near to and farther from the impact location



c) Error signal comparison between similar and dissimilar signal

Figure 4.2 Illustration of error outlier based impact localization concept.

Although the detection of outliers is useful for various different applications, in the present literature review it was found that there is no existing literature available on outlier detection for impact localization application. Therefore, in this chapter, development and demonstration of novel impact localization technique based on error outlier assessment, which operates on the basis that the impact point is most likely to be located near the reference points corresponding to the minimum number of error outliers, is presented. Moreover, the feasibility to localize impact on composite plate and complex composite wing structure was investigated.

4.2 Development of Outlier Method Based Impact Localization Algorithm

The outlier method (OM) developed for localizing the location of the impact is also based on the reference database algorithm. Whereby, set of reference signals required to train the localization algorithm are pre-acquired from the test structure and stored in a database. The reference signal corresponds to the impact signal acquired from the selected reference points on the structure. During impact monitoring, if an impact occurs, then the impact signal is acquired and processed according to the steps shown in Figure 4.3.

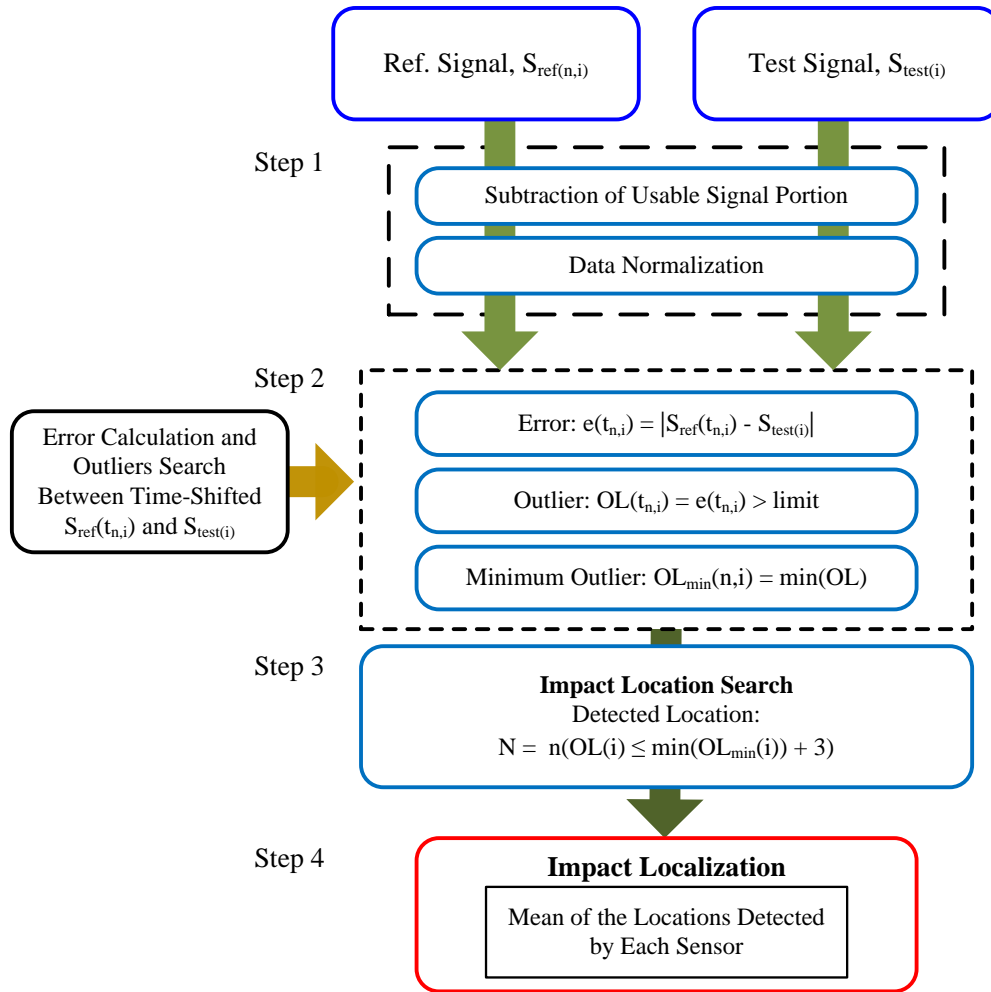


Figure 4.3 Outlier based impact localization algorithm flow chart.

The error outlier based impact localization algorithm flow chart is presented in Figure 4.3. The outlier based impact localization algorithm developed to predict the location of the low velocity impact is based on the reference database algorithm, in which a set of reference signals corresponding to the selected reference points on the structure are pre-acquired. The position of an impact on the test structure is determined by comparing the impact signal with the reference signals. Prior to the signal comparison, the reference signals, $S_{ref(n,i)}$, corresponding to the signal obtained using the FBG sensor 'i' from the reference coordinate point 'n' and the test signal, $S_{test(i)}$, obtained using FBG sensor 'i', are normalized using the standard deviation [103].

$$e(t_{n,i}) = |S_{ref}(t_{n,i}) - S_{test(i)}| \quad (8)$$

After the normalization procedure, the errors between the test signal and the reference signals are calculated using Equation (8). Additionally, the reference signals are time-shifted to improve the localization results. The normalized reference signals are time-shifted, $S_{ref}(t_{n,i})$, by altering the index of the signal starting point from $t=1$ to $t=200$ in increments of $t=1$; then, the errors, $e(t_n)$, between each of the time-shifted reference impact signal and the random impact signal, $S_{ran(i)}$, are computed. In order to determine the error outliers, the absolute error values are compared with the error threshold limit and, subsequently, for each reference grid point, 'n', the minimum outlier, $OL_{min}(n,i)$, among all the time shifted reference signals and the test signals, is determined. This process is repeated for the signals obtained using all the sensors involved in impact monitoring.

In the next step, the impact locations 'N' detected by the FBG sensor 'i' are determined by selecting the reference point 'n' with the least number of error outliers or any reference point 'n' with less than or equal to minimum number of outliers plus three Number of Additional Outliers (NAO). Finally, by calculating the mean of the locations detected by all the FBG sensors, the location of the impact on the test structure is determined.

4.2.1 Impact Localization on Composite Plate using Outlier Method

The error outlier based impact localization experiment was performed on a 690 mm × 690 mm × 4.7 mm quasi-isotropic composite structure with a stacking sequence of [45/90/-45/0₂/-45/0/90/0/-45/0/45/90/-45/0]_s. A high speed FBG interrogator, an SFI-710 (FIBERPRO Inc., Korea) [96], was used to acquire the impact signals from four multiplexed FBG sensors, with center wavelengths of 1532, 1536, 1539, and 1552 nm, respectively, at a 100 kHz sampling frequency. The FBG sensors, with grating lengths of 10 mm, were attached to the bottom surface of the composite plate covering the test area with dimensions of 500 mm × 500 mm. The composite plate was bounded using five point clamps on each of its two edges. The experimental-setup for the impact localization test is shown in Figure 3.3 and the sensor configuration is illustrated in Figure 3.4 (a).

The reference grid was created in the 500 mm × 500 mm test area with 50 mm spacing, resulting in 121 reference points. Impact on the composite structure was simulated using an impact hammer. Validation of the outlier based impact localization algorithm was performed using the 20 different impact test points shown in

Table 3.1 and illustrated in Figure 4.4; subsequently, the obtained results were compared with the RMS results and the correlation based impact localization results [69].

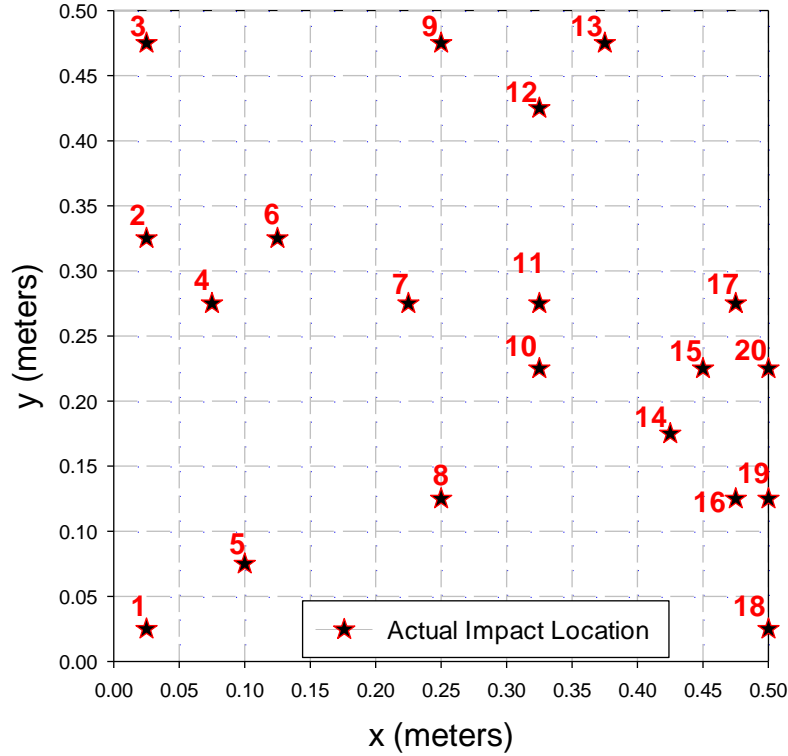


Figure 4.4 Illustration of impact test points on the composite plate.

4.2.2 Error Threshold Set-up

First, in order to determine the error threshold for the outlier based impact localization algorithm, a parametric study of impact localization performance for an error threshold from 0.5 nm to 3.0 nm with interval of 0.5 nm was performed using the impact test points from 1 to 10 shown in Figure 4.4. The results of the error threshold value parametric study are tabulated in Table 4.1. For the purpose of analyzing the error threshold parametric study results presented in Table 4.1, the N. of Outliers obtained using FBG1 for reference points 1 to 121 when an impact is given on Impact Test Point 4 is shown in Figure 4.5.

It can be observed that the N. of Outliers is highly sensitive to the error threshold value. A low threshold value results in a large N. of Outliers counted at each of the reference points. Whereas a high threshold value results in significant decrease in the N. of Outliers counted at each of the reference points. The results show that the outlier based reference database impact localization algorithm is effective at localizing low velocity impacts on the composite plate for thresholds between 0.5 nm and 2.0 nm. From Table 4.1 it is seen that error threshold values larger than 2.0 nm result in average localization error values above 100 mm, whereas small threshold values, i.e., equal to or less than 2.0 nm, give better localization performance.

Table 4.1 Impact localization under varying error threshold parameter.

Impact Test Point	Impact Localization Results (mm)					
	Error Threshold Parameter					
	0.5 nm	1.0 nm	1.5 nm	2.0 nm	2.5 nm	3.0 nm
1	25.5	28.0	16.7	12.5	160.2	272.8
2	35.4	25.0	20.8	2.7	106.2	188.4
3	28.0	28.0	15.8	8.8	178.1	272.5
4	35.4	35.4	25.5	18.8	78.1	143.5
5	37.5	12.5	28.0	37.2	121.2	211.8
6	12.5	12.5	8.8	8.6	84.4	121.1
7	17.7	0.0	15.8	13.2	48.8	29.1
8	25.0	25.0	8.3	0.0	114.6	126.4
9	0.0	0.0	0.0	3.6	133.4	210.4
10	25.0	28.0	15.8	22.5	56.6	63.9
Average Error	24.2	19.4	15.5	12.8	108.2	164.0

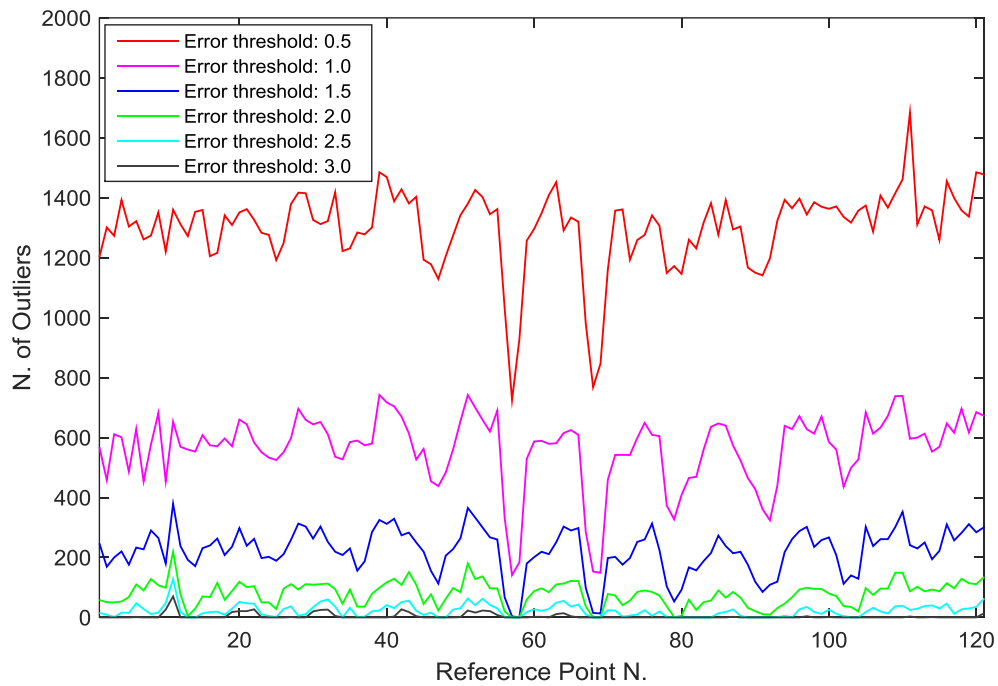


Figure 4.5 N. of Outliers counted at each of the reference point for Impact Test Point 4.

Average localization error improves when the error threshold is increased from 0.5 nm to 2.0 nm, from 24.2 mm to 12.8 mm, respectively. This is due to the fixed value of the NAO used to determine the impact location, i.e., in the current localization algorithm any reference points that have three, or fewer than three additional outliers compared to the reference point with the least N. of Outliers are selected. The criteria for the additional three outliers are found to be suitable because they result in average localization results of about 15.0 mm or less when using the error outlier thresholds of 1.5 nm or 2.0 nm.

A similar trend in the number of outlier results plotted against the reference point n. for error threshold values of 0.5 nm, 1.0 nm, 1.5 nm, and 2.0 nm can be observed in Figure 4.5. However, it can be seen that the difference in the number of outlier between similar reference points becomes larger as the threshold value is decreased. Therefore, NAO parameter, set to 3, plus the minimum N. of Outliers used in the present localization algorithm for determining possible impact locations is not suitable for obtaining further improved localization results for error thresholds below 1.5 nm.

Nonetheless, it is also possible to obtain better results when an error threshold of less than 1.5 nm is used by fine tuning the criteria of the NAO used to determine additional reference points that may be located near the actual point. Moreover, for the present algorithm, satisfactory overall localization error was achieved by setting the error threshold criteria to 2.0 nm; therefore, in the subsequent section, localization using the OM is performed by setting the error threshold criteria to 2.0 nm.

4.2.3 Results and Discussions

The proposed error outlier based impact localization algorithm was used for impact localization of all the 20 impact test points shown in Figure 4.4 and the results were compared with the RMS and correlation based localization results [69], shown in Table 4.2. In comparison to the RMS and correlation based algorithm, the outlier based algorithm also predicted the location of all the impact test points with localization errors less than 50.0 mm, the grid size used for training the reference database algorithm.

The average impact localization error obtained using the OM is found to be improved in comparison to the results obtained using the RMS and correlation methods. However, at impact test points n. 5, 15, 16, and 19, localization errors were larger than the maximum localization error of 28.0 mm obtained using the RMS and correlation methods. In order to determine the reason for the increase in the localization error that occurred at these impact test points, color-mapped figures corresponding to the N. of Outliers for Impact Test Point 19, with the maximum localization error of 39.9 mm, were studied.

Table 4.2 RMS, correlation, and OM localization results comparison.

Impact Test Point	Impact Localization Results (mm)		
	RMS [69]	Correlation [69]	OM
1	25.0	28.0	12.5
2	28.0	25.0	2.7
3	25.0	25.0	8.8
4	28.0	12.5	18.8
5	17.7	0.0	37.2
6	12.5	17.7	8.6
7	0.0	25.0	13.2
8	25.0	12.5	0.0
9	25.0	12.5	3.6
10	17.7	17.7	22.5
11	17.7	25.0	3.6
12	25.0	28.0	7.2
13	12.5	17.7	14.0
14	28.0	25.0	6.7
15	17.7	25.0	33.5
16	17.7	12.5	37.6
17	12.5	17.7	2.7
18	25.0	25.0	14.0
19	12.5	25.0	39.9
20	12.5	25.0	25.0
Maximum Error	28.0	28.0	39.9
Average Error	19.2	20.1	15.6
SD	7.2	7.1	12.9

In Figure 4.6, the error outliers for FBGs 1~4 are color-mapped with respect to the N. of Outliers at each of the reference points in the composite plate. The color map ranges from dark blue to dark red, with those respective colors corresponding to a lower N. of Outliers and a larger N. of Outliers. The reference points closer to the actual impact point colored dark blue. Furthermore, comparing all four FBG color-mapped figures, it can be seen that FBG1, located closest to the actual impact point, detected the impact location most accurately, whereas the FBGs that were located farther from the impact location showed large areas of the composite plate

with fewer numbers of outliers. The location selected by the OM for the final impact location estimation is visualized in Figure 4.7. At Impact Test Point 19, a large localization error occurred due to the selected reference location spreading out by about 100 mm from the actual impact location.

Moreover, the present results show the feasibility of using the error OM to localize the impact test points on a composite plate. All 20 impact test points were localized with average error of 15.6 mm using the OM, 3.6 mm, and 4.5 mm less than the RMS and correlation average localization errors, respectively. Although a better overall localization error was achieved, it was found that the localization errors at some of the impact test points were larger than, 28.0 mm, the maximum location error obtained using RMS and the correlation method. Therefore, in the subsequent section, further improvement in the localization performance is sought by including the Euclidean distance threshold criteria in the present outlier based impact localization algorithm.

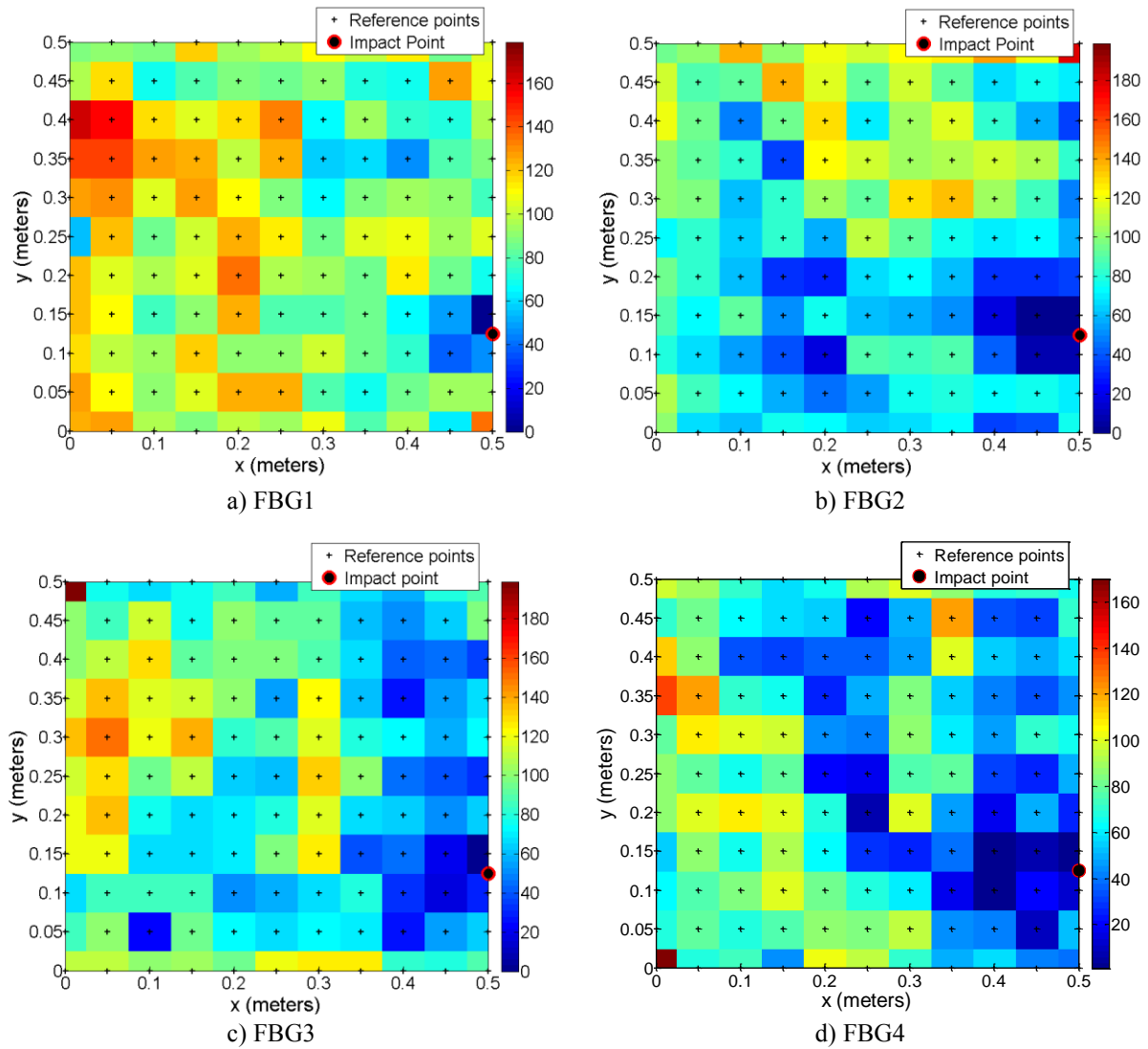


Figure 4.6 Impact Test Point 19: N. of Outliers corresponding to color-mapped figures.

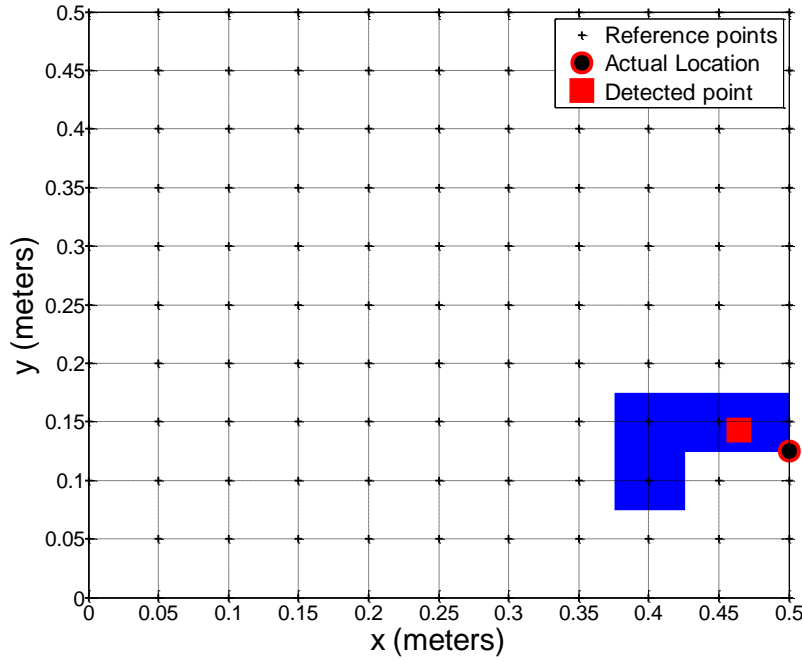


Figure 4.7 Visualization of detected range and location.

4.3 Enhanced Outlier Method using Euclidean Distance Threshold

4.3.1 Overview

In order to narrow down the range of locations detected by the outlier algorithm, the Euclidean distance threshold criteria was integrated into the outlier based impact localization algorithm. Figure 4.8 illustrates the flowchart for the improved outlier based impact localization algorithm. The OM presented in Section 4.2 will be referred to as OM1; the outlier based impact localization algorithm with the Euclidean threshold will be referred to as OM2.

The response signals obtained from the sensors, used for monitoring the structure, are processed by OM2 algorithm in a procedure similar to those used in the OM1 algorithm. The improved outlier localization algorithm follows Step 1, Step 2, and Step 3, as shown in Figure 4.3, for normalization, error outlier assessment and impact location determination. The impact localization algorithm in OM2 differs from that in OM1 after Step 3 is completed. Once all the possible location points ‘N’ are identified in Step 3, in the next step the OM2 algorithm evaluates whether to include any possible detected location that can be used to determine the final impact location. Selection of the most likely impact locations are done by following two additional steps.

Firstly, comparison of the Euclidean distances between the x-coordinate and the y-coordinate of each of the detected locations with the mean of the x-coordinate and the y-coordinate, ‘Dx’ and ‘Dy’, respectively, for all the detected locations, is performed. To estimate the impact location, the x-coordinate or the y-coordinate

that is farther than Threshold1, 100 mm, from the mean is rejected from the possible location points 'N'. In the second step, the mean of the locations selected after the first step is calculated; then, the distances 'Dx' and 'Dy' between the x-coordinate and the y-coordinate are compared. If the distance is more than Threshold2, 60 mm from the mean, then the location is excluded from the final location calculation procedure. Finally, the location of the impact is estimated by calculating the mean of the reference points; this mean value is selected through the Euclidean distance threshold comparison.

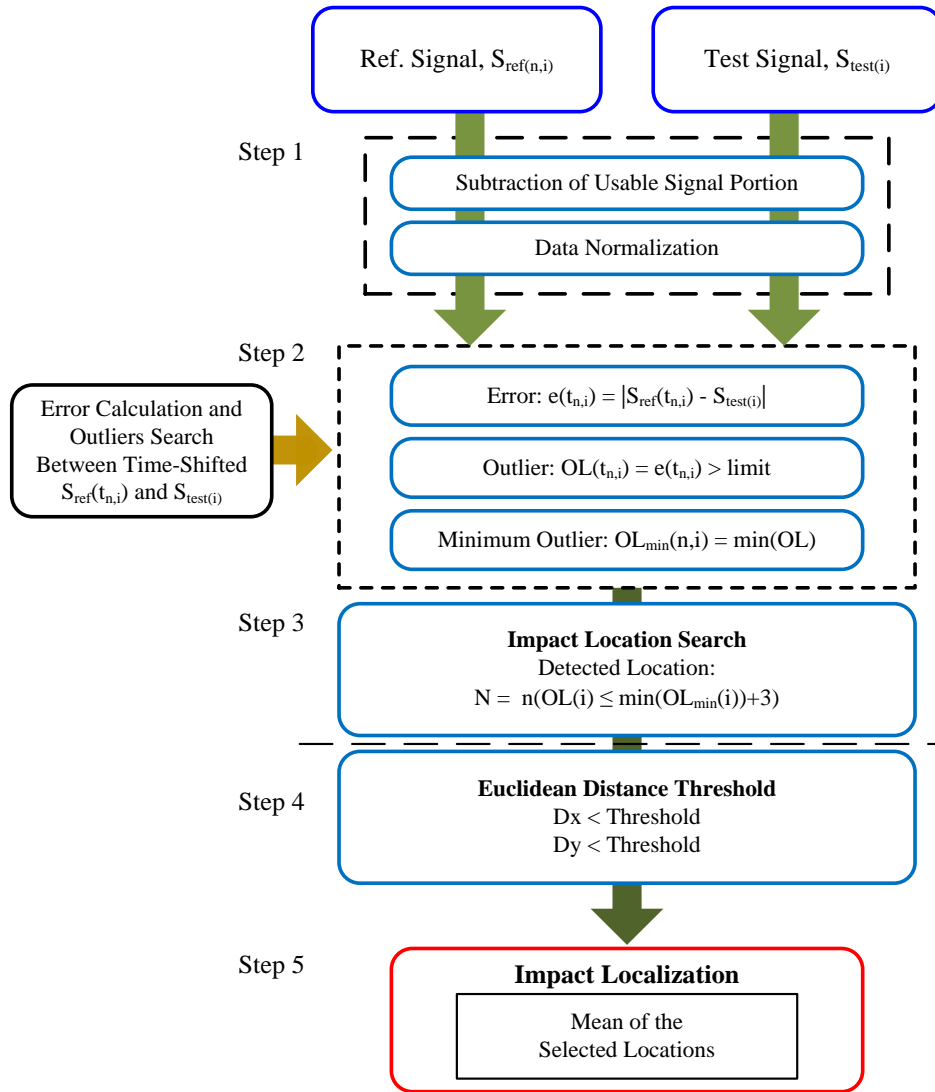


Figure 4.8 OM2 impact localization algorithm flowchart.

4.3.2 Impact Localization on Composite Plate

The impact test points illustrated in Figure 4.4 were used to evaluate the OM2 impact localization algorithm. The 20 impact test points were localized using OM2; the results are compared with the results for OM1, shown in Figure 4.9, and with the RMS and the correlation based impact localization results, shown in Table 4.3.

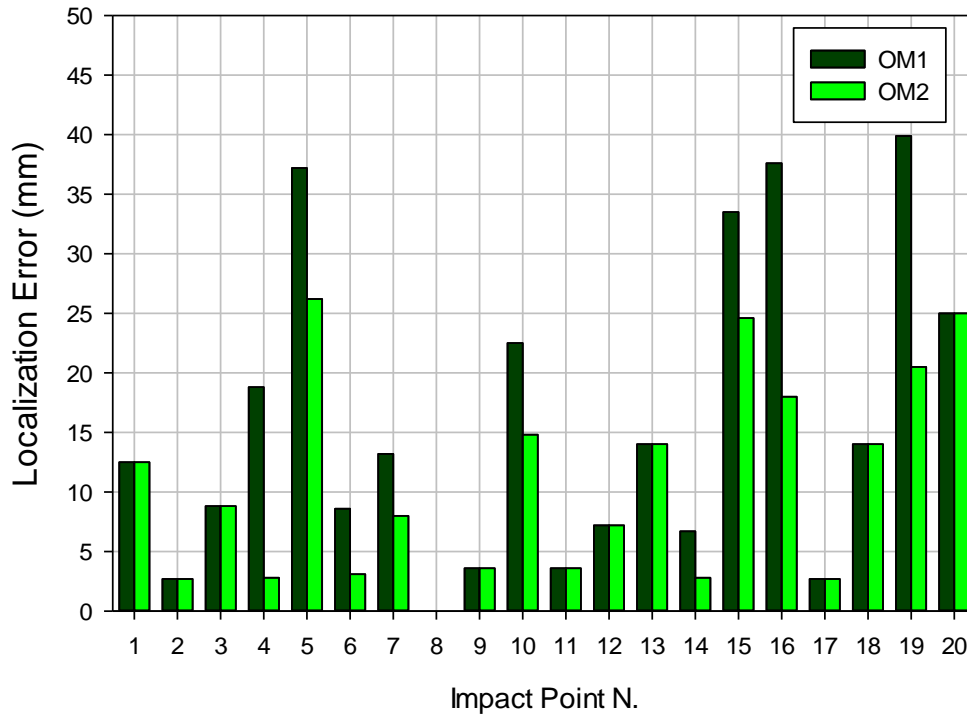


Figure 4.9 Comparison results of OM1 and OM2.

Using the improved OM, a significant improvement in the localization results for the composite plate is obtained. The maximum localization error of 39.9 mm using OM1 at Impact Test Point 19 is reduced to 20.5 mm. Figure 4.10 shows the range of locations, selected for final impact location prediction, obtained using the OM2 impact localization algorithm. The use of the Euclidean threshold resulted in the detection of possible impact locations closer to the actual impact location. Moreover, the maximum error using the OM2 is reduced to 26.2 mm, 1.6 mm less than that of the RMS and Correlation based impact localization methods.

Furthermore, the localization results show that the impact on the composite structure is better localized using OM2 than it is using the RMS, correlation, or OM1 localization algorithms. In comparison to the RMS and correlation results, an approximately 45% reduction was achieved for the average localization error when using the OM2 method. Most of the impact test points were localized within about 10.7 mm of the actual impact point, whereas the average impact localization errors when using the RMS, correlation, and OM1 methods are 19.2 mm, 20.1 mm, and 15.6 mm, respectively.

Table 4.3 Localization results comparison.

Impact Test Point	Localization Results (mm)			
	RMS [69]	Correlation [69]	OM1	OM2
1	25.0	28.0	12.5	12.5
2	28.0	25.0	2.7	2.7
3	25.0	25.0	8.8	8.8
4	28.0	12.5	18.8	2.8
5	17.7	0.0	37.2	26.2
6	12.5	17.7	8.6	3.1
7	0.0	25.0	13.2	8.0
8	25.0	12.5	0.0	0.0
9	25.0	12.5	3.6	3.6
10	17.7	17.7	22.5	14.8
11	17.7	25.0	3.6	3.6
12	25.0	28.0	7.2	7.2
13	12.5	17.7	14.0	14.0
14	28.0	25.0	6.7	2.8
15	17.7	25.0	33.5	24.6
16	17.7	12.5	37.6	18.0
17	12.5	17.7	2.7	2.7
18	25.0	25.0	14.0	14.0
19	12.5	25.0	39.9	20.5
20	12.5	25.0	25.0	25.0
Maximum Error	28.0	28.0	39.9	26.2
Average Error	19.2	20.1	15.6	10.7
SD	7.2	7.1	12.9	8.5

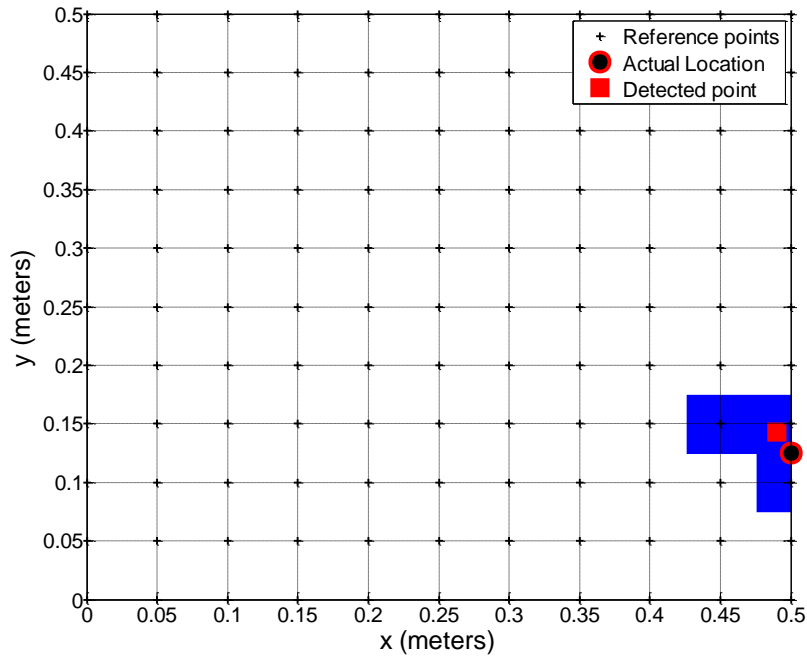


Figure 4.10 OM2 detected location visualization.

Table 4.4 Impact localization on composite panel results comparison.

Ref. N.	Dimension (mm) × (mm) × (mm)	Impact Test Region (mm) × (mm)	Sensor Type	N. of Sensors	Avg. Error (mm)	Max. Error (mm)
Present	690 × 690 × 4.7	500 × 500	FBG	4	10.7	26.2
[79]	305 × 305 × 1.5	--	FBG	5	14.5	--
[79]	305 × 305 × 1.5	--	FBG	4	36.1	--
[76]	300 × 300 × 4.2	150 × 180	FBG	4	10.0	16.0
[76]	300 × 300 × 4.2	180 × 260	Accelerometer	4	6.0	32.0
[71]	340 × 340 × 2.5	--	PZT	4	17.0	--
[68]	690 × 690	250 × 250	FBG	4	8.2	24.6
[75]	700 × 700 × 5.0	250 × 250	FBG	4	4.5	16.1

In Table 4.4, localization results of several impact localization experimental studies done on composite panel are presented. Overall, it can be observed that the localization result is highly dependent on the impact test region, types of sensor, number of sensors used for the localization and the localization technique. Nonetheless, despite of the varying experimental parameters, it is seen that the average errors and the maximum errors ranges from 4.5 mm to 36.1 mm and from 16.0 mm to 32.0 mm, respectively. In this study, the average localization error and the maximum localization error of 10.7 mm and 26.2 mm, respectively, obtained using the novel

localization method based on error outliers assessment are found to be satisfactory and reasonable in comparison to various other experimental results presented in Table 4.4.

Furthermore, using the OM algorithm with similar setting used in this study, it is possible to estimate the location of the impact test points on the composite plate with less computation time. Running the algorithm on a computer system with an Intel(R) Core(TM) i7-4770 CPU @ 3.40GHz with 16GB RAM memory, it took on average about 7.4 s to estimate each of the impact test point, whereas the average time taken to estimate an impact point using the correlation and RMS methods were 20.0 s and 17.3 s [69], respectively.

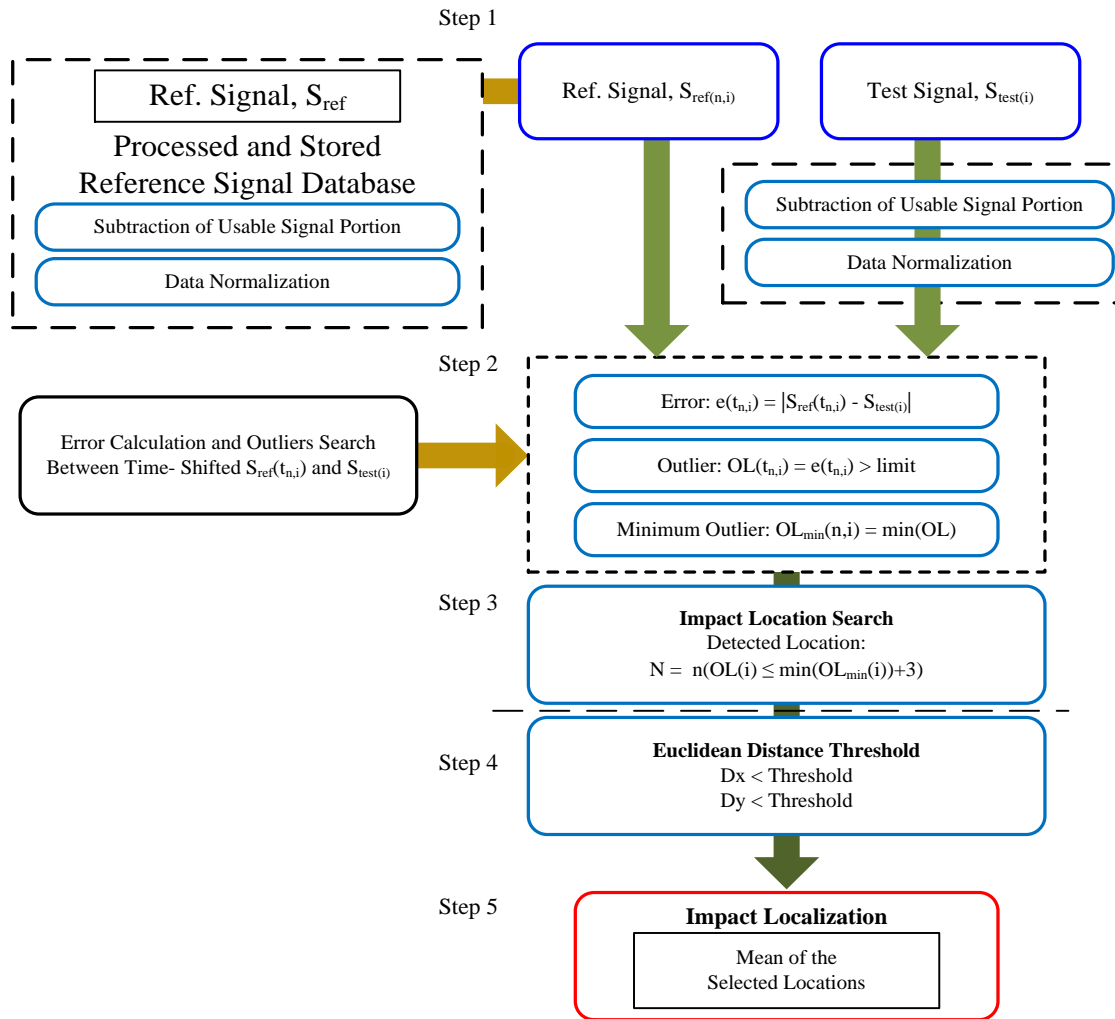


Figure 4.11 Improved processing time by pre-processing the reference signals.

The algorithm processing time can be further improved by pre-processing and storing the reference signals in the database. As a result, when the algorithm performs the localization, it will only be required to process the test signal and then compare the pre-processed reference signals with the normalized test signal, as illustrated in Figure 4.11. Using the updated algorithm presented in Figure 4.11, the average time taken to calculate the impact point was significantly reduced to 3.2 s.

In conclusion, the present OM2 localization algorithm shows significant improvement in the localization performance compared to the OM1 localization algorithm for the detection of impact location on composite plate structures; similar or improved results were obtained in comparison to the RMS and the correlation based localization methods. In the subsequent sections, further validation of the proposed OM based impact localization algorithms are demonstrated on composite wing structure.

4.3.3 Impact Localization on Composite Wing

Impact localization of impacts on complex composite structures such as the aircraft's wing is highly desirable for real-time SHM applications. In this section, the OM1 and OM2 impact localization algorithms are further examined by localizing impact test points on the composite wing of Jabiru UL-D, presented in section 3.4, to determine whether such localization techniques can be effective in detecting impact test points on complex composite structure. The experimental set-up used for the verification of OM1 and OM2 to localize impact test points on the composite wing is the same as the figure shown in Figure 3.8. The inner section of the wing is used for impact localization test.

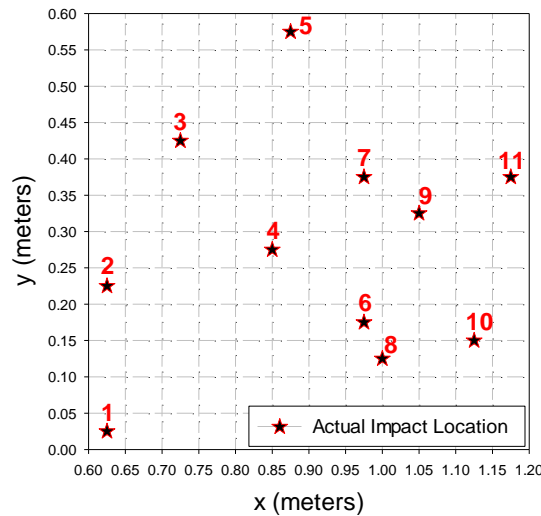


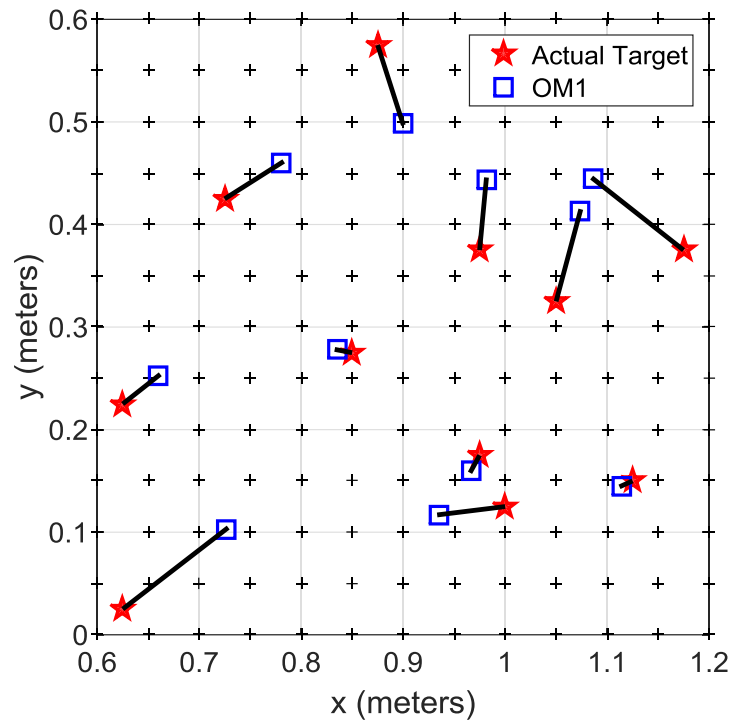
Figure 4.12 Visualization of impact test points on the inner wing section.

Signals acquired from the six FBG sensors, with center wavelength ranging from 1532 nm to 1547 nm, attached on the upper surface of the composite wing are processed using the OM1 and OM2 impact localization algorithms to monitor impacts on the wing surface. The 11 impact test points on the wing's upper surface, visualized in Figure 4.12, are localized and compared with baseline RMS and correlation results [69] presented in section 3.4. The impact test points on the composite wing were localized using the OM1 and OM2 impact localization algorithms with same parameters used for localizing impacts on the composite plate, i.e., error threshold value of 2.0 nm and $NAO = 3$ were used, and the results are tabulated in Table 4.5 and visualized in Figure 4.13.

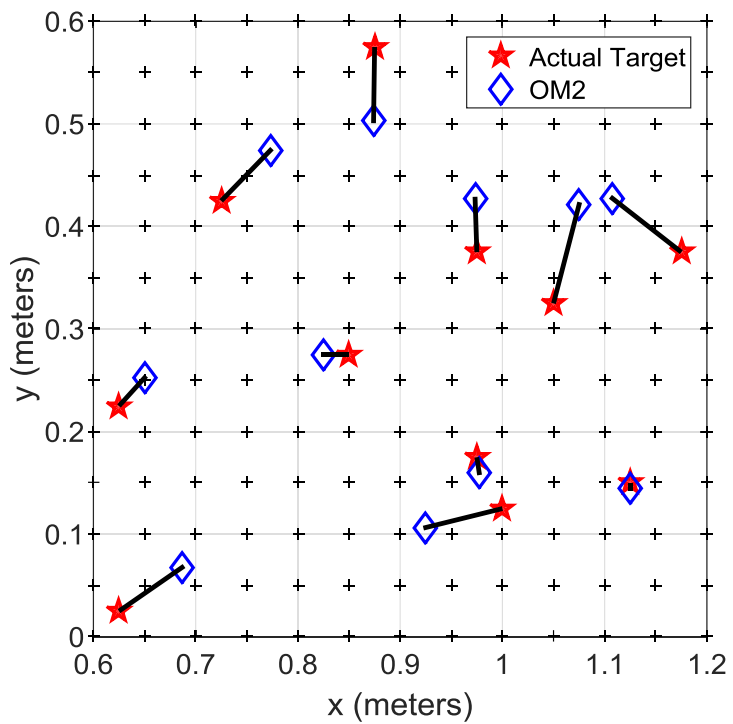
Table 4.5 OM1 and OM2 inner wing localization.

a) OM1 Inner Wing Localization Results			
Impact Test Point	Detected Location		Localization Error (mm)
	x (mm)	y (mm)	
1	726.6	103.1	128.1
2	660.0	252.5	44.5
3	780.9	460.3	66.1
4	835.2	277.8	15.1
5	899.5	499.1	79.8
6	966.7	160.0	17.2
7	981.5	443.5	68.8
8	935.7	117.1	64.8
9	1073.6	412.6	90.8
10	1114.3	145.2	11.7
11	1086.7	444.3	112.3
Maximum Error			128.1
Average Error			63.6
SD			37.1

b) OM2 Inner Wing Localization Results			
Impact Test Point	Detected Location		Localization Error (mm)
	x (mm)	y (mm)	
1	686.7	67.6	75.0
2	650.0	252.5	37.2
3	773.0	474.2	68.8
4	825.0	275.0	25.0
5	874.0	503.1	71.9
6	977.3	160.0	15.2
7	973.3	426.6	51.6
8	925.0	106.5	77.3
9	1075.0	421.4	99.6
10	1125.0	145.2	4.8
11	1107.5	427.5	85.5
Maximum Error			99.6
Average Error			55.6
SD			29.6



a) OM1 predicted impact location visualization



b) OM2 predicted impact location visualization

Figure 4.13 OM1 and OM2 inner wing predicted impact location visualization.

The impact localization performed using OM1 resulted in average localization error of 63.6 mm and maximum localization error of 128.1 mm, as shown in Table 4.5. Whereas, using the OM2 the average localization error of 55.6 mm and maximum localization error of 99.6 mm were obtained. As in the case of the composite plate impact localization results, better results using OM2 than OM1 were obtained. However, the results presented in Table 4.5 are not as accurate as the impact localization results obtained when impact tests were performed on the composite plate. The composite plate localization results and the composite wing localization results are compared in Table 4.6.

Table 4.6 Comparison of composite plate and composite wing OM impact localization results.

Localization Results Comparison				
	Composite Plate		Composite Wing	
	OM1	OM2	OM1	OM2
Average Error (mm)	15.6	10.7	63.6	55.6
Maximum Error (mm)	39.9	26.2	128.1	99.6

Error threshold parametric study was done to investigate the cause of the significant increase in localization error using the OM1 and OM2 algorithms for the composite wing impact test signals. Figure 4.14 shows the N. of Outliers calculated between the test signal, obtained by delivering impact at Impact Test Point 1, and the reference signals, reference points 1 to 169, for error threshold parameters from 0.5 nm ~ 3.0 nm. It can be seen that the total N. of Outliers is significantly reduced for error threshold limit from 2.0 nm ~ 3.0 nm. Figure 4.15 shows the N. of Outliers obtained at each of the reference points using error threshold values of 1.5 nm, 2.0 nm, 2.5 nm, and 3.0 nm. High error threshold value of 2.0 nm used in OM1 and OM2 results in several reference points, which are farther from the actual impact location, having zero N. of Outliers.

Similarly, the N. of Outliers decreases drastically when the error threshold limit is set to 2.5 nm and 3.0 nm. High error threshold limit causes the OM impact localization algorithm to falsely identify several reference points as the impact location as these reference points are found to have low N. of Outliers or no outlier at all. As a result, this led to increase in the localization error for the composite wing impact localization test cases. Although the error threshold value of 2.0 nm enables the OM1 and OM2 algorithms to obtain satisfactory results for composite plate case, it is found to result in larger localization error for complex composite structure. It can be concluded that the parameters that results in good localization performance in one structure may not necessarily result in similar result when implemented directly on a different structure. Therefore, it is required to determine suitable error threshold value to improve the localization performance of OM1 and OM2 when the structure is changed. Firstly, the localization tests for Impact Test Point 1 case were conducted by varying error threshold limit, from 0.5 nm ~ 3.0 nm, and the localization results are tabulated in Table 4.7.

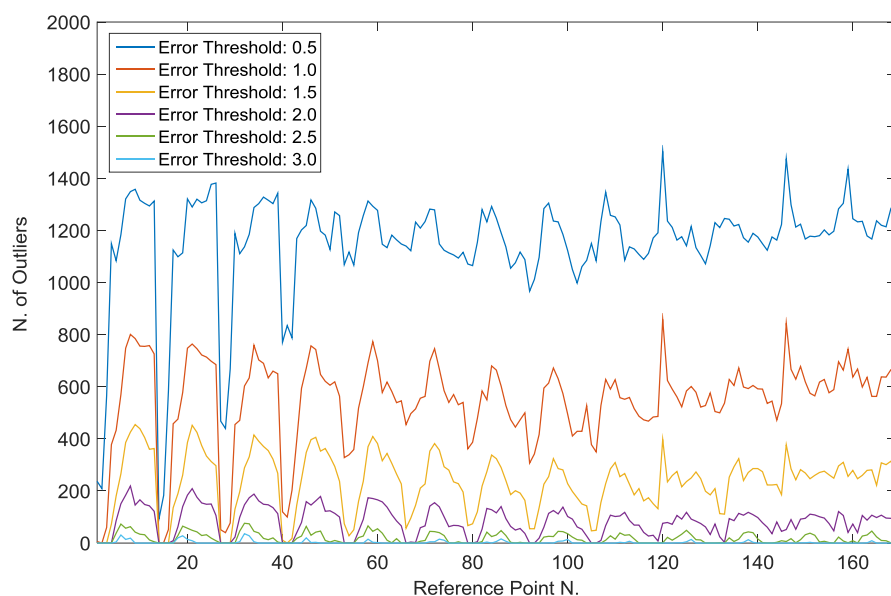
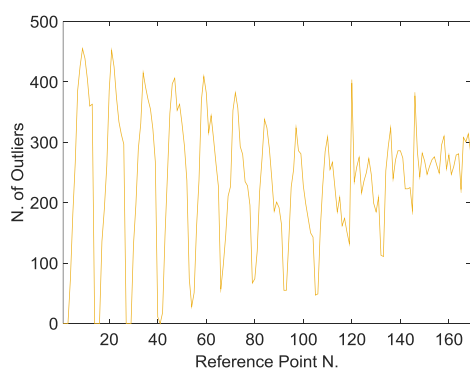
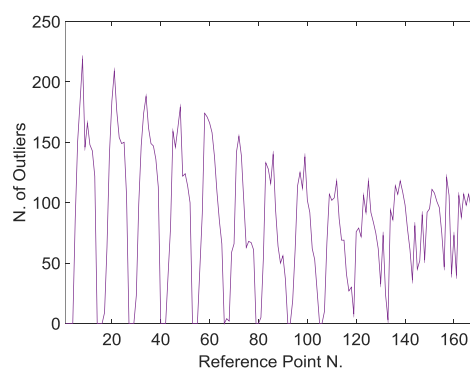


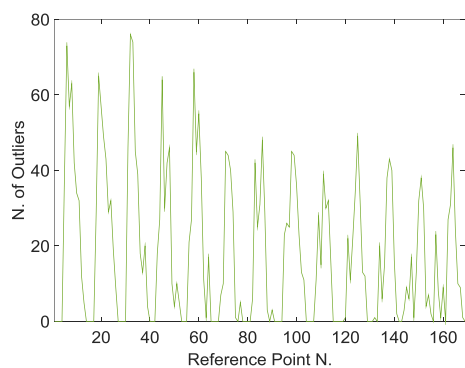
Figure 4.14 Error threshold parametric study at Impact Test Point 1 using FBG1 sensor.



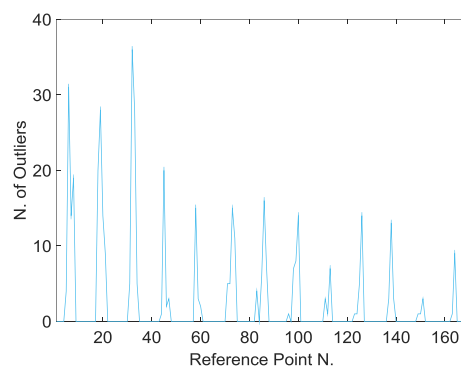
a) Error threshold: 1.5



b) Error threshold: 2.0



c) Error threshold: 2.5



d) Error threshold: 3.0

Figure 4.15 N. of Outliers at each reference point for varying error threshold values using FBG1.

Table 4.7 OM1 and OM2 localization performance comparison.

	Impact Test Point 1 Localization Error (mm)					
	Error Threshold Value					
	0.5 nm	1.0 nm	1.5 nm	2.0 nm	2.5 nm	3.0 nm
OM1	30.7	13.3	22.4	128.1	349.7	372.2
OM2	30.7	13.3	16.3	75.0	353.9	353.8
Computation time (s)	15.1	10.2	7.9	6.6	6.0	5.8

Table 4.7 shows the localization results for error threshold parametric study conducted when impact was given at Impact Test Point 1. Decreasing the error threshold limit significantly improved the localization result of Impact Test Point 1 on the composite wing. When the error threshold value was set to 1.5 nm, the impact location was detected within the range of 22.4 mm and 16.3 mm using the OM1 and OM2 impact localization algorithms. Similarly, the impact location is more accurately predicted when the error threshold value was set to 1.0 nm. Both the algorithms, OM1 and OM2, detected the location with localization error of 13.3 mm. Finally, when the impact was localized with error threshold value of 0.5 nm, the impact location was detected to be 30.7 mm from the actual impact location by both of the OM1 and OM2 algorithms.

Therefore, the present results show that for complex composite structure the impact location can be detected accurately by decreasing the error threshold limit below 2.0 nm. The improved localization results were possible due to the increased N. of Outliers that are obtained when the error threshold limit is lowered, as shown in Figure 4.14. In Figure 4.14, the N. of Outliers are significantly low at only some of the reference points when the error threshold value of less than 2.0 nm was used, in comparison to the results obtained when error threshold value of 2.0 nm or higher was used.

Additionally, the time taken to predict the impact location of impact delivered at Impact Test Point 1 for varying error threshold parameters are presented in Table 4.7. The results show that the computation time is highly sensitive to the selected error threshold limit. It took 15.1 s, 10.2 s, 7.9 s, 6.6 s, 6.0 s and 5.8 s to compute the impact location using error threshold value of 0.5 nm, 1.0 nm, 1.5 nm, 2.0 nm, 2.5 nm and 3.0 nm, respectively. A high error threshold value results in quicker computation time and a low error threshold value increases the time it takes to compute the impact location. The computation time sensitivity to the error threshold value is a result of the N. of Outliers that is obtained when the test signals and reference signals are compared. High error threshold value corresponds to lower number of N. of Outliers resulting in low computation time to assess these outliers for impact localization and low threshold corresponds to more N. of Outliers which require more time to be assessed by the computer system.

From the parametric results it was found that the best impact localization results were obtained using the OM1 and OM2 when the error threshold value was set to 1.0 nm. Therefore, the remaining 10 impact test points were localized using error threshold value of 1.0 nm. The impact localization results for the 11 impact test points on the composite wing were localized and the results are visualized in Figure 4.16. Furthermore, the localization results are compared with the RMS and correlation based impact localization results in Table 4.8.

In Figure 4.16, all the impact test points are shown to be detected close to the actual impact location using the two different outlier based impact localization algorithms. Changing the error threshold parameter from 2.0 nm to 1.0 nm has resulted in significant improvement in the localization results. Results presented in Table 4.8, shows that all of the 11 impact test points were localized with maximum localization error of 35.4 mm using the OM1 and OM2 algorithms. Similarly, the average localization error was also drastically decreased to 20.8 mm and 21.1 mm using the OM1 and OM2 algorithms. These results demonstrate that the feasibility of using outlier based impact localization algorithm to detect impact test points on complex composite structures such as wing structure as well.

The localization results of OM1 and OM2 compared with RMS and correlation method shows that the outlier based impact localization performs similar to the RMS and correlation impact localization algorithms. Although OM1 and OM2 determined all the impact locations within 35.4 mm localization error, same as the RMS and correlation results, the average localization performance can be seen to be slightly less accurate than the RMS and correlation methods. Even though the outlier based algorithm performed satisfactorily further investigation to improve the present outlier algorithms in order to achieve similar or better performance compared to RMS and correlation based impact localization algorithm was done.

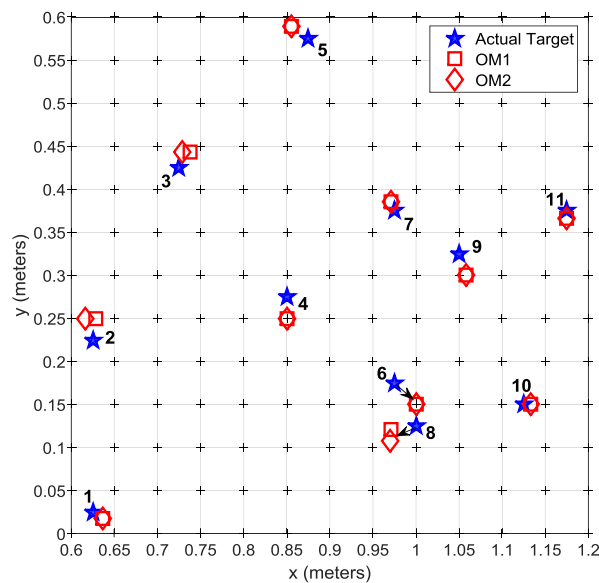


Figure 4.16 Predicted impact location using OM1 and OM2 using error threshold value of 1.0 nm.

Table 4.8 Comparison of impact localization results obtained using various localization methods.

Impact Test Point	Localization Results Comparison (mm)			
	RMS [69]	Correlation [69]	OM1	OM2
1	8.3	8.3	13.3	13.3
2	35.4	35.4	25.3	26.4
3	11.8	18.6	22.5	19.1
4	16.7	25.0	25.0	25.0
5	18.6	30.1	23.9	23.9
6	35.4	35.4	35.4	35.4
7	8.3	0.0	11.3	11.3
8	8.3	11.8	28.8	34.3
9	11.8	16.7	26.4	26.4
10	8.3	16.7	8.3	8.3
11	0.0	0.0	8.3	8.3
Maximum Error	35.4	35.4	35.4	35.4
Average Error	14.8	18.0	20.8	21.1
SD	10.7	12.0	8.6	9.3

4.3.4 NAO Parametric Study

In this section, the effect of varying additional number of outlier for impact location selection is examined using the impact test signals from the composite wing. In the previous sections, three NAO were used in the OM1 and OM2 algorithms. The NAO parametric study was conducted by varying the NAO parameter from 10 to 180 with an interval of 10. The changes in the localization error were studied for both of the OM1 and OM2 impact localization algorithms by performing the localization tests using the same 11 impact test points on the upper surface of the composite wing as visualized in Figure 4.12.

Figure 4.17 shows the OM1 maximum and average localization error for the NAO parametric study results when the NAO were varied from 10 to 180. Additionally, for comparison, it also includes the localization results when three NAO parameter (baseline) were used to localize impacts, as presented in the previous sections. When the NAO parameter is increased from 10 to 30, both the maximum and average localization errors are found to be similar to the baseline results, i.e., the maximum localization error falls within the range of about 40 mm and the average error too falls within the range of about 20 mm. However, further increase in the NAO from 40 to 180 results in drastic increase in the maximum localization error result. Though there is a significant increase in the maximum localization error, the average error value increases gradually from about

20.0 mm to 50.0 mm as the NAO is increased from 40 to 180. This shows that the large localization error occurs at only few of the impact test points.

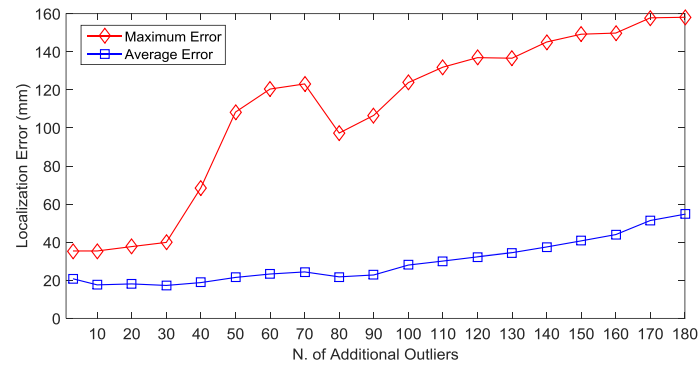
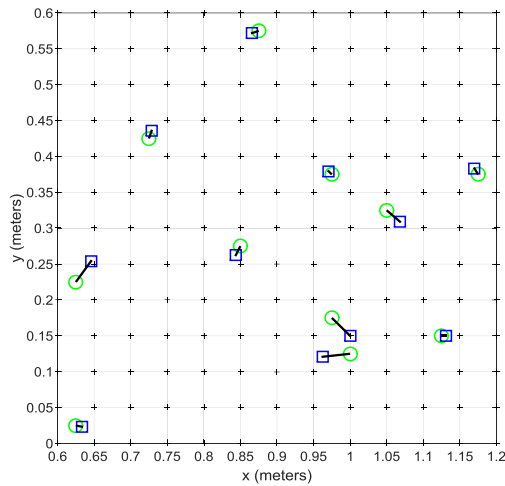
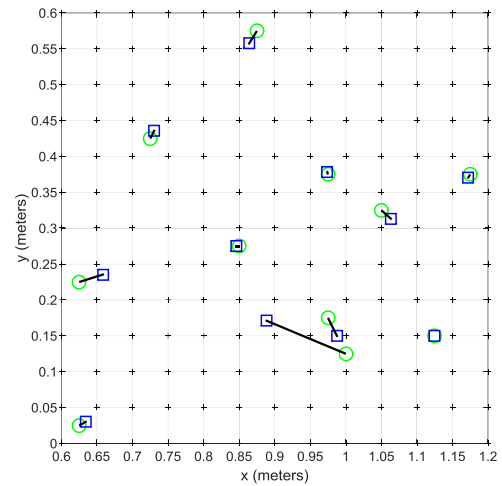


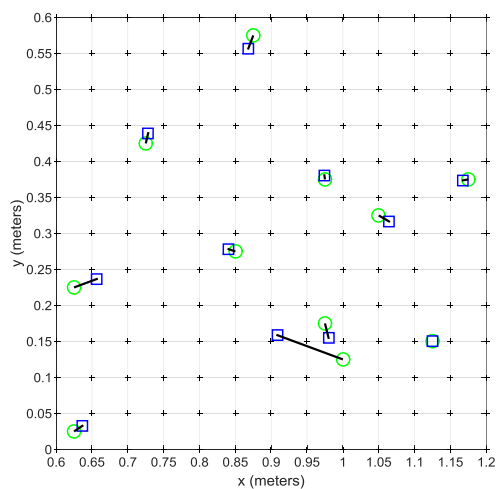
Figure 4.17 OM1 impact localization results for varying NAO.



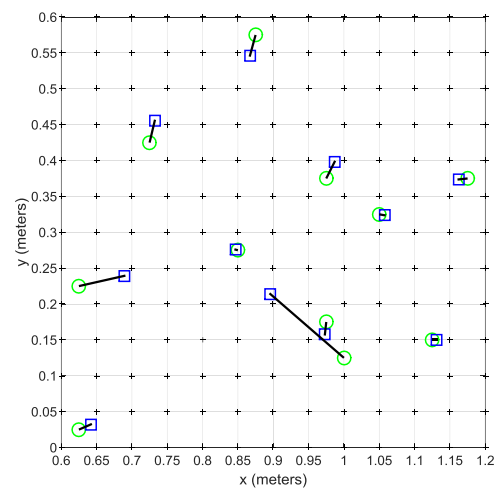
a) NAO: 20



b) NAO: 60



c) NAO: 80



d) NAO: 120

Figure 4.18 OM1 impact localization visualization for varying NAO cases.

The impact localization results for the 11 impact test points for OM1 with 20, 60, 80 and 120 NAO are visualized in Figure 4.18 (a-d). Overall, Figure 4.18 shows that most of the impact test points are well localized. The maximum error localization error occurs at Impact Test Point 8 when the NAO parameter is higher than 20. Whereas, the only other point with localization error larger than 50.0 mm occurrence can be seen in Figure 4.18 (d) at Impact Test Point 2. Thus, it can be concluded that increasing the NAO parameter is suitable for impact localization, however there are some exceptions when the OM1 may not accurately predict the impact location as presented in Figure 4.17 and Figure 4.18.

Similar parametric study to determine the localization performance of OM2 algorithm was done by varying the NAO from 10 to 180. The maximum and average localization errors of the 11 impact test points are presented in Figure 4.19. In comparison to the OM1 results shown in Figure 4.17, OM2 results are found to be relatively better. The maximum localization error is estimated to approximately 40.0 mm from the actual impact location for the 10, 20, and 40 NAO. Whereas for 30 NAO, the maximum localization error increase to 54.2 mm. The Euclidean distance threshold minimizes the maximum localization error below 100.0 mm for NAO values between 50 to 100. Similarly, the algorithm also helps to reduce the localization error when more than 130 NAO are used to determine the impact location.

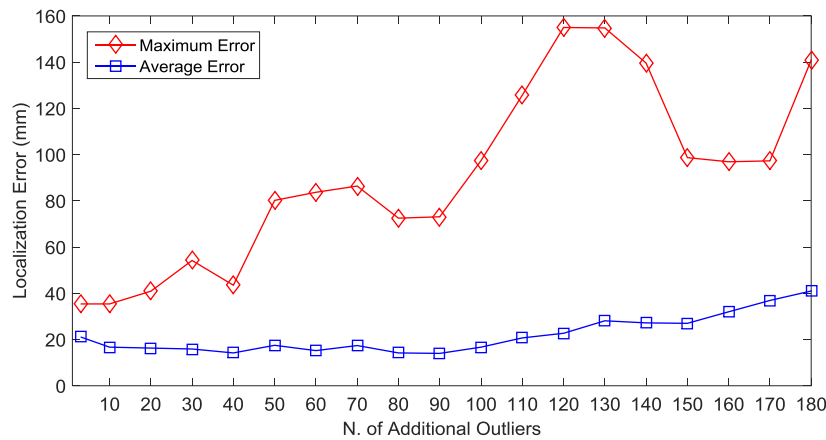
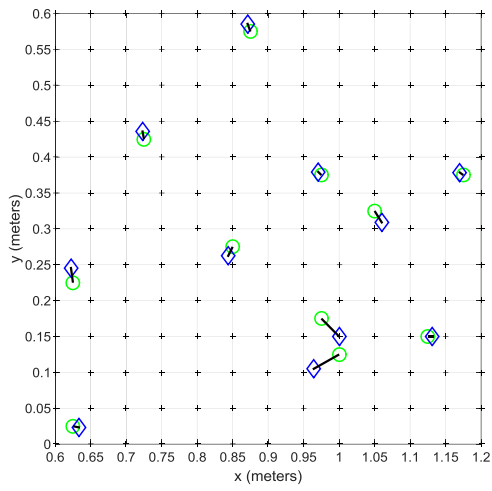
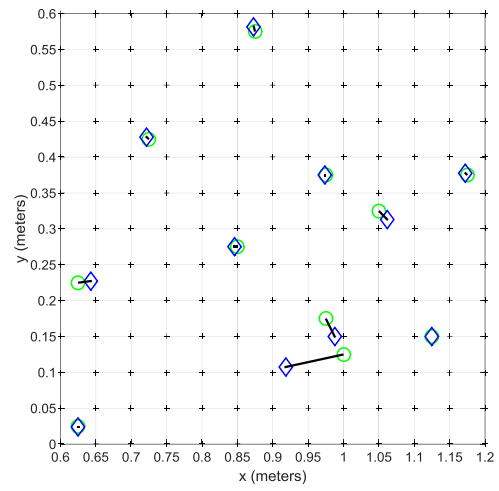


Figure 4.19 OM2 impact localization results for varying NAO.

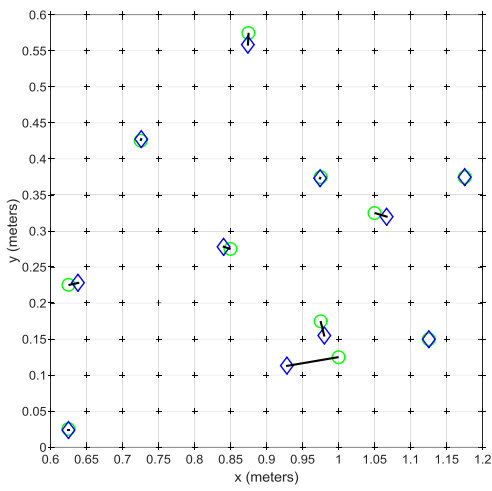
As a result of the reduction in maximum localization error, the OM2 average localization error is found to be considerably improved in comparison to the OM1 results. From 10 to 120 additional outliers, the average localization errors are calculated to be about or less than 20.0 mm. The overall average localization error is less than 40.0 mm and the maximum occurs when NAO is set to 180. OM2 has successfully estimated most of the impact location for varying NAO cases close to the actual impact location. The results for the 11 impact test points for OM1 with 20, 60, 80 and 120 NAO are visualized in Figure 4.20 (a-d). It is observed that except for Impact Test Point 8, increasing the NAO results in better impact localization performance.



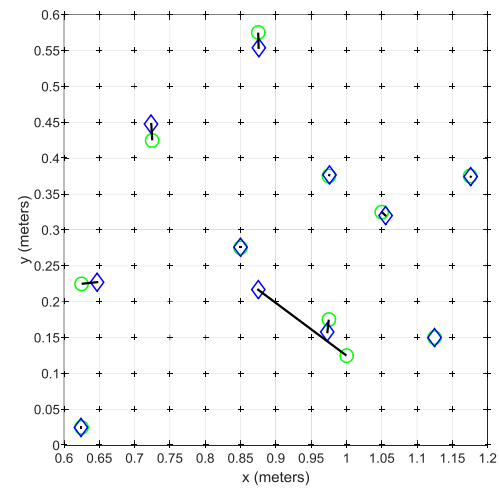
a) NAO: 20



b) NAO: 60



c) NAO: 80



d) NAO: 120

Figure 4.20 OM2 impact localization visualization for varying NAO cases.

Consequently, from present parametric study results for OM2 algorithm it can be concluded that increasing the NAO parameter can further enhance the impact localization results and, furthermore, the Euclidean distance threshold can narrow down the selected locations closer to the actual impact location. Although the Euclidean distance threshold minimizes the localization error, the present technique employed to reject location farther from the actual impact location may not be as effective for some impact test points when the NAO parameter is set to more than 20. However, through the parametric study the optimal No. of Additional Outlier values have been determined for OM1 and OM2 algorithm. The optimal results determined based on maximum localization error and average localization error are tabulated in Table 4.9.

Using 10 additional outliers, it is possible to lower the average localization error to 17.6 mm and 16.7 mm corresponding to OM1 and OM2 localization algorithms, while maintaining the maximum localization error results, as shown in Table 4.9 (a). Moreover, by further increasing the NAO parameter to 30 in the OM1 algorithm and 40 in the OM2 algorithm, the impact locations can be predicted more accurately as the average localization error is decreased to 17.3 mm and 14.2 mm, respectively, as shown in Table 4.9 (b). OM2 with 40 additional number of outlier parameter setting shows better average localization result than the RMS results [69] presented in Table 4.8.

Table 4.9 Optimal localization results based on the NAO parametric study.

a) Optimal Results Based on Maximum Localization Error		
	OM1: NAO = 10	OM2: NAO = 10
Maximum Error (mm)	35.4	35.4
Average Error (mm)	17.6	16.7
b) Optimal Results Based on Average Localization Error		
	OM1: NAO = 30	OM2: NAO = 40
Maximum Error (mm)	39.9	43.5
Average Error (mm)	17.3	14.2

OM2 is found to be highly effective in localizing impact test points on composite wing structure. Though the maximum error is 8.1 mm higher than the RMS localization result [69], the overall localization performance is considerably better than RMS and correlation method. The present parametric study has demonstrated that increasing the NAO parameter for impact location selection can help to more accurately predict the Impact Test Point. Furthermore, the OM with increased NAO parameter which results in overall improved localization performance is highly desired. Hence, further investigation done to lower the maximum localization error when increased NAO parameter was used is presented in the subsequent section.

4.3.5 OM1 and OM2 Localization with ‘k’ Limit

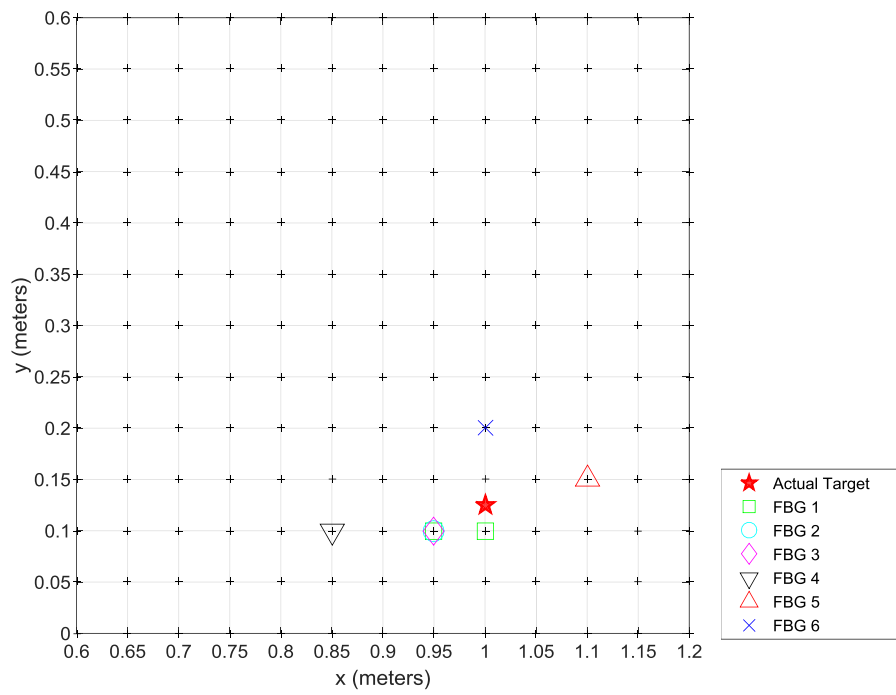
In the previous section, the NAO parametric study showed that increasing the NAO parameter can give better localization performance. Hence, using the 40 NAO resulted in significant reduction in average localization error. However, larger maximum error was obtained for Impact Test Point 8 using higher NAO values compared to the result obtained using 3 NAO. Therefore, the cause of the increase in localization error was investigated and is presented in this section.

Firstly, the number of detected locations for FBG1~6 were examined for 3 and 120 NAO cases using OM2 and the results are tabulated in Table 4.10. Using 3 NAO, two possible impact locations were selected for FBG1 and one location for FBG2~6 were selected. In total 7 possible impact locations were detected. Whereas, 120 NAO resulted in selection of 122 locations for impact location estimation; 7, 4, 6, 16, 23 and 66 locations by FBG1, FBG2, FBG3, FBG4, FBG5 and FBG6, respectively. The detected locations for the two cases of NAO are visualized in Figure 4.21.

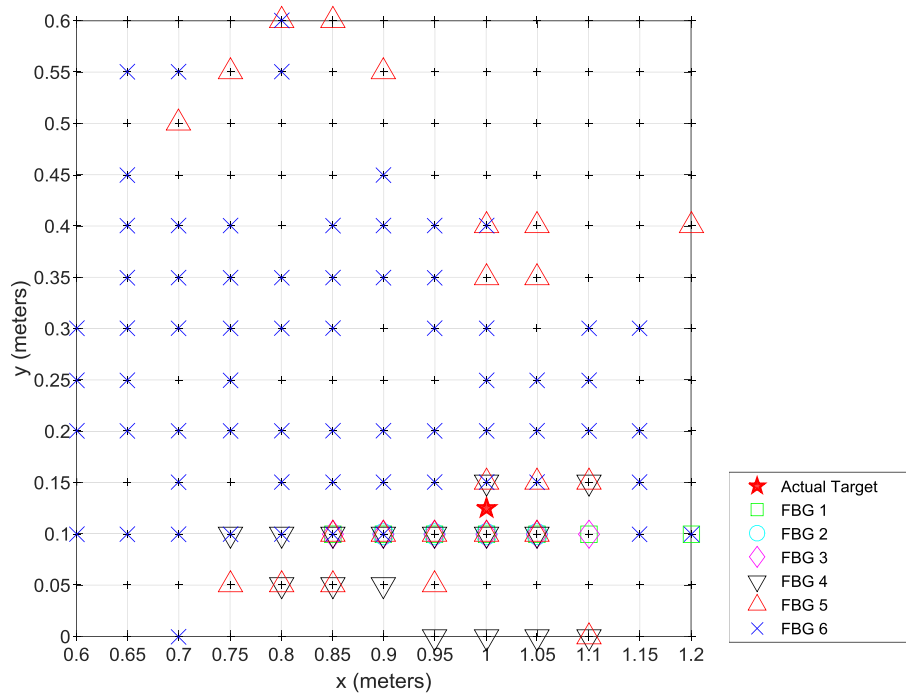
Figure 4.21 (a) shows the detected impact locations when 3 NAO were used. The visualization shows that most of the detected points are located close to the actual impact location. Figure 4.21 (b) shows the detected impact location obtained using 120 NAO. It can be seen that the detected locations are spread throughout the impact test region, and therefore the large localization error can be attributed to the large number of detected location which covers the entire impact region. In order to determine the variation in the number of detected location by FBG1 and FBG6, the N. of Outliers from reference point 1 to 169 for FBG1 and FBG6, shown in Figure 4.22, are examined.

Table 4.10 N. of detected locations for 3 and 120 NAO.

NAO	N. of Detected Locations	
	3	120
FBG1	2	7
FBG2	1	4
FBG3	1	6
FBG4	1	16
FBG5	1	23
FBG6	1	66
Total	7	122



a) NAO: 3



b) NAO: 120

Figure 4.21 Visualization of detected impact locations.

Figure 4.22 (a) and (b) show that the N. of Outliers counted for FBG1 compared to FBG6 is found to have large variations, from about 100 to 700 outliers, for varying reference point. Whereas the variation for FBG6 is not as significant. Consequently, for both of these sensors when the NAO is set to low values, such as 3, gives better localization results in comparison to using large NAO value. For FBG6, the N. of Outliers counted at varying reference point ranges between about 350 to 600. Therefore, large NAO, such as 120, leads to false detection of reference points farther away from the actual impact location as possible impact locations.

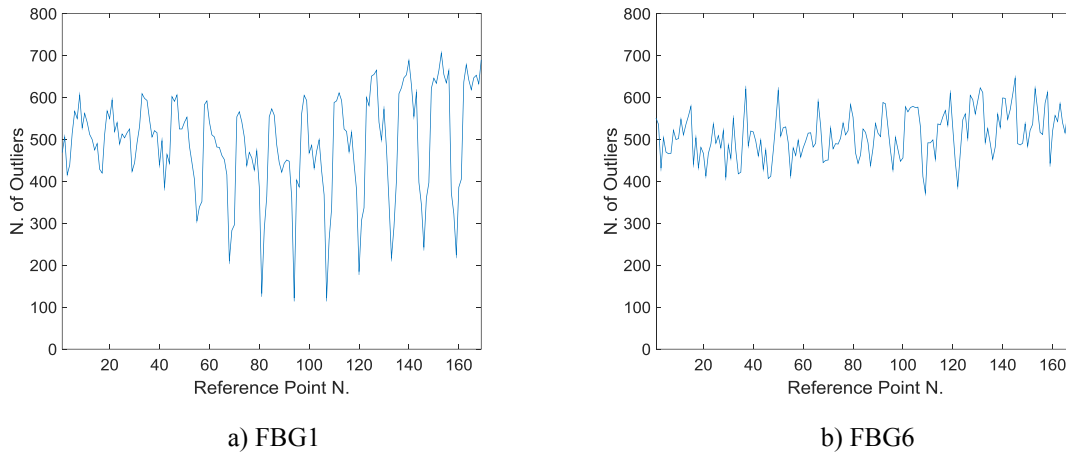


Figure 4.22 N. of Outliers computed for signals from FBG1 and FBG6 at various Reference Point N.

Furthermore, Table 4.10 shows that increasing the N. of Outliers parameter does not necessarily lead to significant increase in the number of detected location for all of the sensors. For instance, FBG1, FBG2 and FBG3 each detect less than eight impact locations. For that reason, if the OM is modified such that when the NAO parameter is increased, restricting the number of detected locations per sensor can help to improve the localization performance. Therefore, the OM1 and OM2 are modified such that each sensor is allowed to detect only seven number of possible impact locations as shown in Figure 4.23.

Step 3

Impact Location Search
Detected Location:

$$N_{l,i} = n_l (OL(i) \leq \min (OL_{\min}(i)) + NAO)$$

Figure 4.23 Modified Step 3 for limited number of detected location per FBG sensor.

In Step 3, the outliers obtained using sensor, ‘i’, at reference point, ‘n’, is compared with the location detection criteria: minimum N. of Outliers obtained using sensor, ‘i’, plus NAO. The modified Step 3, shown in Figure 4.23, ensures the number of detected location, ‘N_l’, by each sensor, ‘i’, does not exceed the limit, k. The OM1 and OM2 algorithms were updated with the modified Step 3, as shown in Figure 4.24, and using limit, k =

7, the 11 impact test points on the composite wing were localized using these algorithms. The localization results obtained using the modified OM1 and OM2 are presented in Figure 4.25 and Figure 4.26.

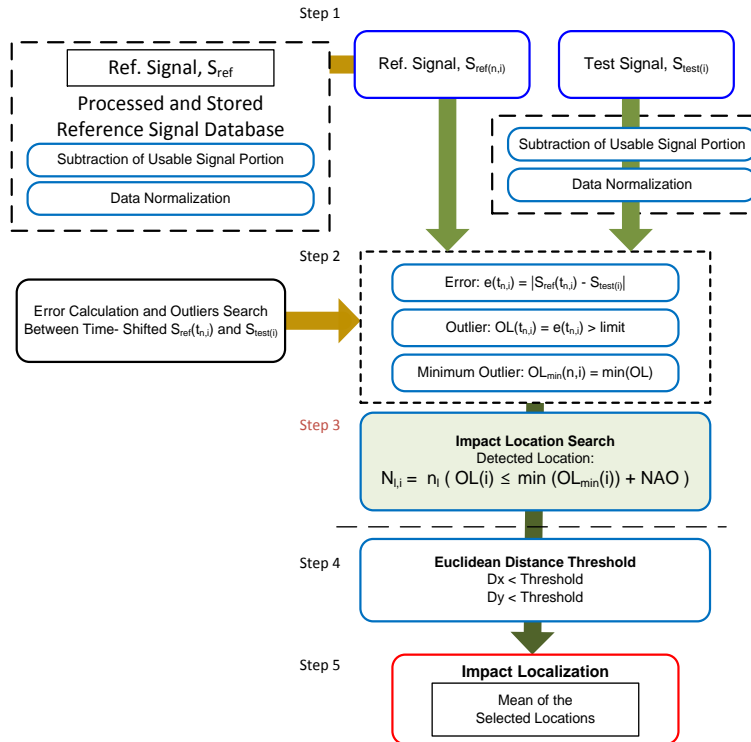
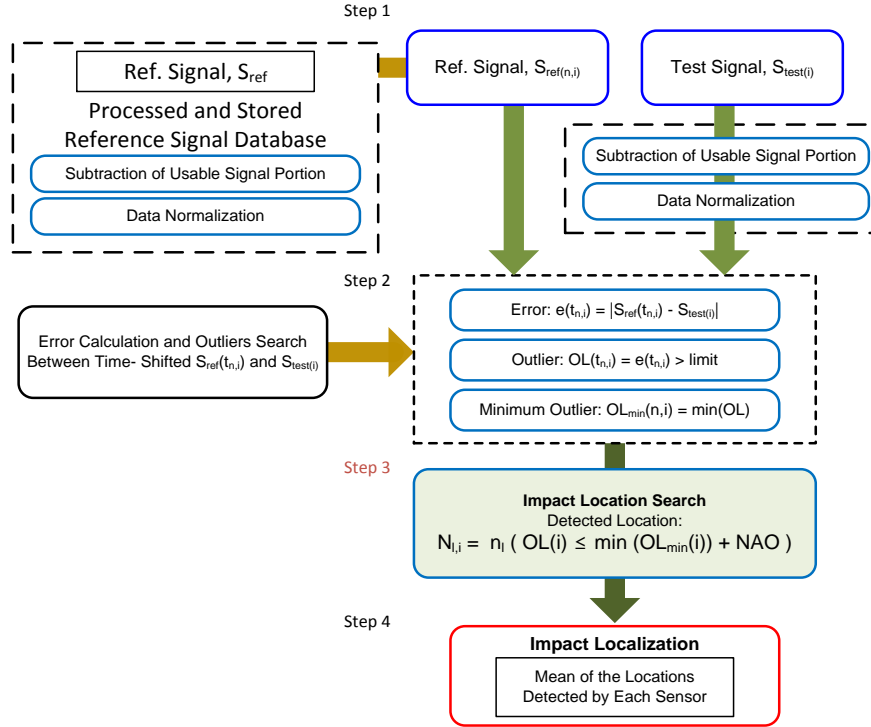


Figure 4.24 Modified OM1 and OM2 algorithm flowchart.

The NAO parametric study performed using the modified OM1 with number of allowed impact location limit, $k = 7$, shows improved impact localization performance. In comparison to the OM1 results shown in Figure 4.17, a decrease in the maximum localization error was achieved as the NAO was increased. The maximum localization error of about 84.0 mm occurred when 50 and 60 NAO were used, compared to about 160.0 mm error using the OM1 algorithm. Whereas, for other cases of NAO the maximum location error of about 40.0 mm was obtained. Similarly, the average localization error of less than 20.0 mm was obtained for all the parametric study cases of NAO from 10 to 180. Incorporating the allowable impact location limit, k , in the OM1 algorithm shows significant improvement in the localization results.

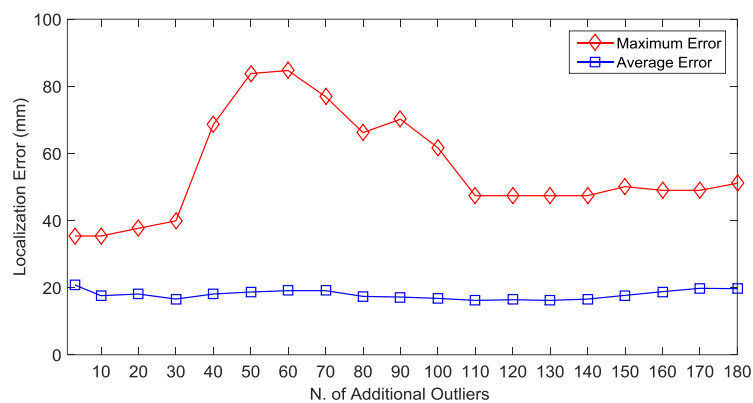


Figure 4.25 OM1 with k number of selected location impact localization results for varying NAO.

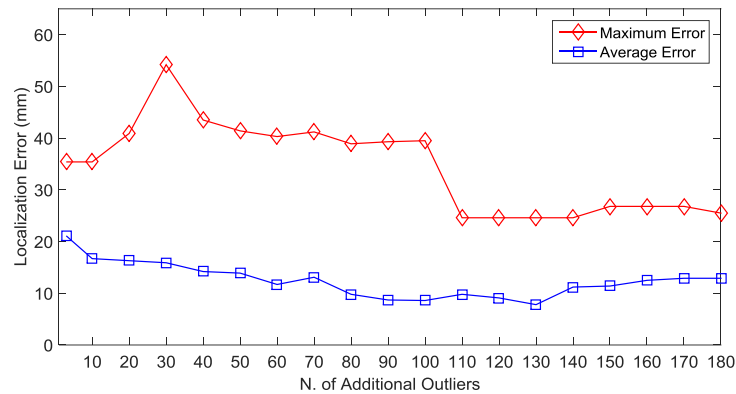


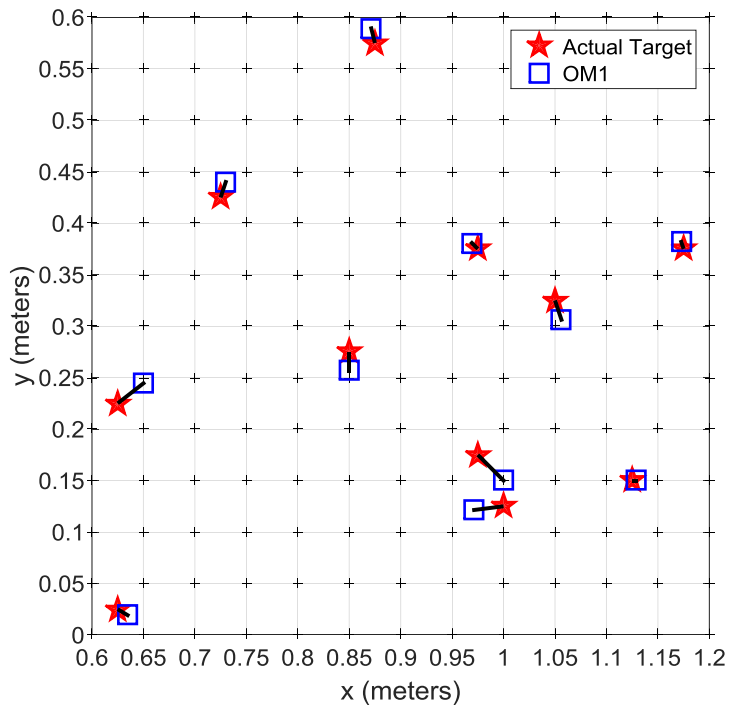
Figure 4.26 OM2 with k number of selected location impact localization results for varying NAO.

Likewise, localization of the 11 impact test points using the modified OM2 resulted in sharp decrease in maximum localization error value compared to the OM2 results shown in Figure 4.19. The maximum localization error peak of 54.2 mm occurs when 30 NAO was used for detecting the impact location. The maximum localization error of about 40.0 mm was obtained when the NAO parameter used ranged from 10 to 100. Increasing the NAO parameter beyond 100 leads to further decrease in the obtained maximum localization error, to about 25.0 mm.

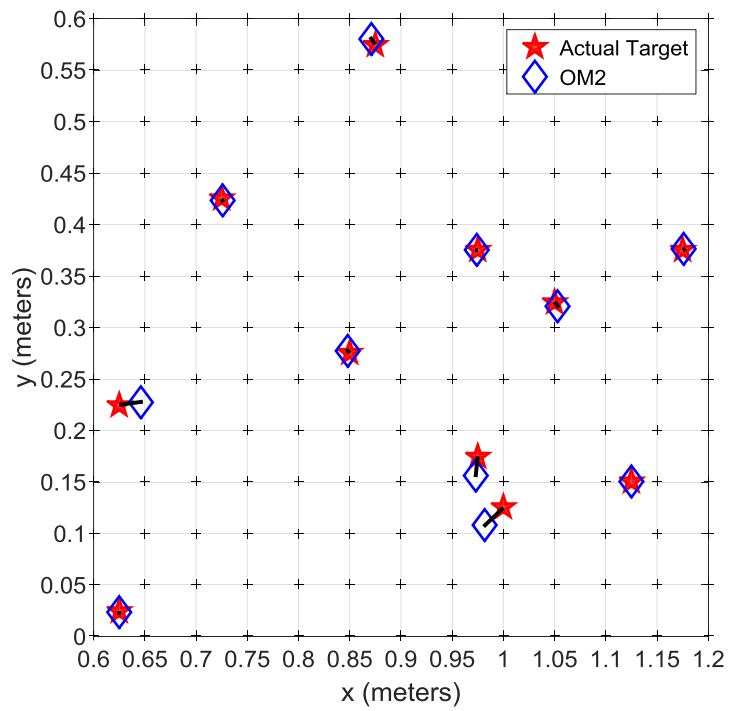
Similarly, significant decrease in the maximum localization error also resulted in considerable decrease in the average localization error, from 21.1 mm to 7.8 mm, by varying the number of additional outlier from 3 to 130, correspondingly. Average localization error of about 15.0 mm was obtained when 10 to 70 NAO were used. Whereas, when 80 to 180 NAO were used the average localization error of about 10 mm was achieved. Moreover, the modified OM1 and OM2 localization result compared to OM1 and OM2 algorithms presented in section 4.3.4 shows improved results.

Table 4.11 OM with limited number of selected location based impact localization results comparison with RMS and Correlation localization results.

Impact Test Point	Inner Wing Localization Results Comparison (mm)			
	RMS [69]	Correlation [69]	OM1: NAO = 10	OM2: NAO = 130
1	8.3	8.3	11.2	1.8
2	35.4	35.4	31.7	21.3
3	11.8	18.6	15.8	1.7
4	16.7	25.0	17.9	3.3
5	18.6	30.1	14.7	6.9
6	35.4	35.4	35.4	18.4
7	8.3	0.0	8.2	0.8
8	8.3	11.8	28.8	24.6
9	11.8	16.7	19.8	5.0
10	8.3	16.7	3.6	0.0
11	0.0	0.0	7.2	1.6
Maximum Error	35.4	35.4	35.4	24.6
Average Error	14.8	18.0	17.6	7.8
SD	10.7	12.0	10.0	8.7



a) Modified OM1 localization results using 10 NAO



b) Modified OM2 localization results using 130 NAO

Figure 4.27 Visualization of OM with limited number of selected location based localization results.

The optimal maximum localization error results of 35.4 mm and 24.6 mm, and average localization error of 17.6 mm and 7.8 mm, using the modified OM1 and OM2 were obtained when 10 and 130 NAO were selected, respectively. The optimal localization results are compared with the RMS and correlation impact location results [69] in Table 4.11, and the estimated impact locations of the 11 impact test points are visualized in Figure 4.27. The modified OM2 maximum localization error was 10.8 mm less than the results obtained using RMS, correlation and OM1 impact localization algorithm, respectively. Whereas, the modified OM2 average localization error was 7.0 mm, 10.2 mm and 9.8 mm less than the results obtained using RMS, correlation and OM1 impact localization algorithms, respectively. Significant decrease in the localization error was achieved using the modified OM2 algorithm.

In conclusion, improved results were obtained for more complex structures such as composite wings. The OM1 and OM2 algorithms which were modified to limit the number of selected location detected by each sensor provided better impact localization performance. Furthermore, the modified OM2 significantly improved the localization results compared to the RMS and correlation method. In the subsequent section, the impact localization test performed on the upper and lower wing structure is presented.

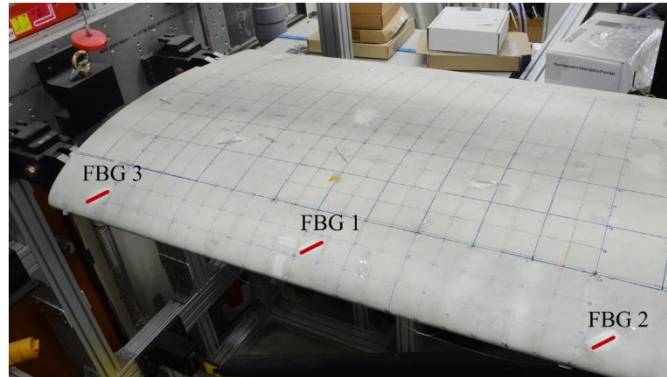
4.3.6 Application of OM1 and OM2 Algorithm with k Limit on Complex Wing Surface

The OM based impact localization algorithms presented in the earlier sections are further validated by localizing impact test points on a more complex structural geometry, such as the leading edge, and also for monitoring impacts on the upper and lower surface of a composite wing of Jabiru UL-D aircraft (Jabiru Aircraft Pty Ltd, Australia), shown in Figure 3.7, using 1D array sensors configuration attached near the leading edge section of the wing. The impact localization experiment was performed on the upper and lower surface of the composite wing. The experimental set-up is presented in Figure 4.28. The test section is divided into upper surface test section and the lower surface test section from the leading edge of the wing and covers an area of 1000 mm \times 1400 mm. The schematics of the upper and lower wing surface test section is shown in Figure 4.29. Additionally, the spar region is represented by shaded region between the dash-dot lines shown in Figure 4.30.

Three multiplexed acrylic coated FBG sensors, with center wavelength of 1544.6 nm, 1547.6 nm and 1550.6 nm, were attached close to the leading edge on the upper surface of the wing in 45° angle. As in the previous sections, the signals from the FBG sensors were sampled at 100 kHz using the high speed interrogator, SFI-710 (FIBERPRO Inc., Korea). The impact test region on the upper and lower surface consists of training signals from 609 reference points, which were located 50.0 mm apart from each other. It takes over 6 hours to acquire all of the training signals. These training signals were used to estimate the locations of 10 impact test points on the upper surface and 10 impact test points on the lower surface of the composite wings. The impact test points coordinates are tabulated in Table 4.12 and visualized in Figure 4.30.



a) Data acquisition system



b) Wing test section

Figure 4.28 Experimental set-up.

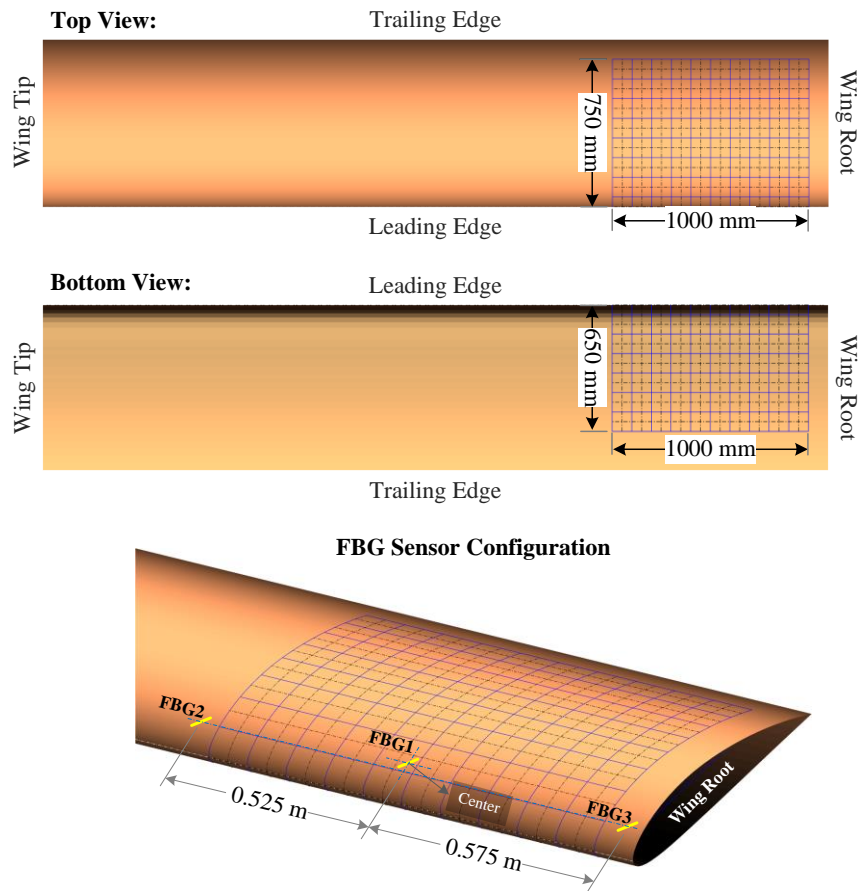


Figure 4.29 Schematics of the upper and lower wing surface impact test section.

Table 4.12 Upper and lower surface impact test point coordinates.

Impact Test Points on the Wing Surface					
Wing's Upper Surface			Wing's Lower Surface		
N.	x (mm)	y (mm)	N.	x (mm)	y (mm)
1	75	1125	11	70	80
2	179	729	12	171	424
3	228	801	13	224	625
4	330	1078	14	479	525
5	575	925	15	575	425
6	725	1375	16	726	275
7	800	675	17	800	570
8	875	1175	18	876	374
9	925	1275	19	935	470
10	1000	925	20	999	621

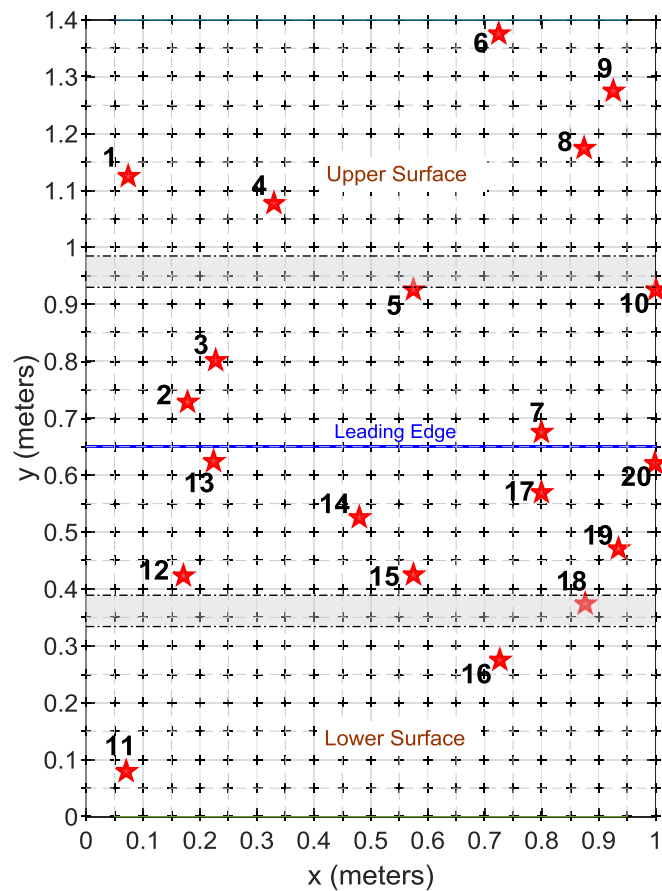


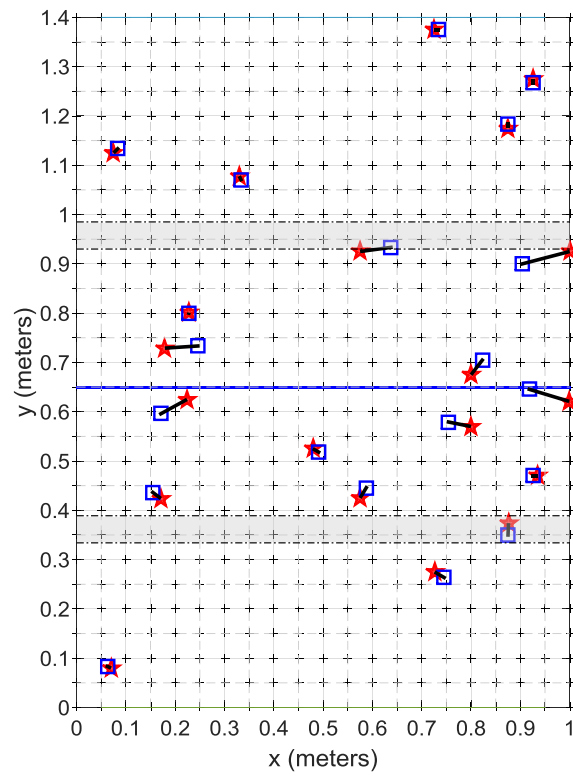
Figure 4.30 Visualization of upper and lower surface impact test points.

4.3.7 Results and Discussion

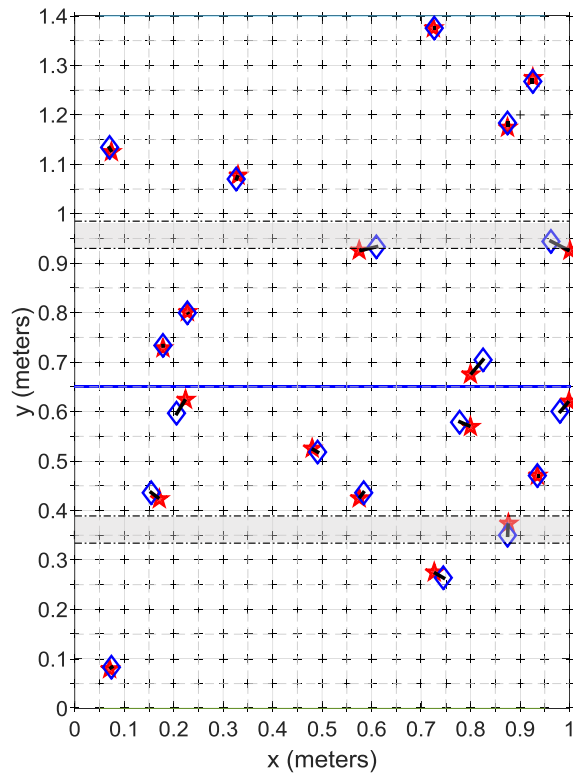
The localization on the upper and lower surface of the composite wing were done using the OM1 and OM2 algorithms presented in 4.3.5, and illustrated in Figure 4.24. The impact localization of the 20 impact test points, shown in Figure 4.30, on the upper and lower surface of the wing were done by setting the error threshold value to 1.5 nm, NAO to 100 and number of detected location by each sensor, $k = 4$. The location of the impacts detected using OM1 and OM2 are shown in Table 4.13 and the detected points are visualized in Figure 4.31. The localization error results obtained using OM1 and OM2 algorithms for the 20 impact cases are tabulated in Table 4.14.

Table 4.13 OM1 and OM2 based predicted impact location coordinates.

Impact Test Point		Actual Location		OM1 Results		OM2 Results	
		x (mm)	y (mm)	x (mm)	y (mm)	x (mm)	y (mm)
Upper Surface	1	75.0	1125.0	83.3	1133.3	70.0	1133.3
	2	179.0	729.0	245.8	733.3	178.6	733.3
	3	228.0	801.0	227.8	800.0	228.6	800.0
	4	330.0	1078.0	333.3	1070.8	327.3	1070.8
	5	575.0	925.0	637.5	933.3	610.0	933.3
	6	725.0	1375.0	733.3	1375.0	727.3	1375.0
	7	800.0	675.0	822.7	704.5	825.0	704.5
	8	875.0	1175.0	875.0	1183.3	875.0	1183.3
	9	925.0	1275.0	925.0	1266.7	925.0	1266.7
	10	1000.0	925.0	904.2	900.0	962.5	944.4
Lower Surface	11	70.0	80.0	62.5	83.3	75.0	83.3
	12	171.0	424.0	154.5	436.4	154.5	436.4
	13	224.0	625.0	170.8	595.8	206.3	595.8
	14	479.0	525.0	490.9	518.2	490.9	518.2
	15	575.0	425.0	587.5	445.8	583.3	436.4
	16	726.0	275.0	745.5	263.6	745.5	263.6
	17	800.0	570.0	754.2	579.2	778.6	579.2
	18	876.0	374.0	875.0	350.0	875.0	350.0
	19	935.0	470.0	925.0	470.0	935.7	470.0
	20	999.0	621.0	918.2	645.5	981.3	600.0



a) OM1 impact localization results



b) OM2 impact localization results

Figure 4.31 Visualization of impact location detected on wings' upper and lower surface.

Table 4.14 Impact localization on upper and lower surface using 1D array sensor configuration.

Upper Surface Localization Results (mm), k = 4			Lower Surface Localization Results (mm), k = 4		
Impact Test Point	OM1	OM2	Impact Test Point	OM1	OM2
1	11.8	9.7	11	8.2	6.0
2	67.0	4.4	12	20.6	20.6
3	1.0	1.2	13	60.6	34.1
4	7.9	7.7	14	13.7	13.7
5	63.1	36.0	15	24.3	14.1
6	8.3	2.3	16	22.5	22.5
7	37.3	38.7	17	46.7	23.3
8	8.3	8.3	18	24.0	24.0
9	8.3	8.3	19	10.0	0.7
10	99.0	42.2	20	84.4	27.5
Maximum Error	99.0	42.2	Maximum Error	84.4	34.1
Average Error	31.2	15.9	Average Error	31.5	18.7
SD	32.1	15.4	SD	23.5	9.6

Overall localization error using OM1 were found to be satisfactory except for Impact Test Point 2, 5, 10, 13 and 20. These five impact cases were localized over 50.0 mm away from the actual impact locations. Figure 4.31 (a) shows that most of these impact test points, Impact Test Point 2, 13, 20 with large errors are located in the leading edge region. Also, two of these impact test points, Impact Test Point 10 and 20, are located at the edge of the impact test region.

Impact that takes place on the edge of the impact test region are more prone to large error, since the number of selected locations are more likely to be located farther out from the actual impact location due to lack of reference points surrounding the impact location at the edge of the test region. As illustrated in Figure 4.32, Impact Test Point 10 is located at the edge of the impact test region, therefore the selected location spans farther out, towards the left side of the impact, from the actual impact location. Based on the outlier assessment, 12 impact locations were selected, however, among these 12 locations only 5 of them were located within 50.0 mm from the actual impact location. Since the impact location is on the edge, the remaining selected location spans out farther from the actual impact location.

Consequently, the localization errors are considerably higher at Impact Test Point 10 and 20, 99.0 mm and 84.4 mm, respectively. Regardless of some impact test points being estimated with large localization error, the modified OM1 was able to effectively localize most of the impact test points with localization error below

25.0 mm, and overall with average localization error of 31.2 mm and 31.5 mm for the upper and lower surface of the wing, respectively.

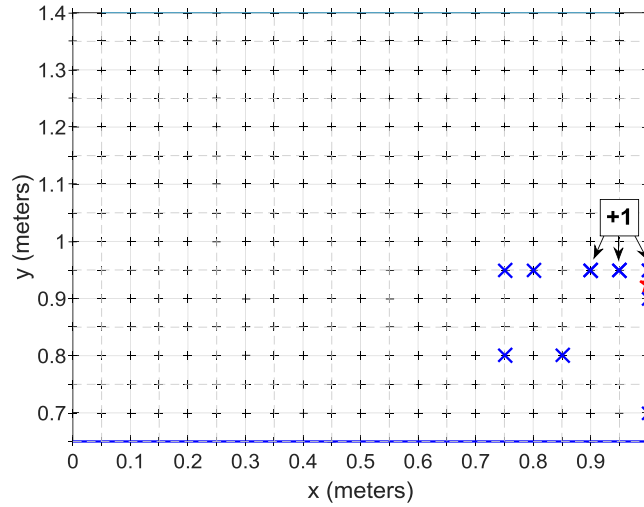


Figure 4.32 Locations selected for Impact Test Point 10 by OM1 algorithm.

Nevertheless, using the modified OM2 algorithm presented in Figure 4.24 (b) all of the 20 impact test points were localized with localization error of less than 50.0 mm. Moreover, using the OM2 algorithm, the impact test points located at the edge of the impact test region were detected closer to the actual impact location; the localization error at Impact Test Point 10 and 20 were considerably reduced to 42.2 mm and 27.5 mm, respectively. Moreover, OM2 impact localization results show that the Impact Test Point 10 is also the location with the maximum localization error. However, significant improvement was achieved using the OM2 algorithm; the 20 impact test points were estimated with a total average error of 17.3 mm. The results show that the impact test points located at the upper surface of the wing were better localized than the ones located on the bottom surface of the wing; impact test points on the upper surface were localized with an average error of 15.9 mm, whereas on the lower surface the impact test points were localized with an average error of 18.7 mm

The localization results obtained using OM algorithms presented in this section and in the previous section demonstrates the effectiveness of utilizing outliers approach to localize impact location on composite structure. Additionally, one of the other main advantage of using the outlier based impact localization algorithm is the time the OM algorithm takes to localize an impact point. For instance, using a computer system with an Intel(R) Core(TM) i7-4770 CPU @ 3.40GHz with 16GB RAM memory, on average it took about 13.2 s, to process and analyze the test signal and the 609 reference signals, with three FBG sensor signals each, to localize an impact point on the wing's upper/lower surface.

The present results are compared with reference results [82] obtained using cross-correlation based impact localization algorithm. Kim [82] performed three sensor configuration parametric study and showed that the average of all maximum localization error was 52.6 mm and average error was 16.8 mm, whereas the best

case sensor configuration results showed 26.2 mm maximum localization error and 14.6 mm average error. Comparison of the present results shows similar performance when three FBG sensors are used for impact localization algorithm. Furthermore, using three FBG sensors and the cross-correlation based impact localization technique took 33.8 s to estimate the impact location [82], whereas the present outlier method took 13.2 s to localize the impact point on the composite wing. Therefore, the present outlier method demonstrates it is an effective technique to localize low velocity impact on complex composite structures such as aircraft wing.

Table 4.15 Localization results comparison.

Three FBG Sensor Configuration	OM2	Cross-Correlation [82]:	
		Average Result [82]	Optimal FBG Configuration [82]
Maximum Error (mm)	42.2	52.6	26.2
Average Error (mm)	17.3	16.8	14.6
Time (s)	13.2	33.8	33.8

4.4 OM3: Simplified Error Outlier Based Localization Algorithm

In this section, the error outlier based impact localization algorithm was developed to localize impact on complex composite structures. The novel method developed to localize impact location based on error outlier assessment demonstrates quick and effective localization of impact test points on composite plate and composite wing structures. The OM algorithms presented in earlier section, although they show good localization results, consists of several parameters which significantly influence the localization results; such as NAO parameter, k parameter and error threshold parameter. The values of those parameters are required to be determined manually, therefore it can be time consuming to determine the suitable values for each of those parameters. OM impact localization algorithm with fewer parameters requiring manual input is desirable so that it can be used flexibly for localizing impact on various different type of structures. Therefore, the OM3 impact localization algorithm using statistically determined distance threshold to reduce the number of such parameters were investigated and the proposed methods are presented in this section.

In the previously developed OM algorithm, the possible impact location, 'I', is selected if the N. of Outliers at reference point, 'n', is the lowest or if it is within the range below the minimum N. of Outliers plus NAO criteria, set in Step 3. The NAO criteria provides a good measure to select the possible impact location region, however the previous results have shown that by setting allowable number of selected detected location, k number of reference points with least N. of Outliers, can give good localization results as well. Therefore, Step 4 of the OM is modified to select the location based on the latter method and not to consider the NAO. Furthermore, in Step 4 of previously developed OM2 the Euclidean distance threshold was used to select likely

impact locations from the list of impact locations identified by the algorithm in Step 3 of OM1. In this section, several different statistically determined distance threshold used for filtering likely impact locations in Step 4 are listed below:

- Standard Deviation threshold,
- Median Absolute Deviation threshold, and
- weighted Median Absolute Deviation threshold.

4.4.1 Overview of OM3 Based Impact Localization Algorithms

4.4.1.1 OM3 Algorithm

This method is a variation of the OM2 algorithm, in which at Step 3 the outlier location with minimum number of outlier is first selected, and subsequently ‘k’ number of additional locations with minimum N. of Outliers plus NAO criteria is used for location selection. The OM3 algorithm differs from OM1 and OM2 algorithms, as the NAO criteria is not taken into consideration, i.e., in this method the location selection is no longer based on minimum N. of Outliers plus NAO condition. Instead it directly selects k number of location with least N. of Outliers.

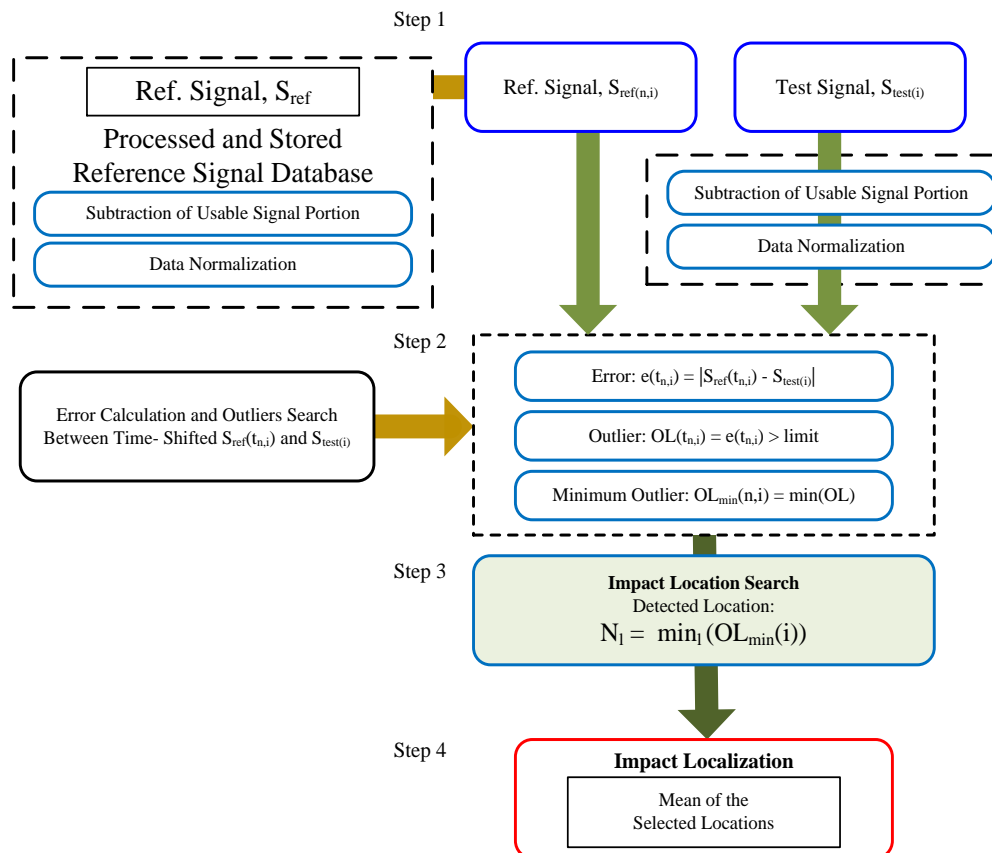


Figure 4.33 OM3 impact localization flowchart.

The k minimum outlier criteria for impact location detection without the NAO criteria is illustrated in Figure 4.33. In Step 3, the outliers obtained using sensor, 'i', at reference point, 'n', is compared with the location detection criteria: minimum N. of Outliers obtained using sensor, 'i'. After the first location with the minimum number is found, this process is repeated until the number of detected location ' $N_1 = N_k$ '. Therefore, from each sensor 'k' number of locations will be chosen, and the total number of impact location selected by Step 3 will be equal to number of sensors, 'i', times the number of allowed location limit, 'k'.

4.4.1.2 OM3 with SD Threshold

In the OM3 with SD threshold based impact localization method, once the possible impact locations are determined using Step 3 these locations are filtered using the Standard Deviation (SD) threshold in Step 4 to determine whether to select or reject the location for estimating the impact location. The overview of the OM3 with SD threshold based impact localization algorithm is presented in Figure 4.34.

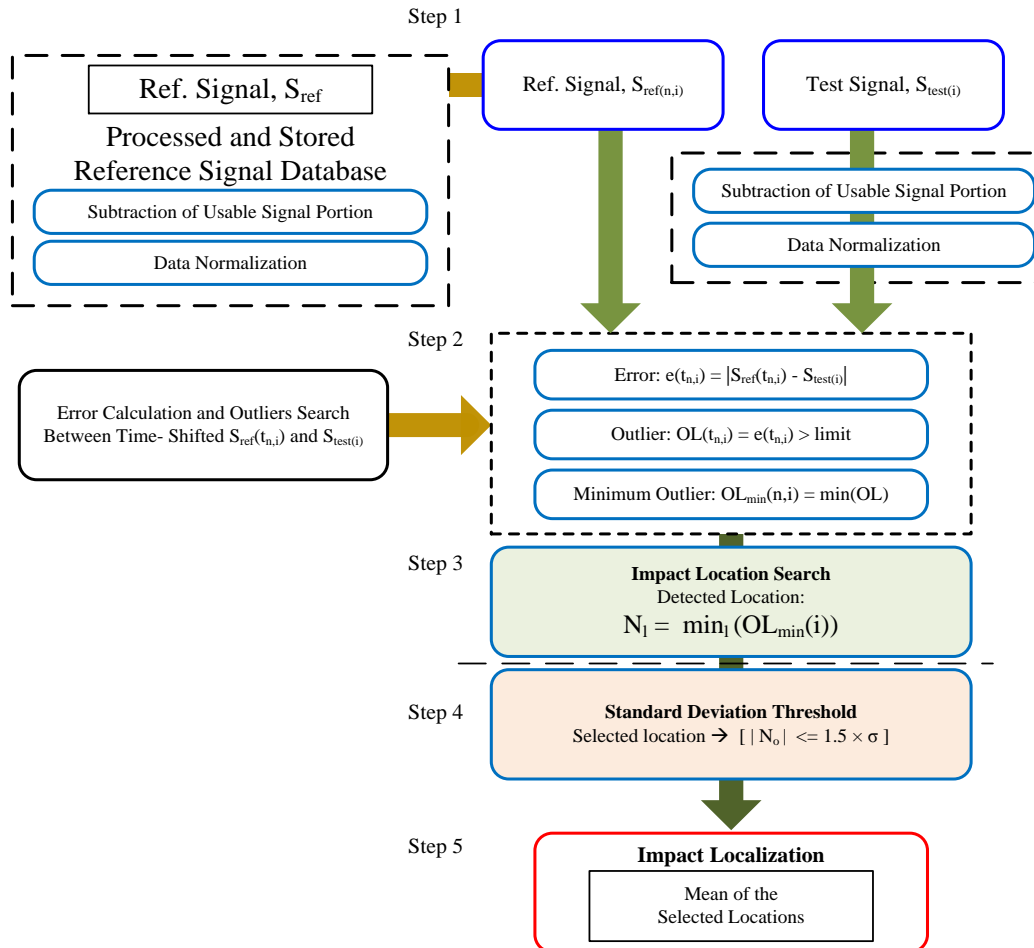


Figure 4.34 OM3 with SD threshold impact localization algorithm flowchart.

In Step 4 of the OM3 with SD threshold algorithm, firstly the standard deviation, σ , of the impact locations 'N' detected by all the FBG sensor are determined and then the location selection SD threshold is

calculated by multiplying the standard deviation, σ , times 1.5. In order to select or reject the detected location 'N', the absolute zero-mean values, ' $|N_o|$ ', of the detected locations 'N' are calculated and each of the detected location is compared with the standard deviation threshold. If the absolute zero-mean value of the detected location is less than or equal to the SD threshold then the location will be selected, otherwise the location will be discarded. This process of zero-mean value comparison with the SD threshold is done for all of the selected locations 'N'. The selected locations 'N' are once more filtered using this process. Finally, the locations that are selected after completing the comparison process of all the detected locations, the impact location is estimated by calculating the mean of the selected locations in the final Step 5.

$$N_o = N - \bar{N} \quad (9)$$

$$\sigma = \sqrt{\frac{1}{k} \left(\sum_{i=1}^k (N_i - \bar{N})^2 \right)} \quad (10)$$

$$\sigma_{Thres} = 1.5 \times \sigma \quad (11)$$

4.4.1.3 OM3 with MAD Threshold

An alternative to the Euclidean distance threshold and the standard deviation threshold is the Median Absolute Deviation (MAD) threshold [104]. In comparison with the SD threshold which uses the mean of the detected locations, ' N_i ', the MAD threshold takes the median location calculated from the set of detected locations, ' N_i ', into consideration for the impact location selection. The MAD value is computed by subtracting the median from each detected location and then taking absolute values. Then the MAD threshold, MAD_{Thres} , is computed by dividing the MAD value by 0.6745 and then multiplying it by 1.5. The MAD threshold is applied for filtering the detected location if the standard deviation of the detected locations is greater than 30.0 mm and this process is repeated at most three times in Step 4.

$$MAD = \text{median} (|N_k - \text{median}(N_i)|) \quad (12)$$

$$MAD_{Thres} = 1.5 \times \frac{MAD}{0.6745} \quad (13)$$

Once the possible impact locations, ' N_i ', are determined using Step 3, these locations are filtered in Step 4 using MAD threshold criteria. The Step 4 with MAD threshold based location selection criteria is illustrated in Figure 4.35. The detected location, ' N_k ', is selected if the absolute value of the impact location, ' N_k ', subtracted by median of all the detected locations, $\text{median}(N_i)$, $|N_k - N_i|$, is less than or equal to the MAD threshold. The filtering process is repeated for all the detected locations. All the locations that fulfill the MAD threshold are then used to finally estimate the impact location in Step 5.

$$|N_k - \text{median}(N_i)| \leq MAD_{Thres} \quad (14)$$

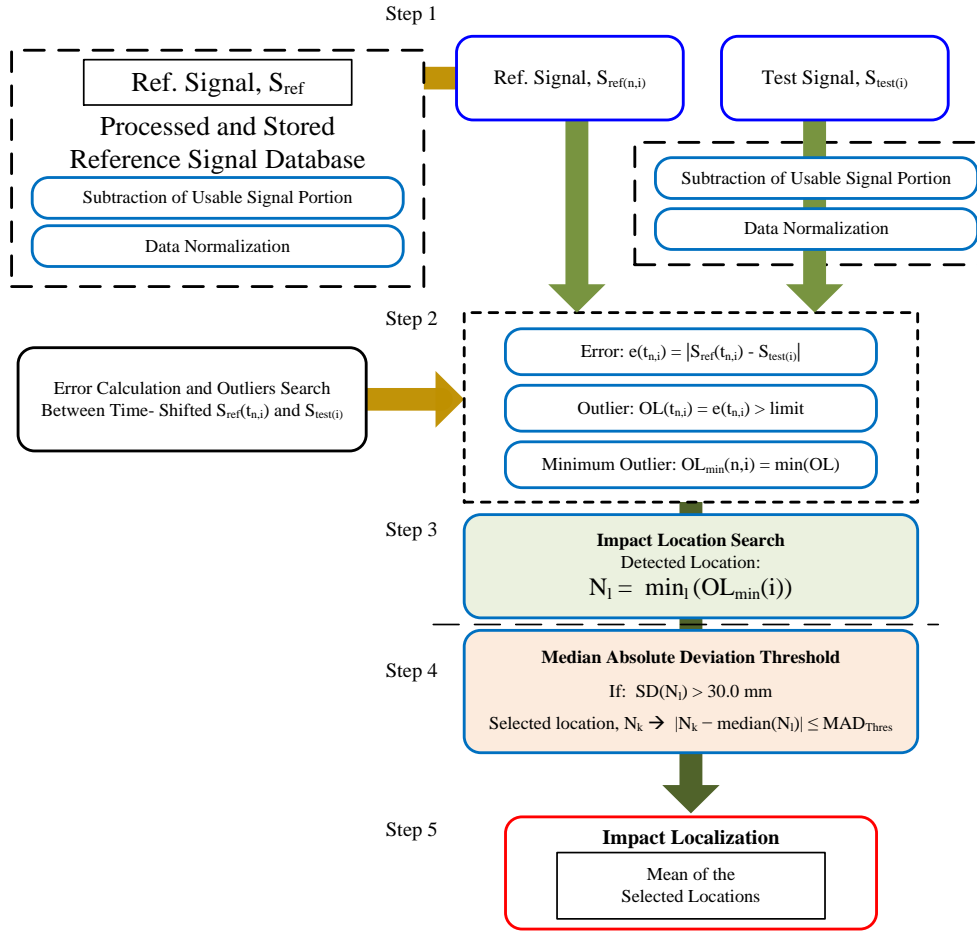


Figure 4.35 OM3 with MAD threshold impact localization algorithm flowchart.

4.4.1.4 OM3 with Weighted MAD Threshold

In order to obtain similar localization results for varying k values, weight based location selection criteria is incorporated in the OM with MAD threshold impact localization algorithm presented in Section 4.4.1.3. Since, the first location detected by the OM is the reference point with the least number of outliers, it is assigned the maximum weight and the subsequently detected locations are assigned less weight. The weight, W , for detected location number ' l ' is set to the maximum number of allowed location as follows:

$$W_l = k - l + 1, \quad (15)$$

where ' l ' is the detected location order from 1 to k . Thus, for the first detected location $l = 1$ the weight is maximum, $W_1 = k$. For instance, if k is set to 10, the first location will be considered 10 times, second detected location will be considered 9 times and so on until the last location, $l = 10$, which will only be considered once. As a result, when the number of allowed location, $k = 10$, is used a total of 55 locations will be used to filter and select the impact location for the final impact location in Step 5. The OM3 algorithm with the weighted MAD threshold is illustrated in Figure 4.36.

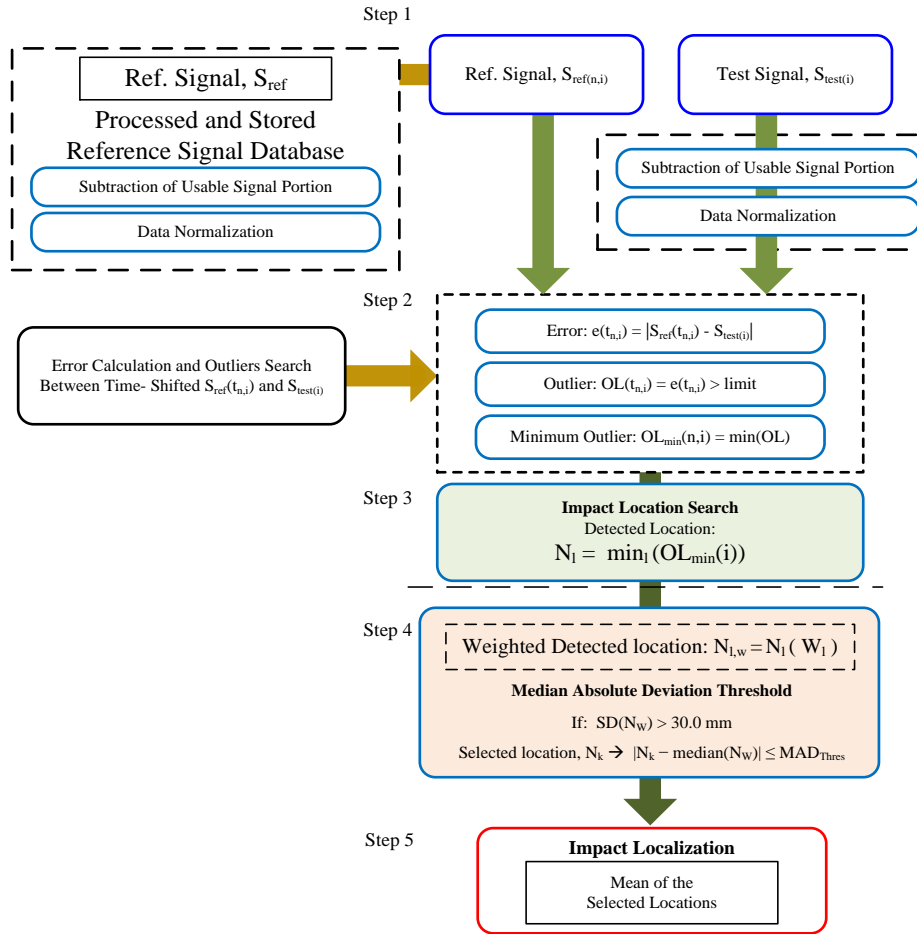


Figure 4.36 OM3 with weighted MAD threshold impact localization algorithm.

4.4.2 Application of OM3 Algorithms on Complex Wing Test Region

Impact localization algorithms based on OM3 algorithm with SD, MAD threshold and weighted MAD threshold were used to localize impact test points on the upper and lower surface of the composite wing for the test configuration presented in Section 4.3.6. The 20 impact locations, tabulated in Table 4.12, were used to verify the OM3 algorithms localization performance. Impact localization of the 20 impact test points on the upper and lower wing surface were done using the OM3 algorithm, OM3 algorithms with SD, MAD threshold and weighted MAD threshold, and the obtained localization results are presented in this section.

4.4.2.1 Localization Using OM3 Algorithm

The OM3 localization results presented in Table 4.16 shows that the 20 impact test points were well localized. Lower values of number of allowed location, k , yields better localization performance than higher value of k . For instance, using $k = 2$, the error value of the maximum localization error was the lowest, 71.2 mm, and similarly using k value of 1, 3 and 4, limits the maximum localization error to less than 100.0 mm. Whereas, for higher k values, the maximum error value is found to be larger than 100.0 mm. The largest localization error

of 191.3 mm occurs at Impact Test Point 10, when the k value is set to 10. Moreover, such poor localization performance occurs typically at impact test points near the leading edge and on the edge of the test region. These locations were previously identified as locations vulnerable to large localization errors in Section 4.3.6.

Table 4.16 OM3 impact localization results.

Impact Test Point		OM3 Algorithm Localization Results for Varying k Value (mm)									
		10	9	8	7	6	5	4	3	2	1
Upper Surface	1	35.9	41.9	42.9	35.5	27.4	19.0	11.8	16.2	37.3	11.8
	2	38.1	37.7	31.5	16.4	35.2	54.3	67.0	65.6	37.9	71.1
	3	21.3	16.4	22.0	12.4	11.3	7.3	15.5	5.9	3.2	11.4
	4	20.5	22.8	16.7	15.2	15.6	10.1	7.9	10.6	12.0	11.8
	5	83.6	73.9	68.9	72.9	66.9	55.2	63.1	66.8	71.2	63.5
	6	10.7	15.8	7.5	13.1	16.7	5.3	8.3	14.2	26.4	11.8
	7	29.2	29.0	54.1	59.1	53.6	26.1	41.2	25.0	26.4	25.0
	8	25.4	26.4	25.3	15.9	25.2	8.5	8.3	11.8	18.6	26.4
	9	18.0	14.4	8.8	6.9	8.3	7.1	8.3	3.9	18.6	26.4
	10	191.3	187.6	174.0	158.6	160.3	152.5	99.0	85.6	68.7	87.0
Lower Surface	11	28.5	22.8	23.9	8.7	3.4	3.3	8.2	4.7	12.7	4.7
	12	26.0	22.7	19.8	23.4	21.6	28.7	24.4	10.3	18.2	23.0
	13	68.9	74.3	65.6	58.4	63.1	72.9	60.6	28.1	25.0	26.1
	14	32.8	43.3	52.3	47.3	29.9	17.7	21.4	12.9	20.9	25.4
	15	43.3	42.2	34.4	31.6	22.2	20.1	24.3	19.6	8.3	11.8
	16	17.0	15.0	11.3	9.4	14.0	19.2	17.7	26.8	25.0	26.1
	17	52.3	70.7	62.3	30.6	29.7	40.6	46.7	46.4	58.5	33.5
	18	39.8	41.5	35.1	9.3	17.0	26.0	24.0	25.8	41.9	49.0
	19	39.0	29.2	15.2	18.7	25.1	12.1	5.9	5.1	7.5	25.0
	20	159.8	170.8	148.7	113.9	97.0	97.5	88.9	72.3	31.9	21.0
Max. Error		191.3	187.6	174.0	158.6	160.3	152.5	99.0	85.6	71.2	87.0
Avg. Error		49.1	49.9	46.0	37.9	37.2	34.2	32.6	27.9	28.5	29.6

Nevertheless, besides the impact location prone to large error, the algorithm predicts the impact location with reasonable accuracy for most of the other impact test points. Overall, by using any value of k between 1 to 10, the 20 impact test points on the upper and lower surface of the wing were localized with average localization error of less than 50.0 mm. Better results were obtained by setting the k value to less than 7, as the overall

localization error is reduced to less than 40.0 mm. Similarly, by further decreasing the k value to less than 4, the impact test points were localized with average localization error of less than 30.0 mm. Among the 10 sets of average localization results for 10 different k values, the lowest localization error of 27.9 mm was obtained using $k = 3$.

Considering the lowest maximum localization error value, k value of 2, all 20 impacts were localized with average localization error of 28.5 mm and maximum localization error of 71.2 mm. In comparison to the localization results obtained using OM2 algorithm, shown in Table 4.15, the results obtained using OM3 does not show good localization performance, mostly because it is not very effective in accurately localizing the impact on the region near the leading edge or on the edge section of the impact test region.

4.4.2.2 OM3: SD Threshold Based Impact Localization

Impact localization results of the 20 impact test points obtained using the OM3 with SD threshold is tabulated in Table 4.17. Use of the threshold method to filter out locations which are farther from the mean of the detected location shows improved localization results than directly using the detected locations to predict the impact location using OM3. Out of the ten cases of k values used for impact localization, the use of the first seven k values shows that using either of these k value can predict the impact location with localization error of less than 100.0 mm.

Furthermore, in comparison with the OM3 results, using k value of 10, the SD threshold lowers the largest maximum localization error at Impact Test Point 10, from 191.3 mm to 106.8 mm. Similarly, using k value of 8 and 9, the impact locations were detected with maximum error being slightly over 100.0 mm. Moreover, by increasing the k value from 1 to 3, the maximum localization error decreased from 87.0 mm to the lowest obtained localization error of 49.6 mm. Increasing the k value from 4 to 7 resulted in the rise in obtained maximum localization error from 53.6 mm to 78.3 mm.

Likewise, corresponding to the reduction in maximum localization error for varying k values, significant improvement in the overall localization performance using the SD threshold is observed in Table 4.17. The largest average localization value obtained using OM3 with $k = 9$ is lowered by approximately 20.0 mm; as a result, it is seen that using any of the k values between 1 and 10, the impact test points on the composite wing were predicted with average localization error of 33.0 mm or less. The average localization error decreases as the k value is increased from 1, and at $k = 3$ the impact test points were localized with lowest average localization error of 17.1 mm compared to the results obtained using other k values. Using k value from 4 to 8 results in prediction of the impact test points with average localization error from 18.2 mm to 27.9 mm.

Using the OM3 with SD threshold with $k = 3$, the 20 impact test points on the composite wing were localized with average localization error of 17.1 mm and maximum localization error of 49.6 mm; 0.2 mm less

error and 7.4 mm higher than the OM2 localization results, respectively. In conclusion, the results are found to be considerably similar to each other. Moreover, by incorporating the SD threshold with the OM3 algorithm, significant improvement in the impact localization performance was achieved. The lowest maximum localization error obtained using the OM3 with SD threshold is reduced by 21.6 mm and the average localization error by about 11.0 mm in comparison with the impact localization results obtained using OM3 with k value of 2.

Table 4.17 OM3 with SD threshold impact localization results.

Impact Test Point		OM3 with SD Threshold Localization Results for Varying k Value (mm)									
		10	9	8	7	6	5	4	3	2	1
Upper Surface	1	27.3	29.4	29.8	25.0	25.2	7.1	9.7	9.1	51.5	11.8
	2	19.2	16.2	4.6	2.2	17.1	1.0	4.5	4.4	9.8	71.1
	3	31.2	13.0	28.2	25.1	28.9	24.2	1.0	6.6	3.2	11.4
	4	20.0	20.2	17.9	20.2	14.9	5.2	7.7	5.9	3.0	11.8
	5	37.5	40.2	39.1	38.8	36.1	16.7	36.0	35.4	25.0	63.5
	6	0.9	3.7	1.1	22.1	22.1	1.7	2.3	6.8	26.4	11.8
	7	54.7	53.2	41.3	32.0	34.0	34.0	25.0	25.0	32.0	25.0
	8	27.6	30.1	25.3	19.1	18.5	2.8	8.3	8.3	26.4	26.4
	9	3.3	25.1	3.4	3.6	18.7	5.0	8.3	4.5	9.7	26.4
	10	106.8	105.0	85.5	73.4	73.1	73.0	53.6	49.6	35.4	87.0
Lower Surface	11	0.8	3.4	7.8	8.7	17.0	12.8	6.0	6.0	20.6	4.7
	12	29.8	21.0	23.5	24.2	20.2	47.0	33.4	10.3	26.4	23.0
	13	47.7	80.0	29.0	26.8	29.8	34.7	30.7	25.0	25.0	26.1
	14	41.8	21.0	24.0	27.5	25.0	17.2	4.3	8.6	25.0	25.4
	15	12.1	25.5	25.9	15.6	9.4	25.5	26.4	25.8	8.3	11.8
	16	1.9	2.9	21.6	6.1	18.2	8.4	17.7	25.1	25.0	26.1
	17	8.0	24.6	19.7	27.3	15.6	21.1	23.3	15.1	20.6	33.5
	18	32.5	32.8	17.0	35.4	54.6	52.6	24.0	35.4	79.7	49.0
	19	6.8	13.6	12.9	9.5	10.6	11.0	3.8	5.0	15.4	25.0
	20	100.2	99.9	101.3	78.3	56.6	57.2	38.6	29.3	31.9	21.0
Max. Error		106.8	105.0	101.3	78.3	73.1	73.0	53.6	49.6	79.7	87.0
Avg. Error		30.5	33.0	27.9	26.0	27.3	22.9	18.2	17.1	25.0	29.6

4.4.2.3 OM3: MAD Threshold Based Impact Localization

The MAD threshold based detected location selection criteria based impact localization results of the 20 impact test points are presented in Table 4.18. Using OM3 with MAD threshold also results in improvement in the obtained localization results in comparison with the OM3 results. When k is set to 10, the maximum localization error at Impact Test Point 10 is reduced from 191.3 mm to 106.8 mm. The maximum error value is limited to less than 100.0 mm with k value less than 5. The lowest maximum localization error of 43.3 mm is obtained using k = 2. Whereas for k = 1 and k = 4~10, the maximum localization errors are over 50.0 mm.

Table 4.18 OM3 with MAD threshold impact localization results.

Impact Test Point		OM3 with MAD Threshold Localization Results for Varying k Value (mm)									
		10	9	8	7	6	5	4	3	2	1
Upper Surface	1	37.9	38.5	31.5	26.4	27.4	19.0	9.7	16.2	37.3	11.8
	2	19.8	16.2	11.6	13.5	17.1	16.0	9.5	4.4	9.8	29.3
	3	30.4	23.5	25.1	25.4	25.9	24.8	10.1	15.5	3.2	11.4
	4	20.5	22.8	20.0	20.0	14.9	10.1	7.9	10.6	12.0	11.8
	5	25.7	29.8	27.8	25.7	21.6	16.7	15.0	20.1	25.0	63.5
	6	14.5	15.8	6.3	13.1	22.1	10.8	8.3	14.2	26.4	11.8
	7	60.1	53.2	49.9	60.6	57.4	31.9	34.4	25.0	26.4	25.0
	8	29.9	26.4	25.3	15.9	18.5	14.4	8.3	11.8	18.6	26.4
	9	18.0	14.4	8.8	6.9	18.7	11.8	8.3	12.8	18.6	26.4
	10	106.8	105.0	110.0	103.0	97.5	101.1	97.8	47.1	43.3	87.0
Lower Surface	11	9.3	7.2	7.3	8.7	17.0	12.8	8.2	4.7	12.7	4.7
	12	29.8	27.9	27.8	30.2	27.2	33.4	24.4	10.3	18.2	23.0
	13	71.9	78.6	68.5	63.7	63.1	37.3	34.1	26.8	25.0	26.1
	14	32.6	25.3	33.0	27.5	25.0	17.2	12.6	12.9	20.9	25.4
	15	26.5	25.9	23.3	18.1	9.4	19.8	23.4	14.0	8.3	11.8
	16	17.0	15.0	11.3	9.4	14.0	18.3	17.7	26.8	25.0	26.1
	17	5.4	15.1	11.6	13.5	15.6	15.2	15.5	15.7	20.6	33.5
	18	36.1	35.2	33.0	34.3	17.0	34.3	24.0	35.4	41.9	79.7
	19	19.3	17.0	12.9	18.3	25.1	11.0	10.0	5.1	7.5	25.0
	20	53.3	79.3	66.1	97.6	53.0	36.2	27.5	29.3	31.9	21.0
Max. Error		106.8	105.0	110.0	103.0	97.5	101.1	97.8	47.1	43.3	87.0
Avg. Error		33.2	33.6	30.6	31.6	29.4	24.6	20.4	17.9	21.6	29.0

Overall improvement in the localization performance is obtained using the OM3 with MAD threshold compared to the OM3 localization performance. Using any value of k from 1 to 10 results in average localization error below 35.0 mm. Using k value between 6 to 10 results in the prediction of the impact location with average localization error above 30.0 mm. By using lower k values, $k = 2\sim5$, the impact test points were localized with average localization error of less than 25.0 mm. In case of the OM3 with MAD threshold algorithm, the lowest average localization error is obtained when k is set to 3, resulting in average localization error of 17.9 mm.

Overall, these results are considerably similar to the results obtained using the OM2 algorithm. Therefore, the OM3 with MAD threshold based impact localization algorithm is found to be a good impact localization technique as well. Furthermore, the lowest maximum localization error obtained using the OM3 with MAD threshold is found to be less than the lowest maximum error obtained using OM3 with SD threshold by over 6.0 mm. Nevertheless, overall results obtained using the MAD threshold are similar to the results obtained using the SD threshold for varying k values.

4.4.2.4 OM3: Weighted MAD Threshold Based Impact Localization

The localization results of the 20 impact test points on the upper and lower surface localized using the OM3 with weighted MAD threshold are shown in Table 4.19 and the overall results are compared with the results obtained using the other OM3 methods in Figure 4.37. In comparison with the OM3 results, significant improvement in the localization results for varying k values are obtained using the weighted MAD threshold. Additionally, the localization results presented in Table 4.19, show better overall localization performance for varying range of k values than the results obtained using SD threshold and MAD threshold.

The improvement is evident since, out of ten k values used for the localization, all of the k values were successful in lowering the maximum localization error at Impact Test Point 10 to about 100.0 mm or less. Furthermore, using k values between 3 to 7 the maximum localization error of less than 60.0 mm was obtained, and the lowest maximum localization error of 41.5 mm was obtained using $k = 5$.

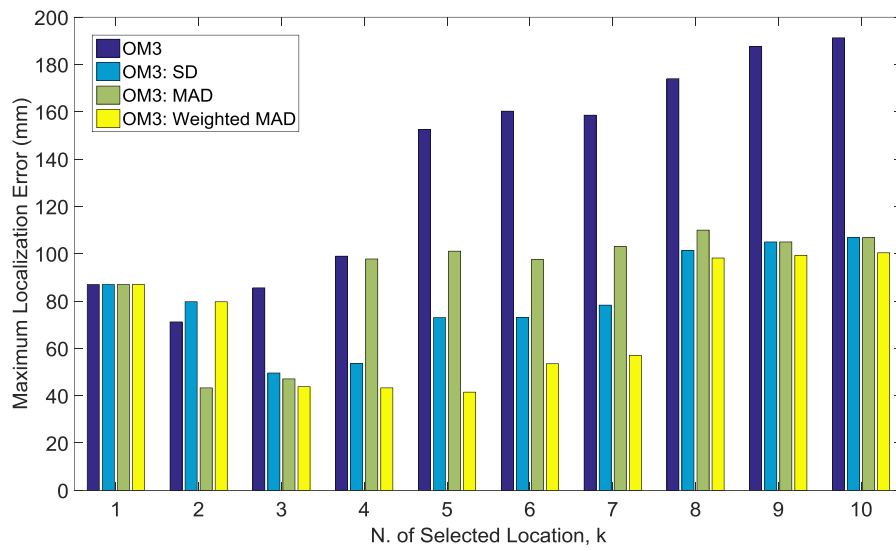
Similarly, the weighted MAD threshold results in better prediction of impact location for most of the impact test points. For varying k values, the impact locations were localized with average localization error of less than 29.0 mm. Overall, the average localization error for k value between 1 to 10 was found to be in the range of 23.0 mm. Furthermore, selecting k value from 3 to 6 enabled the impact test points to be localized with average localization error of 20.0 mm or less.

The lowest average localization error of 18.3 mm was obtained with $k = 4$, corresponding to maximum localization error of 43.3 mm. Whereas, the lowest maximum localization error of 41.5 mm was obtained using $k = 5$, corresponding to average localization error of 18.5 mm. Using OM3 with weighted MAD threshold, the

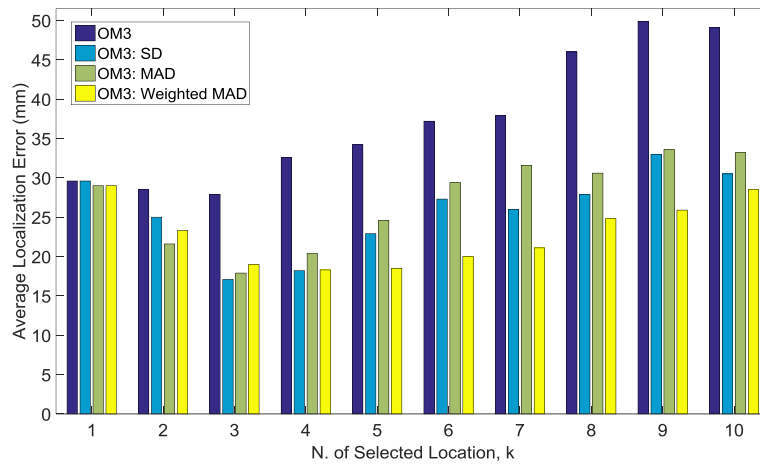
maximum localization error obtained by setting $k = 5$ results in more accurate results than using the other OM3 based impact localization algorithms and similar results were obtained compared to OM2 algorithm results. In summary, the OM3 with weight MAD threshold shows improved localization results for varying range of k values than the OM3 with SD and MAD threshold. Moreover, it is demonstrated that OM3 algorithm with various different threshold techniques to filter the detected locations results in effective localization performance, and it can give similar localization results compared to the OM2 based localization algorithm.

Table 4.19 OM3 with weighted MAD threshold based impact localization results.

Impact Test Point		OM3 with Weighted MAD Threshold Localization Results for Varying k value (mm)									
		10	9	8	7	6	5	4	3	2	1
Upper Surface	1	26.6	25.4	23.9	22.0	20.8	18.3	18.0	22.4	28.6	11.8
	2	13.0	10.7	8.5	7.4	5.8	4.4	9.0	7.7	14.8	29.3
	3	21.4	20.8	20.6	19.9	17.9	14.7	9.8	10.4	5.9	11.4
	4	15.6	14.4	13.0	12.3	10.6	9.1	9.2	10.6	10.6	11.8
	5	27.8	21.3	20.5	18.7	17.1	16.5	18.3	22.3	25.0	63.5
	6	19.2	18.4	17.3	16.7	15.2	12.6	13.4	16.9	21.2	11.8
	7	45.2	43.3	29.2	27.6	27.5	25.0	26.7	25.2	25.6	25.0
	8	19.5	18.0	15.2	12.9	11.6	10.4	12.8	14.6	21.2	26.4
	9	19.1	17.3	15.1	13.0	11.3	12.0	14.2	17.1	21.2	26.4
	10	100.4	99.3	98.2	57.0	53.5	41.5	43.3	43.8	40.7	87.0
Lower Surface	11	13.7	12.0	10.8	10.2	9.7	7.5	6.0	6.1	9.2	4.7
	12	26.8	26.3	25.9	25.5	24.1	27.1	18.1	14.0	17.9	23.0
	13	63.8	28.9	39.9	36.3	33.2	31.2	28.3	25.5	25.1	26.1
	14	20.3	20.2	20.0	19.2	17.1	14.6	14.6	17.0	21.8	25.4
	15	19.2	17.9	16.7	16.3	15.9	16.6	15.3	5.7	8.8	11.8
	16	15.2	20.2	19.4	18.8	18.5	19.4	20.7	24.4	25.1	26.1
	17	14.2	14.7	15.0	16.0	16.5	17.0	18.0	19.5	25.1	33.5
	18	34.5	34.1	33.9	32.4	34.2	33.9	34.1	39.9	79.7	79.7
	19	10.5	10.0	9.3	8.7	8.5	8.8	8.5	9.0	13.0	25.0
	20	44.9	44.8	43.6	32.0	31.3	30.1	27.5	27.5	26.2	21.0
Max. Error		100.4	99.3	98.2	57.0	53.5	41.5	43.3	43.8	79.7	87.0
Avg. Error		28.5	25.9	24.8	21.1	20.0	18.5	18.3	19.0	23.3	29.0



a) Maximum localization error comparison



b) Average localization error comparison

Figure 4.37 OM3 algorithms impact localization results comparison.

4.4.2.5 Results Comparison and Discussions

The error outlier based impact localization algorithms were validated by localizing the impact test points on composite wing of Jabiru UL-D aircraft. The optimal localization results for the complex wing test region obtained using OM2, OM3, OM3 with SD threshold, OM3 with MAD threshold and OM3 with weighted MAD threshold are summarized in Table 4.20. Using various OM algorithms presented in this dissertation, the impact test points were well localized. Considering the complexity of the structure, the results can be observed to be well localized using the error outlier based impact localization algorithms.

Table 4.20 OM localization results summary.

Impact Localization Results of Impact Test Points on Complex Wing Surface Region		
Algorithm	Average Error (mm)	Maximum Error (mm)
OM2	17.3	42.2
OM3	28.5	71.2
OM3: SD	17.1	49.6
OM3: MAD	21.6	43.3
OM3: Weighted MAD	18.5	41.5

Overall, the error outlier based impact localization algorithms with location selection thresholds, OM2, OM3 with SD threshold and OM3 with MAD threshold, shows similar localization performance. The impact test points were predicted with error of less than 50.0 mm. Nevertheless, algorithm without location filtering criteria, OM3, also show good localization performance as it localized the impact location with an average error of 28.5, but the maximum error of 71.2 mm occurred using this method. OM2 and OM3 algorithms shows similar localization results. Using OM2 the impact test points were localized with maximum error of 42.2 mm and average error of 17.3 mm. Similarly, using OM3 with weighted MAD threshold, most of the impact test points were localized within 18.5 mm from the actual impact location and the maximum localization error was 41.5 mm.

In addition to the good localization performance, the OM also shows less computation time required to process the signal from the FBG sensors to predict the location of the impact. The computation time was compared with the localization results obtained using cross-correlation method using three FBG sensors in Table 4.15; the OM algorithm settings presented in this dissertation was able to determine the impact location approximately 60% faster in comparison with the cross-correlation method [82].

4.4.3 Impact Localization Under Simulated Wing Loading Condition

4.4.3.1 Experimental Setup

The impact localization under simulated wing loading was performed on Jabiru UL-D aircraft's (Jabiru Aircraft Pty Ltd, Australia) composite wing, shown in Figure 3.7. The localization tests under the simulated wing loading conditions were performed by localizing the impact test points on the complex wing surface region, shown in Figure 4.28. The experimental set-up configuration of the wing and the sensors are the same as presented in 4.3.6. The impacts delivered to the wing surface were monitored using three FBG sensors, with center wavelength of 1544.6 nm, 1547.6 nm and 1550.6 nm and the signals from these sensors were sampled at 100 kHz using the high speed interrogator, SFI-710.

The FBG signals acquired from the 609 reference points were used to estimate the locations of 20 impact test points located within the test region. The impact test points coordinates are shown in Figure 4.30. The wing loading was simulated by using weights to bend the wing in the upward direction, as shown in Figure 4.38. A total mass of 104 kg was used to bend the wing upward, resulting in tip deflection of approximately 70 mm. The FBG response signal, acquired at 500 Hz frequency, as the weight was applied is presented in Figure 4.39. The impact localization under simulated wing loading condition was done using OM3 with weighted MAD threshold algorithm. The algorithm was run by setting the error threshold parameter to 1.5 nm and using $k = 5$.

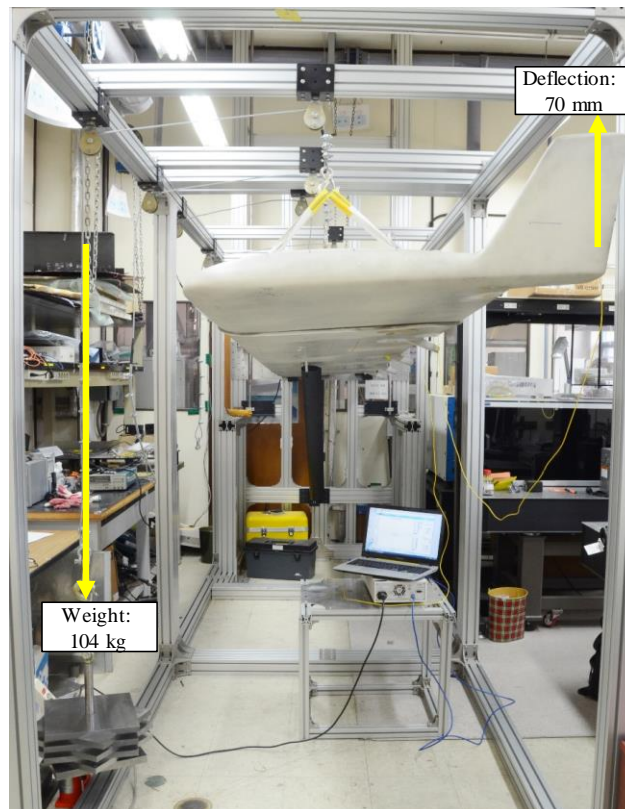


Figure 4.38 Experimental set-up.

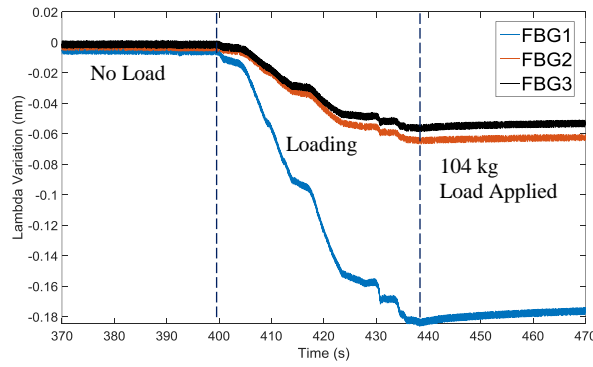


Figure 4.39 Lambda variation due to simulated wing loading.

4.4.3.2 Results and Discussion

The test points on the upper and lower surface of the composite wing under simulated wing loading conditions were localized using the OM3 with weighted MAD threshold impact localization algorithm. The localization results obtained using this algorithm are visualized as shown in Figure 4.40 and tabulated in Table 4.21. The 20 impact test points were well localized using the OM3 with weighted MAD threshold impact localization algorithm. The impact test points were localized with average localization error of 22.1 mm and Impact Test Point 10 located on the edge of the impact test region of the upper wing surface was localized with maximum error of 50.8 mm.

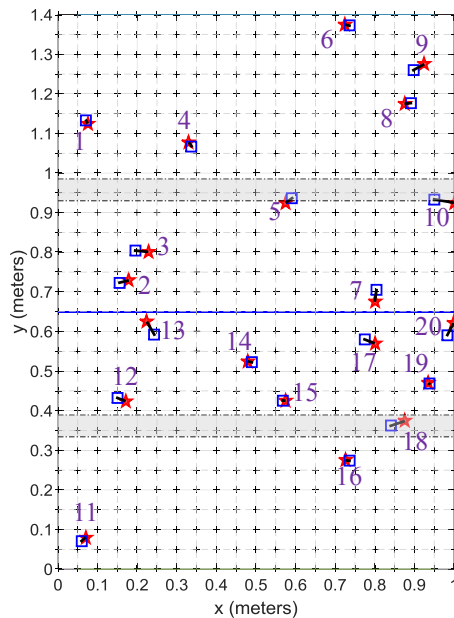


Figure 4.40 Visualization of impact localization under simulated wing loading condition.

Moreover, the localization results of impacts delivered on wing subjected to simulated wing loading were found to be similar to the localization results of impact delivered on wing structure without any simulated

wing loading condition using OM2 and OM3 with weighted MAD threshold algorithms presented in the earlier section. Even for the impact localization done on composite wing without simulated loading condition, the same Impact Test Point 10 was the impact case which was localized with maximum error of 42.2 mm and 41.5 mm using the OM2 and OM3 with weighted MAD threshold algorithms, respectively.

Table 4.21 Impact localization under simulated wing loading.

Upper Surface		Lower Surface	
Impact Test Point	Localization Error (mm)	Impact Test Point	Localization Error (mm)
1	8.1	11	13.7
2	24.3	12	22.6
3	33.1	13	37.9
4	12.5	14	10.8
5	19.9	15	7.5
6	11.4	16	10.2
7	29.8	17	27.7
8	16.0	18	37.7
9	31.2	19	3.3
10	50.8	20	33.7
Maximum Error	50.8		
Average Error	22.1		

The reason for larger error at Impact Test Point 10 compared to other impact location was discussed in detail in Section 4.3.7. In brief, the impact delivered at Impact Test Point 10 was localized with larger error due to the fact that this test point lies at the edge of the impact test region, as a result the training points only exist on the left-side of the impact test point. Additionally, OM3 with weighted MAD threshold algorithm, which was set to select five possible impact locations for final impact location prediction, selects five possible impact locations only on the left-side of the actual Impact Test Point 10 resulting in larger localization error for impacts located at the edge of the impact test region.

Nevertheless, using the OM3 with weighted MAD threshold algorithm, all of the impacts delivered under simulated loading condition were localized with similar average localization error compared to OM2 and OM3 with weighted MAD threshold algorithm which were used to localize impacts on the wing without any simulated wing loading condition; 22.1 mm, 17.3 mm and 18.5 mm respectively. Therefore, from the present study it can be concluded that the OM can effectively localize impacts under simulated wing loading condition as well.

4.5 Single Sensor Impact Localization Parametric Study

The parametric study to demonstrate the feasibility of localizing impact using the OM2 and OM3 with weighted MAD threshold based impact localization algorithms using impact signals from a single FBG sensor were performed. The parametric study was done on the upper and lower surface test region of 1000 mm \times 1400 mm, monitored using 3 FBG sensors presented in Section 4.3.6. The 20 impact test points presented in Section 4.3.6 and visualized in Figure 4.30 were used for the single sensor parametric study. Subsequently, in Section 4.5.3, the present single sensor parametric study results were compared with the impact localization done using cross-correlation based impact localization algorithm [82].

4.5.1 OM2: Single Sensor Parametric Study

Impact localization performance using one FBG sensor covering the upper and lower surface of the composite wing, illustrated in Figure 4.28, was examined using the OM2 impact localization algorithm. Firstly, OM2 algorithm with same parameters used in Section 4.3.6 were selected for the parametric study, i.e., the error threshold value of 1.5 nm, NAO = 100 and $k = 4$ were used. The impact localization results obtained using the individual FBG sensor are tabulated in Table 4.22 and the predicted location by each sensor is visualized in Figure 4.41. Using individual FBG sensors, impact locations are found to be predicted close to the actual impact location for most of the impact point cases. Better localization results were obtained for the upper wing surface than the lower wing surface; on the upper surface the average localization error of 29.9 mm, 13.8 mm and 61.5 mm were obtained using FBG1, FBG2, FBG3, whereas, on the lower surface of the wing the impact test points were localized with average localization error of 31.5 mm, 48.3 mm and 45.9 mm, with FBG1, FBG2 and FBG3, respectively. Considering both of the wing surfaces, the use of FBG1, FBG2 and FBG3 for impact localization resulted in average localization error of 30.7 mm, 31.1 mm and 53.7 mm, respectively.

Overall, use of either of the FBG1 and FBG2 shows similar localization performance, while more number of impact test points were localized with larger localization error using FBG3. The maximum localization error using FBG1 occurred at Impact Test Point 5, 142.2 mm, and error larger than 50.0 mm occurred at three impact test points, at Impact Test Point 10, 18 and 19, 55.9 mm, 50.6 mm and 54.6 mm, respectively. FBG2 shows good localization performance on the upper surface of the wing; with all impact test points predicted with error of less than 30.0 mm. Whereas, on the lower surface, using FBG1, the maximum error of 179.4 mm error occurs at Impact Test Point 20, and localization error of 58.7 mm and 56.4 mm occurs at Impact Test Point 16 and 18, respectively. FBG3 localization results shows larger localization error value at several impact test points. Compared with the other two sensors, the largest maximum error of 246.9 mm occurred using FBG3 at Impact Test Point 2. Furthermore, error of over 100.0 mm occurred for three other impact test points; at Impact Test Point 10, 13, and 17.

Table 4.22 Single FBG sensor parametric study based impact localization results using OM2 algorithm.

Impact Localization Error (mm)				
	Impact Test Point	FBG1	FBG2	FBG3
Upper Surface	1	15.0	0.0	15.0
	2	29.3	21.4	246.9
	3	5.4	3.2	22.0
	4	5.8	5.8	25.3
	5	142.2	0.0	28.0
	6	0.0	0.0	25.0
	7	45.1	25.0	25.0
	8	0.0	25.0	0.0
	9	0.0	28.0	28.0
	10	55.9	30.0	200.2
Maximum Error		142.2	30.0	246.9
Average Error		29.9	13.8	61.5
Lower Surface	11	15.3	21.4	7.1
	12	25.0	10.3	25.0
	13	34.7	44.5	102.1
	14	22.6	24.4	4.0
	15	28.0	28.0	26.4
	16	34.7	58.7	1.0
	17	50.6	37.6	200.8
	18	54.6	56.4	24.0
	19	17.6	22.4	15.8
	20	31.9	179.4	53.3
Maximum Error		54.6	179.4	200.8
Average Error		31.5	48.3	45.9
Maximum Error		142.2	179.4	246.9
Average Error		30.7	31.1	53.7

As observed in the previous section, most of the large error, over 100.0 mm, occurs at impact point which are located near by the leading edge of the wing. Similarly, the predicted error also increases when the impact point is located at the edge of the impact test region. However, from the parametric study results it can be concluded that using several sensors can significantly improve the localization results since more data are

available for more accurate impact location prediction. Nonetheless, the OM algorithm to predict the impact location is found to be robust in detecting most of the impact locations using just one FBG sensor. The results presented in Table 4.22 were obtained using OM2 with error threshold of 1.5 nm. By setting error threshold value to 1.5 nm and using one FBG sensor for impact signal acquisition and data processing, the OM2 algorithm took only 4.5 s to predict an impact location. The localization speed was reduced by over 50% compared with the time it took to compute an impact point using OM2 with six FBG sensors.

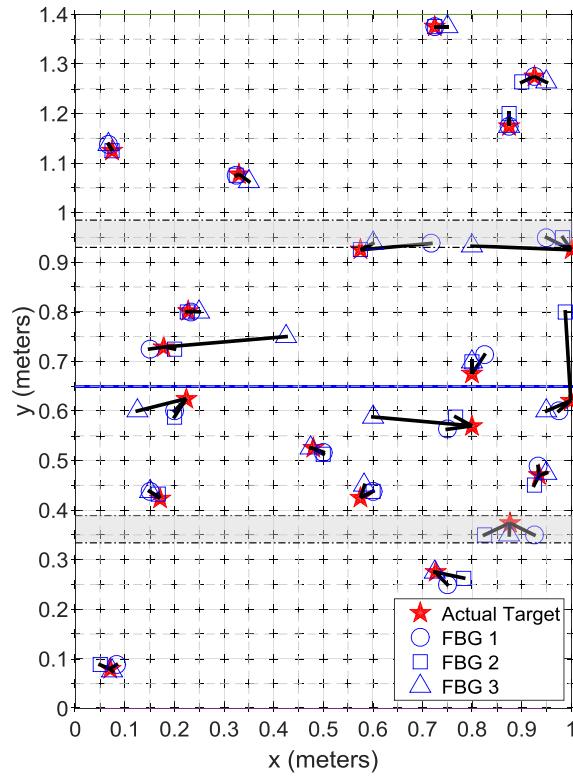


Figure 4.41 Visualization of single FBG sensor parametric study based predicted impact locations.

In Table 4.7, it is shown that reducing the error threshold can result in improved localization result. Therefore, for improved results, the error threshold value was reduced to 1.0 nm, while same NAO of 100 and allowed number of detected location, $k = 4$, were used in the OM2 impact localization algorithm. The impact localization results obtained using the individual FBG sensor are tabulated in Table 4.23 and the predicted impact locations are visualized in Figure 4.42. The parametric study results of impact localization done using one FBG sensor are tabulated in Table 4.23. Better localization performance was obtained with error threshold value of 1.0 nm when using one FBG sensor to predict the location of the impact on the upper and lower surface of the composite wing. Overall, the average localization error for each of the FBG sensor was decreased; using FBG1, FBG2 and FBG3, in case of the impacts on the upper surface were localized with average localization

error of 22.1 mm, 25.0 mm and 36.0 mm, respectively, and impact test points on the lower surface were localized with average error of 26.5 mm, 27.6 mm and 22.5 mm, respectively.

Table 4.23 OM2 impact localization parametric study using error threshold value of 1.0 nm.

Impact Localization Error (mm)				
	Impact Test Point	FBG1	FBG2	FBG3
Upper Surface	1	25.0	15.0	11.8
	2	5.7	21.4	22.7
	3	3.2	28.0	22.0
	4	5.8	11.8	25.3
	5	100.0	25.0	28.0
	6	0.0	0.0	25.0
	7	25.0	25.0	25.0
	8	0.0	25.0	0.0
	9	0.0	42.5	0.0
	10	55.9	55.9	200.4
	Maximum Error	100.0	55.9	200.4
	Average Error	22.1	25.0	36.0
Lower Surface	11	20.6	4.7	7.1
	12	10.3	33.4	21.0
	13	38.6	25.0	70.0
	14	32.6	25.3	4.0
	15	11.8	15.0	11.8
	16	34.7	34.7	11.1
	17	7.5	13.3	7.5
	18	74.9	56.4	35.4
	19	13.4	35.8	25.0
	20	21.0	31.9	31.9
	Maximum Error	74.9	56.4	70.0
	Average Error	26.5	27.6	22.5
Maximum Error		100.0	56.4	200.4
Average Error		24.3	26.3	29.3

Compared with the results obtained using error threshold value of 1.5 nm, the localization performed using error threshold value of 1.0 nm shows improved localization results in terms of the maximum localization error values obtained when using a single sensor to predict the impact location. The maximum localization error for each of the sensor, FBG1, FBG2 and FBG3, were decreased to 100.0 mm, 56.4 mm and 200.4 mm, respectively. The number of localization error larger than 100.0 mm are reduced from 6 to 2. The maximum error occurred at Impact Test Point 5 for FBG1, at Impact Test Point 18 for FBG2 and at Impact Test Point 10 using FBG3. Occurrence of localization error of over 50.0 mm for all three FBG sensors occurred only at Impact Test Point 10. Whereas, for the other impact cases most of these points were localized with error of less than 50.0 mm by all of the FBG sensors. For some impact test points, such as Impact Test Point 5, only one of the FBG sensor resulted in large localization error.

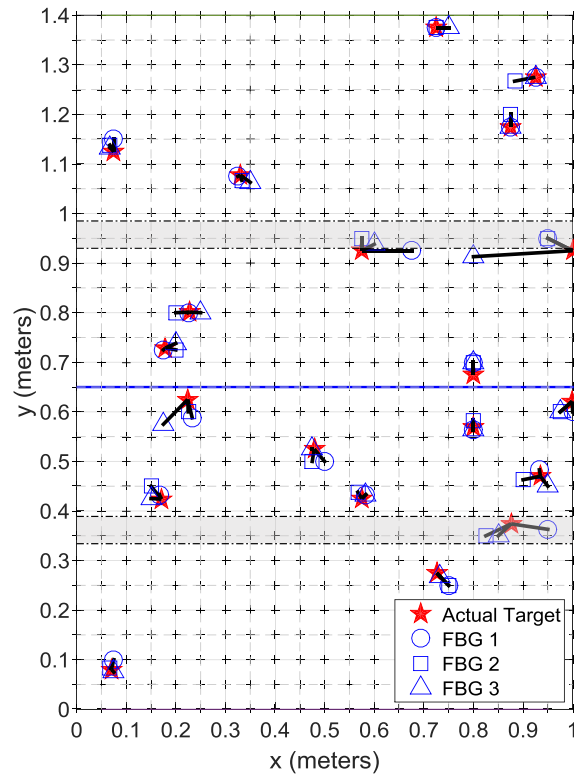


Figure 4.42 OM2: single sensor based predicted impact location visualization.

Moreover, it can be seen that using a single FBG sensor, FBG2, all of the 20 impact test points on the upper and lower surface of the wing were localized with maximum localization error of 56.4 mm and average localization error of 26.3 mm. The obtained results further demonstrate the effectiveness of the OM to successfully localize the impact test points on complex composite structures.

4.5.2 OM3 with Weighted MAD Threshold Algorithm: Single Sensor Parametric Study

As in the previous section, the single sensor parametric study using OM3 with weighted MAD threshold algorithm were performed for error threshold limit of 1.5 nm and 1.0 nm. The single sensor impact localization results obtained using error threshold limit of 1.5 nm and 1.0 nm are tabulated in Table 4.24 and Table 4.25 and the predicted impact locations are visualized in Figure 4.43 and Figure 4.44, respectively.

Overall, the localization results obtained using OM3 with weighted MAD threshold algorithm are found to be similar to the results obtained using OM2 algorithms. Additionally, similar impact test points which were localized with larger location using OM2 algorithm, were localized with large localization error using OM3 with weighted MAD threshold algorithm as well; such as Impact Test Point 2, 10, 13, 17. These locations with large error are located close to the leading edge or close to the spar region. However, it can be observed that using OM3 with weighted MAD threshold algorithm overall better results, as shown in Table 4.24 and Figure 4.43, were obtained compared with OM2 algorithm when the error outlier threshold was set to 1.5 nm. For instance, for FBG1 and FBG2 the maximum localization error obtained using the OM3 with weighted MAD threshold algorithm decreased by 61.8 mm and 93.2 mm. As a result, using the OM3 with weighed MAD threshold with 1.5 nm error threshold value, the impact test points were localized with average error of 23.4 mm, 24.5 mm and 47.0 mm using the FBG1, FBG2 and FBG3 sensor.

As in the case of the OM2 based localization results, setting error threshold value to 1.0 nm in OM3 with weighted MAD threshold algorithm improved localization results compared to the results obtained using error threshold value of 1.5 nm, as shown in Table 4.25 and Figure 4.44. Furthermore, it can be observed that by decreasing the error threshold parameter improves the localization results for most of the impact test points except for the impacts located at the edge of the impact test region; such as Impact Test Point 10 and 20. Overall, using FBG1, FBG2 and FBG3, the 20 impact test points were localized with average error of 23.8 mm, 23.9 mm and 33.2 mm, and maximum localization error of 78.5 mm, 78.8 mm and 197.3 mm. Using either FBG1 or FBG2 sensors resulted in similar localization performance for the localization of the 20 impact cases visualized in Figure 4.30. Whereas, using FBG1 and FBG2, the OM2 algorithm localized the impact test points with average error of 24.3 mm and 26.3 mm and maximum error of 100.0 mm and 56.4 mm.

Although using FBG2 in case of OM2 algorithm shows optimal localization performance since the maximum error is limited to 56.4 mm, it can be seen that the overall localization performance of OM3 with weighted MAD threshold algorithm is slightly better than OM2 case. Moreover, both of these error outlier assessment approach for impact localization demonstrates the feasibility of predicting low velocity impact location on complex composite structures using just a single FBG sensor. The single sensor parametric study results obtained using the OM based impact localization algorithms are compared with cross-correlation based impact localization results in the subsequent section.

Table 4.24 OM3 with weighted MAD threshold: parametric study using error threshold value of 1.5 nm.

Impact Localization Error (mm)				
	Impact Test Point	FBG1	FBG2	FBG3
Upper Surface	1	3.9	3.9	24.6
	2	16.1	16.1	276.8
	3	19.3	19.3	17.9
	4	4.7	4.7	27.6
	5	9.1	9.1	23.7
	6	8.5	8.5	29.5
	7	26.2	26.2	26.9
	8	27.7	27.7	7.1
	9	33.7	33.7	26.4
	10	41.5	41.5	163.5
Maximum Error		41.5	41.5	276.8
Average Error		19.1	19.1	62.4
Lower Surface	11	17.7	22.4	12.0
	12	24.5	25.2	21.2
	13	32.5	37.4	54.9
	14	24.9	18.2	6.6
	15	19.7	14.3	16.4
	16	20.5	30.2	8.7
	17	12.0	16.7	111.8
	18	34.9	86.2	35.4
	19	10.0	22.7	15.1
	20	80.4	26.2	34.9
Maximum Error		80.4	86.2	111.8
Average Error		27.7	29.9	31.7
Maximum Error		80.4	86.2	276.8
Average Error		23.4	24.5	47.0

Table 4.25 OM3 with weighted MAD threshold: parametric study using error threshold value of 1.0 nm.

Impact Localization Error (mm)				
	Impact Test Point	FBG1	FBG2	FBG3
Upper Surface	1	11.8	11.8	14.3
	2	12.4	18.6	25.5
	3	34.5	16.7	18.3
	4	5.3	4.7	27.6
	5	78.5	14.1	21.2
	6	12.7	7.1	18.4
	7	31.9	25.3	25.0
	8	5.3	27.7	7.1
	9	9.7	33.7	8.5
	10	46.7	24.4	197.3
Maximum Error		78.5	33.7	197.3
Average Error		24.9	18.4	36.3
Lower Surface	11	17.7	20.3	13.7
	12	21.7	21.2	24.9
	13	40.5	27.2	57.5
	14	15.2	20.4	9.2
	15	20.2	19.0	16.5
	16	9.2	31.9	10.8
	17	12.0	17.0	6.7
	18	43.0	78.8	41.9
	19	10.0	33.2	1.7
	20	37.0	25.5	117.6
Maximum Error		43.0	78.8	117.6
Average Error		22.7	29.4	30.0
Maximum Error		78.5	78.8	197.3
Average Error		23.8	23.9	33.2

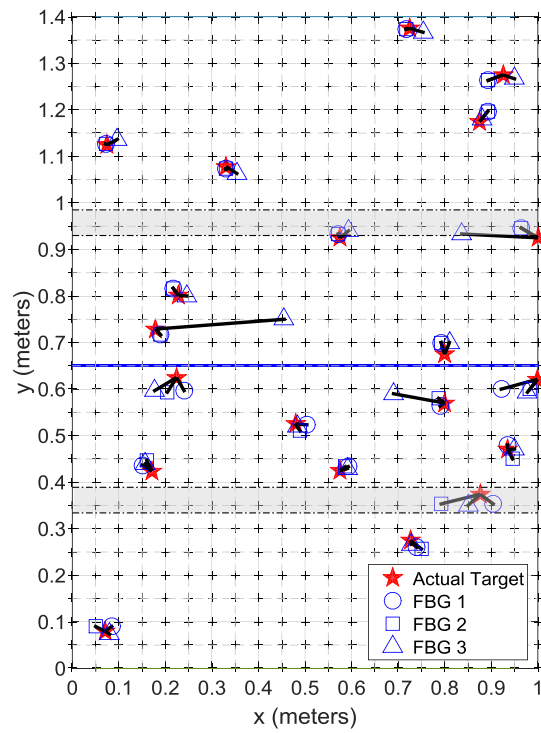


Figure 4.43 OM3 with weighted MAD threshold: single sensor based predicted impact location visualization using error threshold value of 1.5 nm.

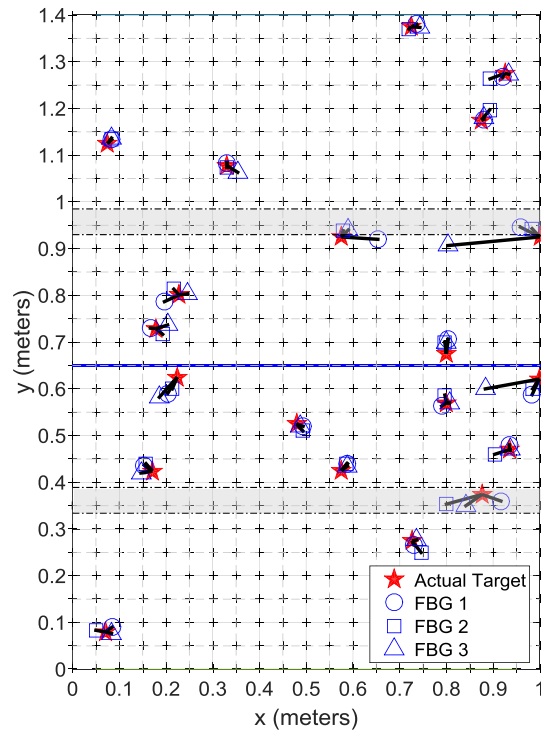


Figure 4.44 OM3 with weighted MAD threshold: single sensor based predicted impact location visualization using error threshold value of 1.0 nm.

4.5.3 Results Comparison and Discussions

From the single sensor parametric study, it can be concluded that the error outlier based impact localization algorithm is capable of determining the location of the impact on complex composite structure using a single FBG sensor. Moreover, using a single FBG sensor, and OM2 and OM3 with weighted MAD threshold algorithms, most of the low velocity impacts on the wing surface were localized about 27.0 mm from the actual impact location. The overall impact localization results obtained using all of the sensors are summarized and compared with single sensor localization results obtained using cross correlation method in Table 4.26. Overall, for a single sensor impact monitoring system, error outlier based impact localization algorithm shows more stable impact localization performance; both the OM algorithms predicted the impact locations with average error of about 27.0 mm. Whereas, for the cross-correlation method the impacts were localized with average error of about 77.7 mm.

Furthermore, significant difference in the computation time is found between these two methods, as shown in Table 4.26. Error outlier based impact localization algorithm is found to be more than 50% faster than the cross-correlation method; location of on an impact point was predicted by error outlier based impact localization algorithms in about 6.0 s, whereas it took cross-correlation algorithm about 13.4 s. The faster computation time can be attributed to several reasons such as the data length used for signal processing, algorithm efficiency, signal time-shift parameter, error threshold parameter. The result shown in Table 4.26 further demonstrates the OM algorithms effective performance capability to localize impact on complex composite structures.

Table 4.26 Single sensor based OM vs. cross-correlation localization results comparison.

	OM2 (3 Sensors)	OM3: Weighted MAD Threshold (3 Sensors)	Cross-correlation Method [82] (5 Sensors)
Maximum Error (mm)	200.4	197.3	627.0
Average Error (mm)	26.6	27.0	77.7
Computation Time (s)	5.7	6.0	13.4

4.6 Summary

In this chapter, a novel error outlier based impact localization algorithm was proposed and the novel impact localization method was successfully demonstrated for localization of low velocity impact on composite wing structure. Furthermore, error outlier based impact localization algorithms with several different techniques to determine the selection of possible impact location was also introduced; low velocity impact localization performance using OM algorithm with user set distance threshold, OM2 with Euclidean distance threshold, and OM with statistically determined distance threshold algorithms, OM3 with SD threshold method, OM3 with MAD threshold method, OM3 with weighted MAD threshold method were investigated.

Overall, the error outlier assessment based impact localization techniques were found to be effective tool for localizing impacts on composite wing structure. Moreover, OM2 and OM3 with weighted MAD threshold algorithms localized impact on complex composite wing structure with similar localization performance; average error of about 18.0 mm and maximum error of about 42.0 mm. Additionally, impacts delivered on composite wing under simulated wing loading condition were also localized with similar localization performance; average error of about 22.1 mm and maximum error of about 50.8 mm. Single sensor parametric study was done to determine if error outlier based impact localization algorithm can localize impacts on complex composite structure using a single sensor with similar localization performance compared to multiple number of sensors. The present study demonstrates the capability of the error outlier based impact localization algorithm to localize impact on complex composite structure using a single sensor; the impacts were localized with average error of about 27.0 mm within about 6.0 s. Additionally, from the present research the spar region and the edge of the impact test region were identified as weak spots, i.e. the impact located at the edge of the test region is vulnerable to larger localization error.

The localization performance of the error outlier based impact localization algorithm was compared with the experimental studies performed by various researchers in Table 4.27. Overall it can be seen that, using multiple number of sensors for monitoring impacts, the average and maximum localization results obtained for the various structures are found to range from 8.4 mm to 64.4 mm and 20.0 mm to over 100.0 mm, respectively. Moreover, it can be seen that the ratio calculated between the average error circular area and the test region area for most of the studies are about 3% or less. Similarly, for the present study this ratio is about 0.1 % using three FBG sensors and 0.2 % using a single FBG sensor. The localization performance depends on the impact test region/structure, types of sensor, number of sensors used for the localization and also the localization technique. Nonetheless, the results obtained using error outlier based impact localization algorithm together with either three FBG sensors or one FBG sensor are found to be satisfactory and reasonable in comparison to various other experimental results presented in Table 4.27.

Table 4.27 Impact localization on complex composite structure results comparison.

Reference	Localization Method	Dimension (mm × mm)	Sensor Type	N. of Sensors	Max. Error (mm)	Avg. Error (mm)	Area Normalized Avg. Error (%)
*Present Study: Wing Box	Reference Database	1000 × 1400	FBG	1	197.3	27.0	0.2
				3	41.5	18.5	0.1
[69] Wing Box	Reference Database	600 × 1200	FBG	6	35.4	18.8	0.2
[82] Wing Box	Reference Database	1000 × 1400	FBG	1	627.0	77.7	1.4
[68] Wing Box	Arrival Time Difference	500 × 500	FBG	6	65.9	45.4	2.6
[68] Stiffened Panel	Arrival Time Difference	500 × 600	FBG	4	82.6	51.7	2.8
[81] Stiffened Panel	Reference Database	600 × 900	FBG	4	33.8	17.7	0.2
[73] Wing Box	Time Reversal	385 × 400	PZT	6	25.4	8.4	0.1
[62] Stiffened Panel	Time Reversal	30 × 100	PZT	1	20.0	20.0	41.9
[72] Wing Flap	Reference Database	385 × 1015	PZT	9	>100.0	64.4	3.3
[63] Wing Box	Time Reversal Focusing	410 × 450	PZT	24	32.0	17.5	0.5
[74] Oil Tank	Near-field Multiple Signal Classification	310 × 610	PZT	7	21.0	13.2	0.3

Chapter 5. Soft and Hard-Impact Classification and Localization

5.1 Introduction

Low velocity impacts delivered using impact hammer with hard tip were well localized using the error outlier based impact localization algorithm. Impact localization algorithm capable of localizing impact delivered using impactor with varying hardness is highly desirable. Therefore, localization of impact delivered using impactor with varying hardness were investigated and presented in this chapter.

Impact delivered using hard material results in a short duration impact, whereas using soft material results in a long duration impact [105]. Comparison of FBG1 signals, from the same impact location coordinates (0.525 m, 0.825 m) on the upper surface of the composite wing shown in Figure 4.28, obtained using an impact hammer with hard tip and soft tip is presented in Figure 5.1. The impact signals for these two cases are found to differ significantly due to the changes in the hardness of the impact material. Additionally, the arrival time of the soft-body impact can be observed to be earlier than the hard-body impact case, as shown in Figure 5.1 (b). Additionally, periodograms of the soft and hard-impact signals are shown in Figure 5.2. In general, it can be seen that the power of the frequency, ranging from 0 Hz to 5000 Hz, for soft-impact is less than that for the hard-impact case except for the frequency range less than 300 Hz.

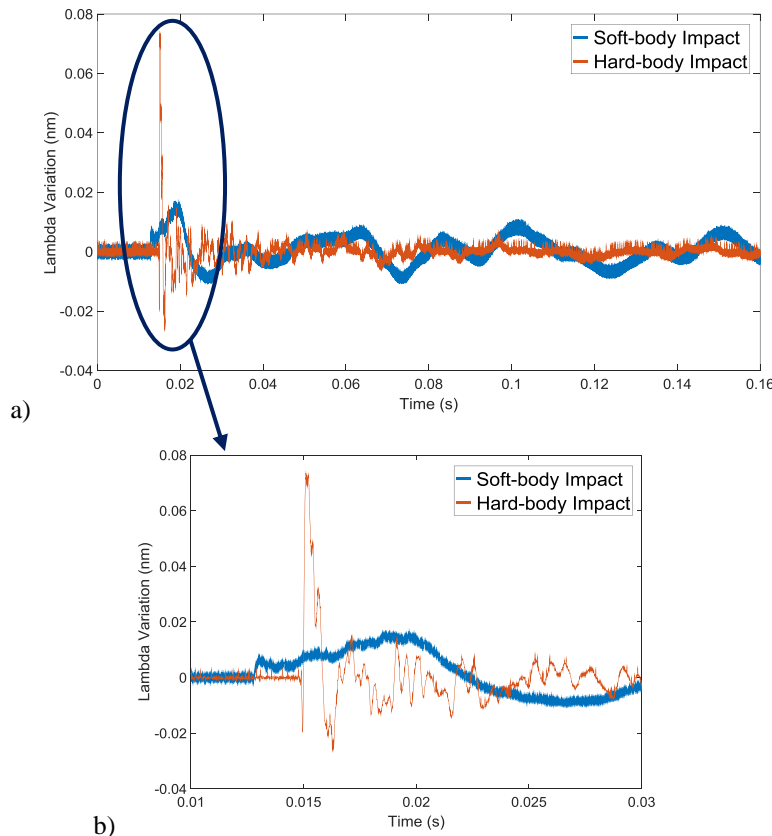


Figure 5.1 Hard-body and soft-body impact signal comparison.

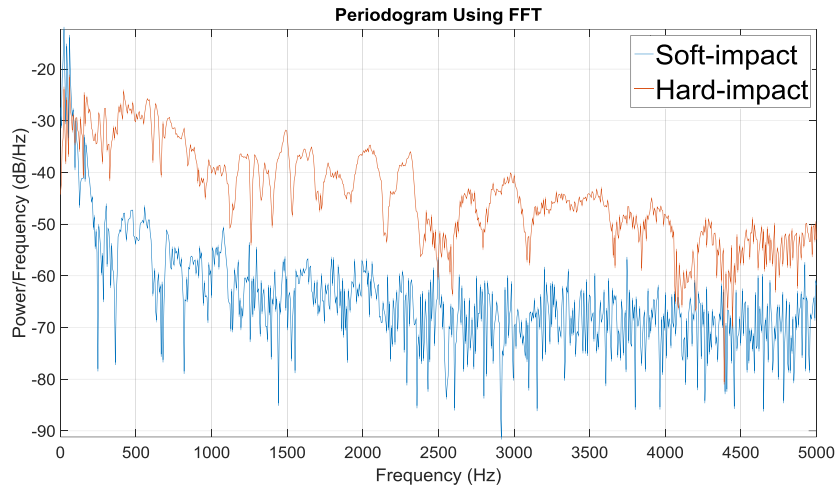


Figure 5.2 Soft and hard-impact periodogram plot.

Since the SFI-710 interrogator records the impact data once the amplitude of the signal is detected to be more than 0.01 nm, the significant difference in arrival time can be attributed to the slower amplitude increase rate for soft-body impact case compared to the hard-body impact case. As a result, using the same reference signals obtained using impact hammer with hard tip to localize impact with soft tip will result in highly inaccurate impact location prediction.

Therefore, the feasibility of localizing soft-body impact using the error outlier based impact localization algorithm is investigated in the subsequent sections by obtaining new set of reference signal database consisting of soft-body impact signals from each of the reference points on the impact test region. Furthermore, soft and hard-impact classification technique was developed and incorporated in the weighted MAD threshold algorithm. Finally, several impacts were delivered on the wing surface using hammers with varying impactor hardness, and the OM with weighted MAD threshold was used to classify the type of impact and predict the impact location.

5.2 Soft-Body Impact Localization

The soft-body impact localization was performed on Jabiru UL-D aircraft's (Jabiru Aircraft Pty Ltd, Australia) composite wing shown in Figure 4.28. The reference signals for the soft-impact localization study were obtained from the 609 reference points using the soft-impact hammer, with 24.0 mm × 25.0 mm contact tip, shown in Figure 5.3. OM3 with Weighted MAD threshold algorithm introduced in Section 4.4 was used to localize 40 soft-impact test points on the upper and lower surface of the composite wing illustrated in Figure 5.4.

In case of the hard-impact case, short impact data length has been found to be sufficient for accurate impact location prediction. Therefore, firstly in Section 5.2.1, the feasibility of soft-body impact localization was done for the first 10 impact cases shown in Figure 5.4 for varying data lengths from 0.030 s to 0.14 s. Subsequently in Section 5.2.2, the remaining impact test points were localized and compared for several data length cases.



Figure 5.3 Impact hammer with soft rubber used for reference database construction.

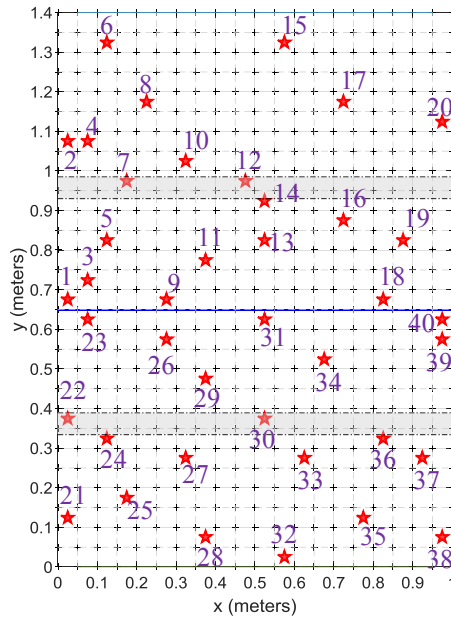


Figure 5.4 Soft-body impact test points visualization.

5.2.1 Data Length Parametric Study

Impact Test Point 1 to 10 were localized using response signal with data length varying from 0.03 s to 0.14 s and the results are tabulated in Table 5.1. Overall better localization results were obtained using longer data length. By increasing the data length used by the algorithm from 0.03 s to 0.14 s, the average localization error decreased from 103.0 mm to 53.1 mm, and the maximum error from 415.3 mm to 91.0 mm. Moreover, in contrast to the hard-impact localization results the soft-body impact were predicted with larger localization error.

The improved localization results obtained using longer data length can be understood by observing the impact response signal for the soft-body presented in Figure 5.1; the changes in the Lambda variation is relatively gradual and extends over a longer duration compared to the hard-impact case. Therefore, increasing the data length leads to improved localization performance, however it also increases the computation time from

36.9 s to 165.0 s. In the subsequent section, further localization test of all of the 40 impact test points are done for three data length cases: 0.040 s, 0.12 s and 0.14 s.

Table 5.1 Soft-body impact localization performance for varying response signal data length.

Data Length (s)	Average Error (mm)	Maximum Error (mm)	Computation Time (s)
0.030	103.0	415.3	36.9
0.035	77.9	137.5	43.4
0.040	64.2	125.0	49.4
0.060	71.2	164.2	75.7
0.080	65.5	137.6	103.7
0.100	68.7	165.0	124.8
0.120	58.7	106.9	148.7
0.140	52.1	91.0	165.0

5.2.2 Localization Performance Comparison

OM3 with weighted MAD threshold based error outlier algorithm was used to localize all of the 40 impact test points shown in Figure 5.4 using data length of 0.04 s, 0.12 s and 0.14 s. The predicted locations for each of the data length cases are visualized in Figure 5.5 and the localization results are tabulated in Table 5.2. In summary, using 0.04 s, 0.12 s and 0.14 s data length the impact test points were localized with average error of 58.6 mm, 50.6 mm, and 48.5 mm, respectively.

The impact location for which the localization error was maximum for each data length case was found to be close to the leading edge. For instance, using 0.04 s data length, the Impact Test Point 39 was localized with maximum error of 142.4 mm. In case of longer data length, 0.12 s and 0.14 s, the impact point located close to the spar region, Impact Test Point 36, was localized with maximum error of 114.5 mm and 111.0 mm, respectively. Even though the accuracy of the soft-body impact cases was not as accurate as for the hard-body impact cases presented in the earlier chapter, overall, it can be concluded that the error outlier approach can effectively localize the soft-body impacts using reference database constructed using soft-body impactor.

As evident from the data length parametric study presented in the previous section, using longer data length, i.e., 0.12 s or 0.14 s results in better localization results compared to 0.04 s data length. Moreover, increasing the data length from 0.12 s to 0.14 s, the localization results is found to be similar whereas the computation time increases considerably, as shown in Table 5.1. Therefore, further impact localization study of soft-impact was done using data length of 0.12 s.

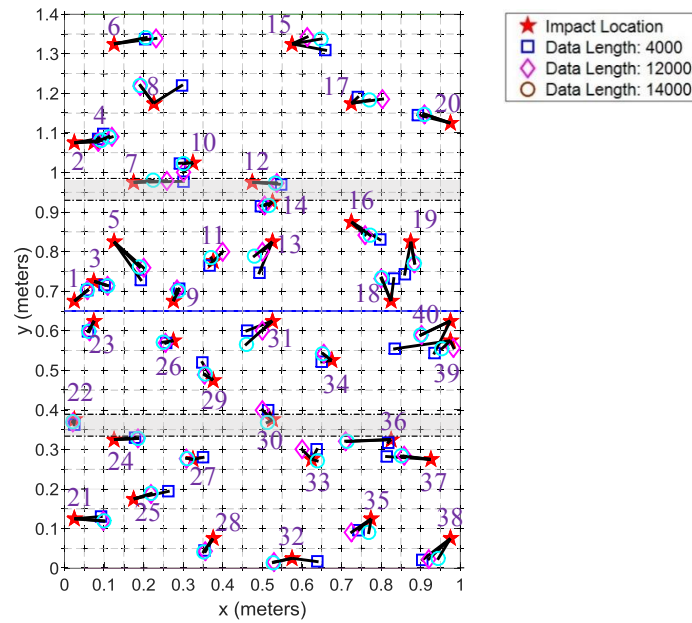


Figure 5.5 Visualization of predicted impact locations.

Table 5.2 Summary of soft-impact localization results.

Data Length (s)	0.04	0.12	0.14
Maximum Error (mm)	142.4	114.5	111.0
Average Error (mm)	58.6	50.6	48.5
SD (mm)	34.9	27.4	25.3

5.3 Localization of Impact Delivered with Varying Impactor Hardness

5.3.1 Overview

The response signal dissimilarity between the soft and hard-impact can be distinctly observed in Figure 5.1. Classification of the impact can be done by identifying the distinct features which differentiate the soft-impact from the hard-impact signals. The $Length_s$, distance between Ind_1 and Ind_2 of soft-body impact signal, is found to be significantly longer than $Length_h$, distance between Ind_1 and Ind_2 of hard-body impact signal, as illustrated in Figure 5.6. Therefore, in the algorithm presented in Figure 5.6, for the training signal selection, extraction of the distance feature between two time index, Ind_1 and Ind_2 , located closest to the maximum normalized lambda variation value of the impact signal was proposed for impact type classification.

The number of data points between Ind_1 and Ind_2 were determined for 10 different soft and hard-impact cases, selected from Figure 5.5 and Figure 4.30, and the results are tabulated in Table 5.3 (a) and (b). As expected, overall data length between Ind_1 and Ind_2 is found to be shorter for hard-impact and longer for soft-impact. $Length_h$ ranged from 35 to 113 data-points, while, $Length_s$ ranged from 265 to 1211 data-points.

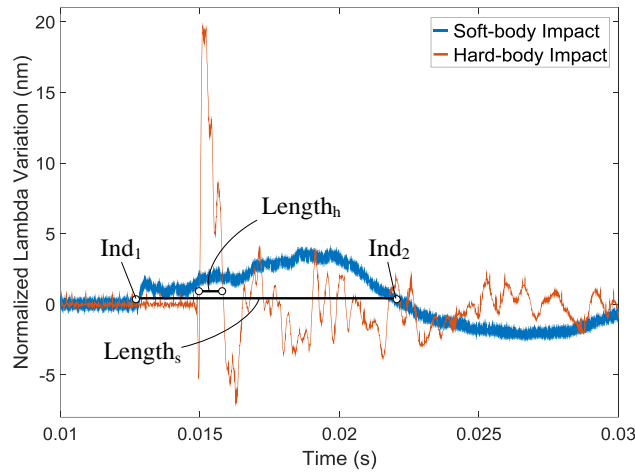


Figure 5.6 Comparison of $Length_h$ and $Length_s$.

Table 5.3 Overview of $Length_h$ and $Length_s$ at various impact test points.

a) Hard-Impact, $Length_h$				b) Soft-Impact, $Length_s$			
Impact Test Point (Figure 4.30)	FBG1	FBG2	FBG3	Impact Test Point (Figure 5.5)	FBG1	FBG2	FBG3
1	89	85	113	1	543	443	1192
2	89	61	85	4	283	505	492
3	81	111	107	5	489	423	1129
4	90	97	106	7	387	357	750
5	35	86	83	8	385	595	579
6	79	81	79	9	671	603	1093
7	97	37	47	10	265	477	807
8	74	55	113	12	733	667	771
9	100	56	73	16	1211	691	913
10	104	54	73	20	991	783	729
Minimum Length	35	37	47	Minimum Length	265	357	492
Maximum Length	104	111	113	Maximum Length	1211	783	1192

Therefore, in order to localize soft or hard-impact cases, the database used by the error outlier algorithm should consist of both the soft and hard-impact reference signals. When an impact is detected, the algorithm scans the impact signal to determine the type of impact occurrence, and based on the impact classification outcome corresponding training signal is selected for further signal processing using the weighted MAD threshold based impact localization algorithm. The overview of the soft and hard-impact localization procedure is presented in Figure 5.7.

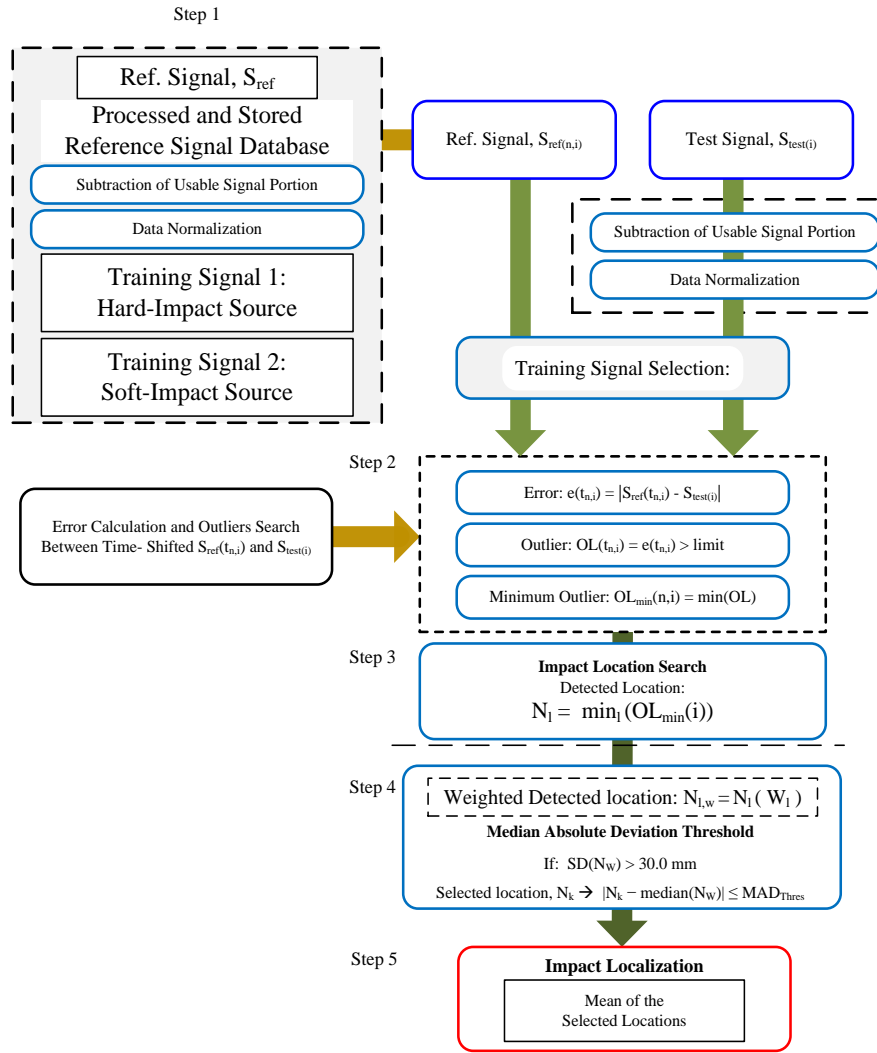


Figure 5.7 OM3 with Weighted MAD threshold algorithm for soft and hard-impact localization.

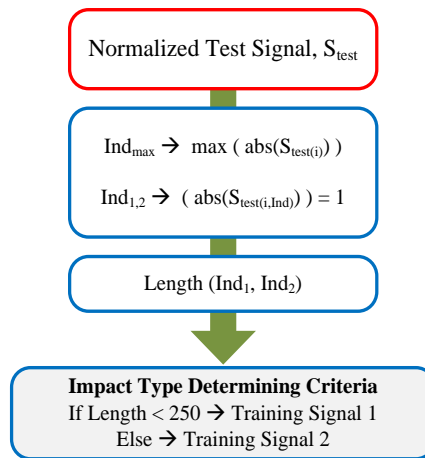


Figure 5.8 Overview of training signal selection process.

In the training signal selection process shown in Figure 5.8, the algorithm first determines the time index at which the maximum normalized lambda variation value occurs, Ind_{max} . Then the time indexes closest to the Ind_{max} , Ind_1 and Ind_2 , which results in the normalized lambda variation equal to 1 are determined. The distance between Ind_1 and Ind_2 is calculated to determine the Length parameter for impact type classification. Finally, the impact type is determined to be hard-body impact if for each of the FBG sensor impact response signal the Length is less than 250 data points or else it is classified as soft-body impact.

The weighted MAD threshold based error outlier algorithm illustrated in Figure 5.7 for soft and hard-impact localization was used for localizing trained impact and non-trained impact cases. In Section 5.3.2 the impact hammers used for constructing the reference database was used for verifying the algorithm effectiveness in classifying the impact signal. Subsequently, in section 5.3.3, non-trained impacts were localized using the algorithm consisting of hard and soft-impact training signals. 20 impact test points used for localizing the trained and non-trained impact cases are shown in Figure 5.9.

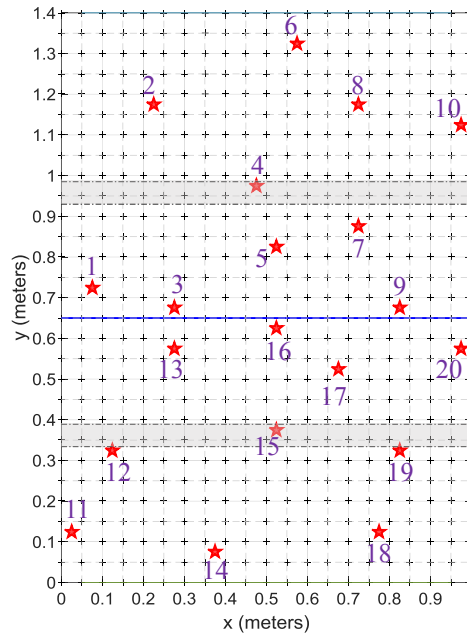


Figure 5.9 Visualization of impact test points for trained and non-trained impact localization study.

5.3.2 Classification of Trained Soft and Hard-Impact Cases

In this section, the impact type classification for soft and hard-impact cases was done for test impact delivered using the hammers, shown in Figure 5.10, which were used for training the algorithm for localizing soft and hard-impact locations. The 20 impacts on the upper and lower surface of the composite wing were delivered at impact test points presented in Figure 5.9.



Figure 5.10 Impact test hammers.

The soft and hard-impact classification results are visualized in Figure 5.11. Hard-impact classification is represented with square marker and soft-impact classification is represented with circle marker. The impacts delivered using the impact hammer with soft tip and hard tip were classified correctly as shown in Figure 5.11 (a) and (b). From the present results it can be seen that the classification method incorporated into the OM3 with weighted MAD threshold based impact localization algorithm is effective for distinguishing the impact type for trained impact cases.

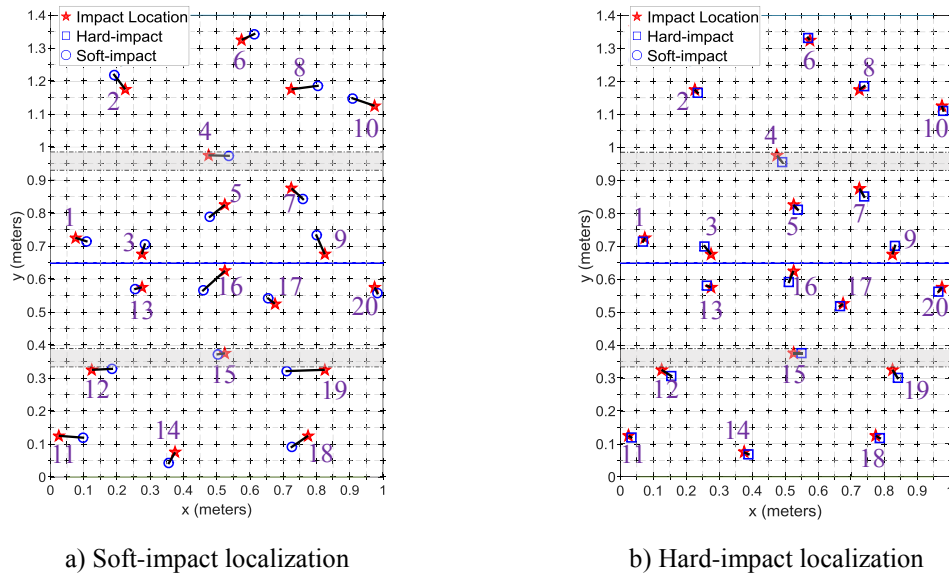


Figure 5.11 Trained impact cases classification results.

5.3.3 Classification and Localization of Non-Trained Impact Cases

Two categories of impact localization of non-trained impact were considered; impact hammer with a) small contact area, and b) large contact area. For impact hammer with small contact area impact localization, Case 1: hard tip with diameter of 5.3 mm and Case 2: soft tip with diameter of 6.2 mm, presented in Figure 5.12, were used to deliver the impact. Whereas, for impact hammer with large contact area, four impact cases shown

in Figure 5.13 were used; Case 3: diameter of 26.3 mm, Case 4: dimension of 24 mm * 24 mm, Case 5: diameter of 46.0 mm, and Case 6: diameter of 24.0 mm.



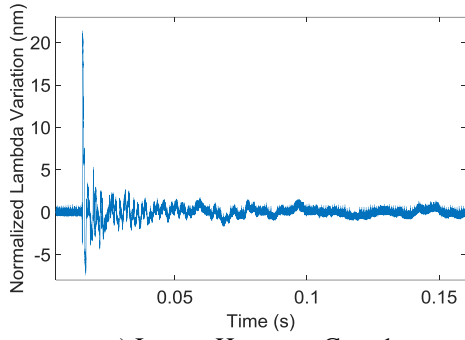
Figure 5.12 Impact hammer with small contact area.



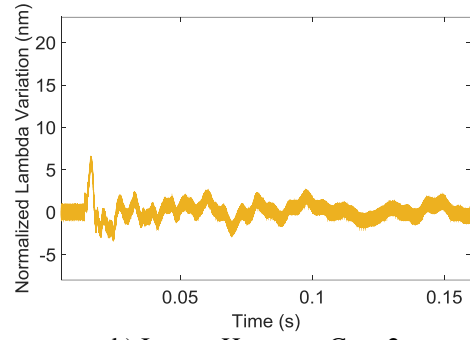
Figure 5.13 Impact hammer with large contact area.

The impact behavior of each of the impact hammers, Case 1~6, was investigated by acquiring response signal after delivering impact at Impact Test Point 5 (0.525 m, 0.825 m), on the upper surface impact test region shown in Figure 4.28. Impact hammers with small impact area, Case 1 and Case 2, FBG1 response signals are shown in Figure 5.14 and their corresponding periodogram is shown in Figure 5.15. FBG1 impact response signal obtained using impact hammer with larger contact area, Impact Hammer: Case 3~6, and the corresponding periodogram is presented in Figure 5.16 and Figure 5.17, respectively.

For each impact case the periodogram is compared with the baseline hard-impact and soft-impact periodograms. The hardness of the impact material can be inferred by analyzing and comparing the periodogram of each of the impact hammer with the base line periodograms. In Figure 5.15, it can be seen that for non-trained impact hammer with small contact area, Case 1 periodogram closely resembles the trained hard-impact case, whereas, the non-trained impact hammer Case 2 periodogram is found to be largely similar to the trained soft-impact case periodogram. For impact hammer with larger contact area, in Figure 5.17, it can be seen that impact hammer Case 3 and Case 5, overall, the power of the frequency is less than the baseline hard-impact case but higher than the soft-impact case, and impact hammer Case 3 and Case 5 periodograms are relatively similar to the baseline soft-impact periodogram. Therefore, the hardness of the impact hammers of Case 1~6 used for impact localization tests are found to range from baseline hard-impact hammer to baseline soft-impact hammer.

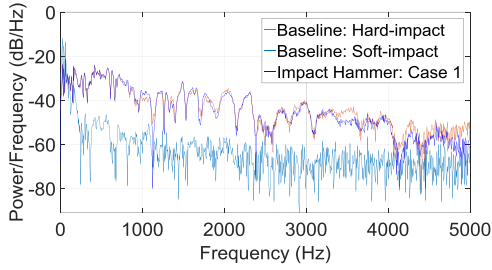


a) Impact Hammer: Case 1

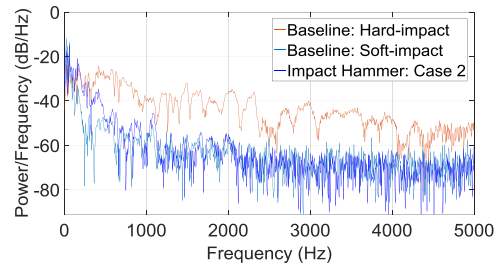


b) Impact Hammer: Case 2

Figure 5.14 FBG1 response signal for impact hammer with small contact area.

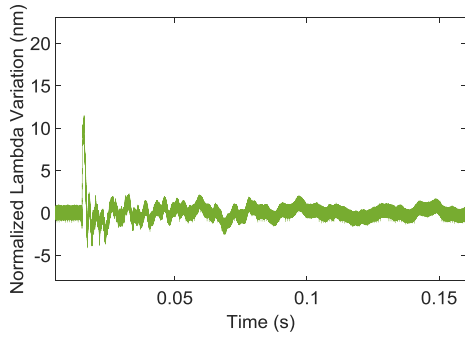


a) Impact Hammer: Case 1

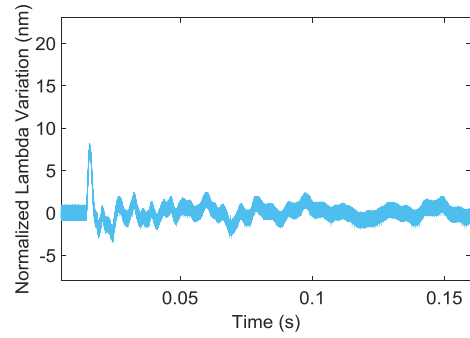


b) Impact Hammer: Case 2

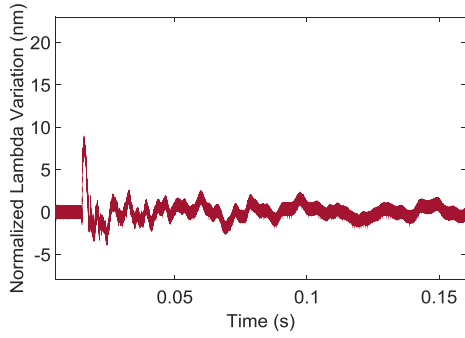
Figure 5.15 Periodogram comparison of FBG1 signal for impact hammer with small contact area.



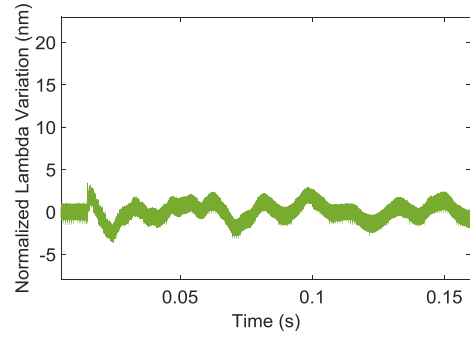
a) Impact Hammer: Case 3



b) Impact Hammer: Case 4



c) Impact Hammer: Case 5



d) Impact Hammer: Case 6

Figure 5.16 FBG1 response signal for impact hammer with large contact area.

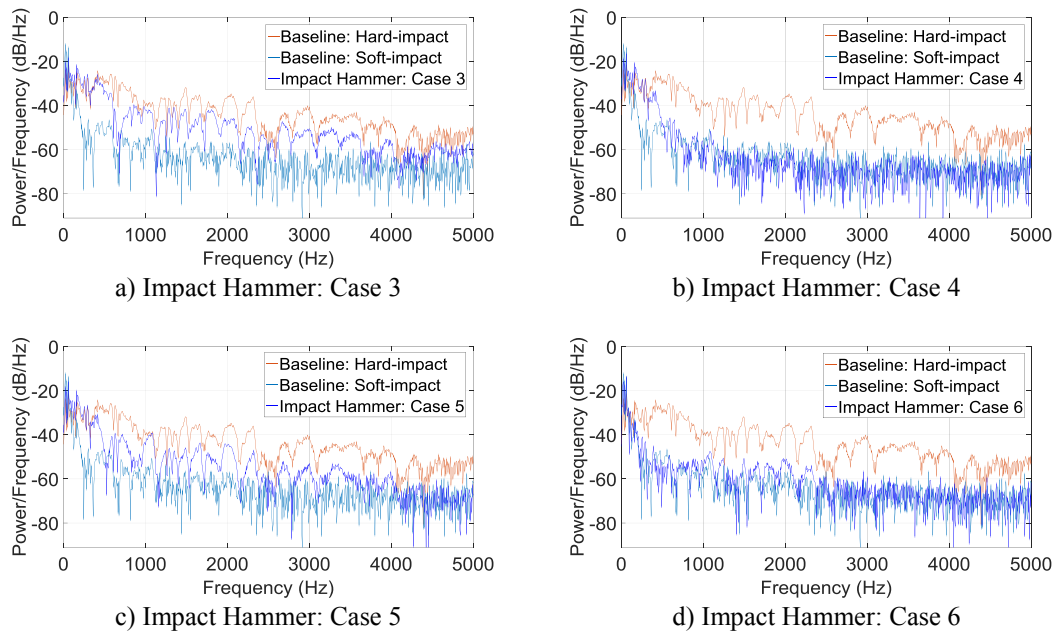
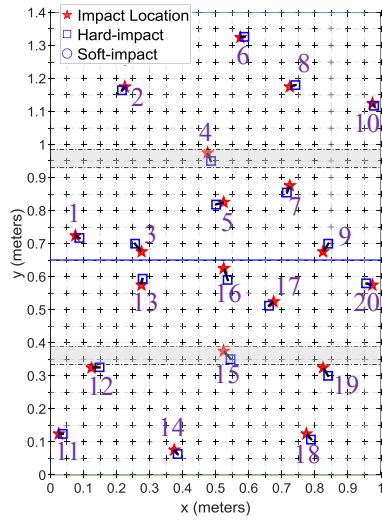


Figure 5.17 Periodogram comparison of FBG1 signal for impact hammer with large contact area.

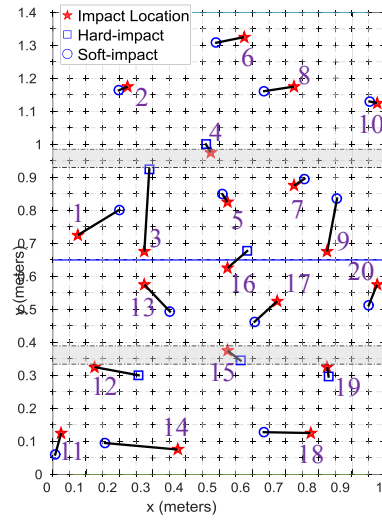
5.3.3.1 Localization Results of Non-Trained Small Contact Area Impacts

The localization results for impact delivered using impact hammer Case 1 and Case 2 are visualized in Figure 5.18 and tabulated in Table 5.4. Impacts delivered using the non-trained impact hammer Case 1 were all classified as hard-impact, and the impact test points were localized with maximum error of 37.0 mm and average error of 21.7 mm. The impact delivered using impact hammer Case 1 are found to be localized with localization accuracy similar to the trained hard-impact hammer case. Similar localization results for impact hammer Case 1 in comparison to the trained hard-impact hammer case can be attributed to similar response signal characteristics for these two impact cases, as shown for Impact Test Point 5 in Figure 5.15 (a).

Whereas, most of the non-trained impact hammer Case 2 were classified as soft-impact; out of the 20 impact cases six of the impacts were classified as hard-impacts and the remaining impacts were classified as soft. Overall, impacts delivered using the impact hammer Case 2 was localized with maximum error of 249.9 mm and average error of 93.8 mm. Moreover, the periodogram of impact hammer Case 2 for Impact Test Point 5 shown in Figure 5.15 (b) which is found to closely match the trained soft-impact periodogram was classified as soft-impact. Furthermore, it can be observed that the impacts which were classified as hard-impacts are located close to leading edge and spar region, such as Impact Test Point 3, 4, 12, 15, 16 and 19.



a) Impact Hammer: Case 1



b) Impact Hammer: Case 2

Figure 5.18 Visualization of localization results for Case 1 and Case 2 impact hammer.

Table 5.4 Localization results for Case 1 and Case 2 impact hammer.

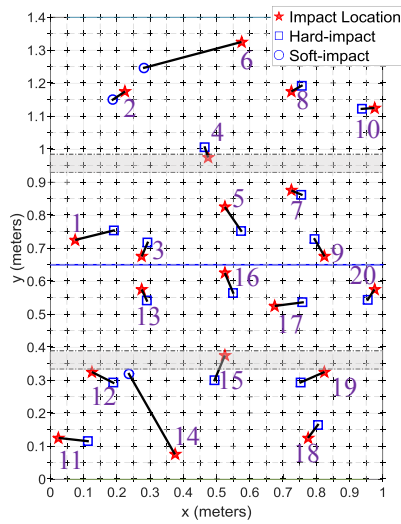
Impact Hammer	Case 1	Case 2
Maximum Error (mm)	37.0	249.9
Average Error (mm)	21.7	93.8

5.3.3.2 Localization Results of Non-Trained Large Contact Area Impacts

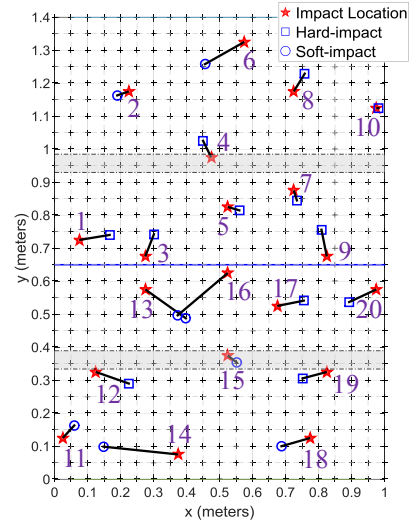
Impacts delivered using impact hammer Case 3~6 were localized using the OM3 with weighted MAD threshold algorithm. The impact localization results for non-trained impact hammer Case 3~6 are visualized in Figure 5.19 and tabulated in Table 5.5. Firstly, analysis of the impact classification corresponding to the response signal and its periodogram presented in Figure 5.16 and Figure 5.17 (a)~(d) was done. By observing the Impact Test Point 5 impact response signals presented in Figure 5.16, it can be deduced that each of the impact hammers tip used for the impact test have varying impactor hardness. For data length time less than 0.04 s, considerable changes in the response signal can be seen.

The power of the periodogram plot of impact hammer Case 3 and Case 5, shown in Figure 5.17 (a) and (c), is less compared with the trained hard-impact case but higher than trained soft-impact case. The algorithm classified the impact given using impact hammer Case 3 and Case 5 as hard-impact. In case of impact hammer Case 4, for frequency range between 0~500 Hz the power is relatively higher than the trained soft-impact case and closer to the trained hard-impact case, however for frequency range over 500 Hz, the power matches closely with the trained soft-impact case. Interestingly, the algorithm classified this impact case as hard-impact. Impact delivered at Impact Test Point 5 using impact hammer Case 6 was classified as soft-impact; the power of

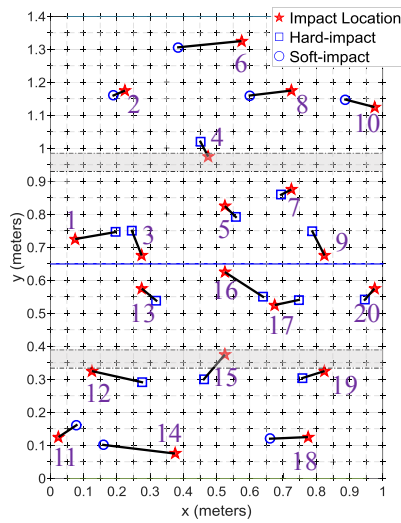
periodogram plot shown in Figure 5.17 (d) of the FBG1 impact response signal shows similar trend as that of trained soft-impact case for frequency range from 0 Hz to 5000 Hz. The impact delivered at Impact Test Point 5 using impact hammer Case 3~6 were localized with error of 87.4 mm, 36.5 mm, 46.8 mm and 82.9 mm, respectively.



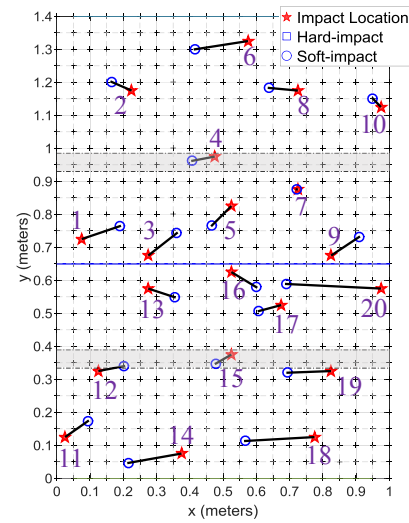
a) Impact Hammer: Case 3



b) Impact Hammer: Case 4



c) Impact Hammer: Case 5



d) Impact Hammer: Case 6

Figure 5.19 Visualization of localization results for impact hammer Case 3~6.

Table 5.5 Localization results for impact hammer Case 3~6.

Impact Hammer	Case 3	Case 4	Case 5	Case 6
Maximum Error (mm)	303.1	227.7	217.2	285.6
Average Error (mm)	83.7	86.3	94.8	104.1

Furthermore, the impacts delivered using impact hammer Case 3 were mostly classified as hard-impact except for Impact Test Point 2, 6 and 14. Impact Test Point 6 and 14 were localized with large error, 303.1 mm and 280.0 mm, respectively. However, most of the impact test points were localized with average error of 83.7 mm. For impact hammer Case 4, most of the impact on the upper surface were classified as hard-impact and most of the impact on the lower wing surface were classified as soft-impact. The localization algorithm classified Impact Test Point 2, 6, 11, 13, 14, 15, 16 and 18 as soft-impact and the remaining impact test points were classified as hard-impact. The impact test points for impact hammer Case 4 were localized with average error of 86.3 mm and Impact Test Point 14 was localized with maximum localization error of 227.7 mm. Similarly, for impact hammer Case 5 with the largest impact contact area, 13 impact test points were classified as hard-impact and 7 impact test points were classified as soft-impact. The impact test points were localized with average error of 94.8 mm and Impact Test Point 14 was localized with maximum error of 217.2 mm. Finally, for impact hammer Case 6, all of the impacts were classified as soft-impact and these impacts were localized with average error of 104.1 mm and Impact Test Point 20 was localized with maximum error of 285.6 mm. The impacts at Impact Test Point 5 delivered using impact hammer Case 3~5 were classified as hard-impact and Case 6 was classified as soft-impact. Given that the classification algorithm selects the impact type based on the Length criteria, the Length for each of the response signal obtained by delivering impact at Impact Test Point 5 using impact hammer Case 3~5 was less than 250 data-points, therefore they were all classified as hard-impact.

Except for impact hammer Case 6 for which all the impacts were classified as soft-impact, for impact case 3~5 the impact classification is not as unanimous for impact delivered at various location. From the classification results of impacts delivered at the 20 impact test points for impact hammer Case 3~5, shown in Figure 5.19, a pattern in the way the impacts were classified can be observed. In general, if the hardness of the impact hammer tip used for simulating impact is not similar to the tip of the trained impact hammer but harder than the trained soft-impact hammer then the impacts located at the rigid portion of the wing surface, the surface region bounded by the wing's leading edge and the spar region, were likely to be classified as hard-impact, and impacts located close to the trailing edge of the wing were likely to be classified as soft-impact. As a result, the classification results for impact hammer Case 3~5 were found to be varied.

Although the impacts delivered using the non-trained impact hammer were localized with relatively larger localization error, overall, it can be seen that the impact delivered using the non-trained impact hammers were localized with average error of about 100.0 mm or less. Moreover, the impact localization performance of the error outlier based impact localization algorithm trained using two extreme impact hardness cases is found to be effective for localizing both trained and non-trained impact sources.

5.3.4 Impact Localization Using Reduced Data Points

Increasing the data length used for localizing the impact location considerably increases the computation time as presented in Section 5.2. Therefore, in this section the localization of the trained and non-trained soft and hard-impacts were localized by reducing the sampling rate of the impact from 100 kHz to 33 kHz. The localization study was done using the trained and non-trained impact cases presented in Section 5.3.2 and 5.3.3. The impact localization done using response signal with data sampling rate of 33 kHz and 100 kHz are compared in Figure 5.20 and the computation time for these two cases are tabulated in Table 5.6.

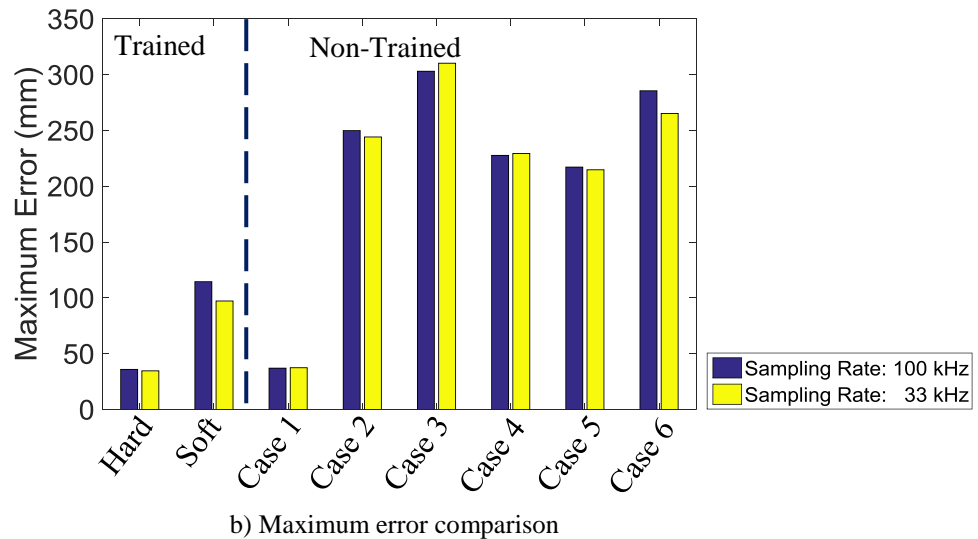
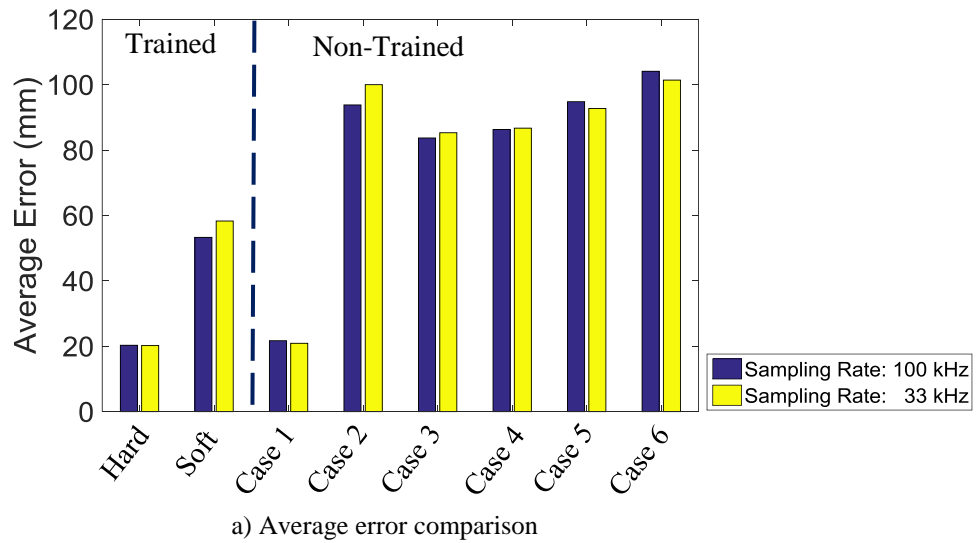


Figure 5.20 Localization performance comparison.

Using the response signal with reduced number of data points, similar localization performance can be observed for the trained and non-trained soft and hard-impact cases compared to the localization done using response signal data acquired using sampling rate of 100 kHz. Therefore, it can be concluded that the impact localization can be done using 33 kHz sampling rate. Furthermore, by reducing the sampling rate to 33 kHz, the

computation time required for localizing both the soft and hard-impact can be significantly improved. In case of the hard-impact, the computation time was reduced from 15.5 s to 2.0 s. Whereas, for the soft-impact the computation time was reduced from 148.7 s to 17.1 s.

Table 5.6 Computation time comparison.

Sampling Rate	100 kHz	33 kHz
Hard-Impact	15.5 s	2.0 s
Soft-Impact	148.7 s	17.1 s

5.4 Summary

In this chapter, classification and localization of impact using error outlier based impact localization algorithm on composite wing structure was presented. The data length between two time indexes located closest to the peak amplitude of the impact signal was proposed as the feature for classifying hard and soft-impact. This classification technique was integrated into the OM3 with weighted MAD threshold algorithm for localizing impact delivered on the composite wing using trained impact hammer and non-trained impact hammer cases.

Firstly, the soft-impact training signals were obtained from the reference points and feasibility study of localizing impact hammer with soft tip was performed. The localization results show that the error outlier based impact localization algorithm can also be used effectively for localizing soft-impact on composite wing. However, in comparison to hard-impacts localized using the error outlier based impact localization algorithm, the soft-impacts were localized with relatively larger error. Additionally, in comparison to hard-impact cases, longer data length was required for localizing soft-impacts for better localization results. The soft-impacts were localized with average error of 48.5 mm and maximum error of 111.0 mm using 0.14 s data length. Subsequently, validation of the classification technique integrated into the OM3 with weighted MAD threshold based impact localization algorithm was performed. Classification of impacts delivered using the trained soft and hard impactor was done and the results shows that all of the impacts were classified correctly.

Further investigation of the OM based impact localization algorithm was performed to determine its capability for classification and localization of non-trained impact cases with small and large contact area. The non-trained impacts were localized with larger localization error than the trained impact cases. However, the overall impacts on the wing surface delivered using the non-trained impacts were localized with average error of about 80.7 mm and the maximum error for non-trained impact cases ranged from 217.2 mm to 303.1 mm. Considering that the localized impacts were localized using training signals obtained using only two different hammer with soft and hard impactor, the obtained results were found to be satisfactory.

Chapter 6. Conclusions

Low velocity impact on composite structures poses serious threat to the safety and integrity of the composite structures as it can lead to occurrence of BVID. Therefore, the research presented in this dissertation focused on localization of low velocity impact on complex composite structures. A novel localization method based on error outlier assessment was proposed. In the past, detection of outliers has been used for various applications ranging from medical diagnosis, to credit card fraud detection and for damage detection. Therefore, for quick and effective localization tool development, a novel impact localization algorithms based on error outlier assessment method was developed and successfully validated on a complex composite structure, Jabiru UL-D aircraft's (Jabiru Aircraft Pty Ltd, Australia) composite wing, monitored using multiplexed FBG sensors.

Feasibility of using 1D array configuration to estimate the location of the impact has been demonstrated in Chapter 3. Using 1D array FBG sensor configuration and reference database algorithm, similar localization capability as obtained using 2D array FBG sensor configuration was observed. Therefore, the number of required sensors for impact localization can be drastically reduced by using 1D array FBG sensor configuration. Moreover, the use of 1D array for impact localization application enables easier FBG installation on composite structures in terms of wiring issues. Single sensor parametric were done to determine the feasibility of using single sensor for localizing impact on complex composite structures. Moreover, from the parametric study it was observed that it is possible to use few number sensors for impact localization; two FBG sensors to detect impact on wing spanning 4.2 m with localization error similar to that of 1D array FBG configuration consisting of three or six FBG sensors.

Subsequently, in Chapter 4, novel method for localizing impacts using error outlier based impact localization algorithms were proposed and developed. The error outlier based impact localization algorithms with user-set distance threshold method and statistically determined distance threshold methods for selecting the likely impact locations were investigated. In case of user-set distance threshold, the error outlier based impact localization algorithm with Euclidean distance threshold was used which was referred to as OM2 algorithm. Then, three different statistical methods for selection of distance threshold were investigated: 1) Standard Deviation threshold method, 2) Median Absolute Deviation threshold method and 3) weighted Median Absolute Deviation threshold method, which were referred to as OM3 with SD threshold method, OM3 with MAD threshold method and OM3 with weighted MAD threshold method, respectively. Localization performance of OM1 and OM2 algorithms were sensitive to a) error threshold parameter, b) NAO parameter and c) number of allowed location, k value. Whereas, the OM3 algorithm was a simplified version of OM algorithm and its localization performance was sensitive to only two parameters; a) error threshold parameter, and b) k value. In

brief, it was found that lower error threshold value, higher NAO and lower k value are suitable for optimal localization performance.

The error outlier assessment based impact localization technique was found to be an effective tool for localizing low velocity impacts. Among the three different statistical threshold methods examined for impact location selection, OM3 with weighted MAD threshold was determined as the best method. Furthermore, OM2 with user-set distance Euclidean distance threshold and OM3 with weighted MAD threshold algorithms are found to have similar localization performance. Both of these methods localized impact on complex composite wing structure with average error of about 18.0 mm and maximum error of about 42.0 mm. Additionally, using OM3 with weighted MAD threshold algorithm, impacts delivered on composite wing under simulated wing loading condition were also localized with similar localization performance; average error of about 22.1 mm and maximum error of about 50.8 mm. Also, it was demonstrated that the error outlier based impact localization algorithm is capable of localizing impact using a single FBG sensor.

Impact localization algorithm capable of localizing various different impact cases, and not only trained impact cases but also non-trained impact cases is highly desirable. The impact localization tests done using error outlier based impact localization algorithms, presented in Chapter 4, using impact hammer with hard tip were localized close to the actual impact location. However, if the same algorithm consisting of hard-impact reference database were to be used for localizing soft-impact it would result in large localization error as the response signal for soft and hard-impact were found to be dissimilar. Therefore, new database consisting of impact signals obtained using impact hammer with soft tip was constructed for the soft-impact feasibility study. Error outlier based impact localization algorithm was able to localize soft-impact, however the algorithm required longer data length and the localization error was relatively larger compared with hard-impact localization results. Using data length time of 0.14 s, the soft-impacts were localized with average error of 48.5 mm and maximum error of 111.0 mm.

In order for the algorithm to localize the soft and hard-impacts the algorithm should be able to distinguish the impact type and then select the corresponding training signal from the reference database for impact localization. Therefore, the data length between two time indexes located closest to the peak amplitude of the impact signal was proposed as the feature for classifying hard and soft-impact and this method was integrated into the OM3 with weighted MAD threshold algorithm. Firstly, the classification of trained soft and hard-impact cases, i.e. the hammer used for constructing the reference database, were done; the corresponding impacts were classified correctly. Subsequently, classification and localization of non-trained impact cases were performed and compared to the trained cases, the non-trained impact cases were localized with larger error. The non-trained impacts were localized with average error of about 80.7 mm and the maximum error for non-trained impact cases ranged from 217.2 mm to 303.1 mm.

Although the OM algorithm shows good localization performance, there are several limitations of using this method. The proposed localization technique is only capable of localizing single impact event. Also, since the localization technique presented in this thesis is based on reference database method, acquisition of the training signals for large scale structures can be time consuming and labor intensive. Furthermore, the accuracy of the localization results of the impact depend on whether or not the database consists of the training signal for the corresponding impact being localized. Consequently, the trained impact cases were localized more accurately than the non-trained impact cases. From the present research the spar region, leading edge region and the edge of the impact test region were identified as region vulnerable to larger localization error. Additionally, further study of impact localization during operational condition is required to realize such SHM system for real-world application.

Nevertheless, the present study demonstrates the effectiveness of a novel approach to localizing impacts on composite structures using error outlier method. Using the error outlier based impact localization algorithm proposed in this thesis, the trained and non-trained impact delivered using impact hammer with varying impactor hardness were well localized and the overall results were found to be satisfactory. In addition to the improved localization performance, the OM based impact localization tool provides a simple and quick technique to localize low velocity impacts on large scale structures, which involves data acquisition using a large number of sensors. Furthermore, this method is not limited to localizing structural impacts but can also be implemented in a wide range of fields pertaining to localization applications, such as remote sensing, Global Positioning System, surveillance system etc. At present, for large scale structures such as aircraft, spacecraft etc., large number of sensor requirement and, the complexity and high cost involved in data acquisition process poses hindrance in the implementation of SHM system for real world application. However, SHM system are crucial for ensuring the integrity and safety of such structures. Therefore, the use of 1D array configuration coupled with OM based impact localization algorithm can be effective in reducing the complexity involved in sensor wiring and data processing issues for detecting impacts on complex large composite structures.

Bibliography

- [1] R. M. Jones, *Mechanics of Composite Materials*. CRC Press, 1998.
- [2] “Aviation Safety: Status of FAA’s actions to oversee the safety of composite airplanes,” US Government Accountability of Office Report: GAO-11-849, 2011.
- [3] W. G. Roeseler, B. Sarh, and M. U. Kismarton, “Composite structures: The first 100 years,” in *16th International Conference on Composite Materials*, 2007, pp. 1–10.
- [4] N. V. Bhat, “Delamination growth in graphite/epoxy composite laminates under tensile loading,” Thesis, Massachusetts Institute of Technology, 1993.
- [5] K. Reifsnider, “Fatigue behavior of composite materials,” *Int. J. Fract.*, vol. 16, no. 6, pp. 563–583, 1980.
- [6] K. N. Shivakumar, W. Elber, and W. Illg, “Prediction of low-velocity impact damage in thin circular laminates,” *AIAA J.*, vol. 23, no. 3, pp. 442–449, Mar. 1985.
- [7] W. J. Cantwell and J. Morton, “The impact resistance of composite materials - a review,” *Composites*, vol. 22, no. 5, pp. 347–362, 1991.
- [8] A. Baker, S. Dutton, and D. Kelly, *Composite Materials for Aircraft Structures*. AIAA, 1986.
- [9] P. O. Sjoblom, J. T. Hartness, and T. M. Cordell, “On low-velocity impact testing of composite materials,” *J. Compos. Mater.*, vol. 22, no. 1, pp. 30–52, 1988.
- [10] W. Cantwell, P. Curtis, and J. Morton, “Impact and subsequent fatigue damage growth in carbon fibre laminates,” *Int. J. Fatigue*, vol. 6, no. 2, pp. 113–118, 1984.
- [11] W. Simon, “Damage/Defect types and inspection-some regulatory concerns,” in *Presentation at the Composite Damage Tolerance and Maintenance Workshop*, 2006.
- [12] L. Cartz, *Nondestructive Testing: Radiography, Ultrasonics, Liquid Penetrant, Magnetic Particle, Eddy Current*. Asm International, 1995.
- [13] C. Scarponi and G. Briotti, “Ultrasonic technique for the evaluation of delaminations on CFRP, GFRP, KFRP composite materials,” *Compos. Part B Eng.*, vol. 31, no. 3, pp. 237–243, Apr. 2000.
- [14] P. M. Delpach, D. M. Boscher, F. Lepoutre, A. A. Déom, and D. L. Balageas, “Quantitative Nondestructive Evaluation of Carbon-Carbon Composites by Pulsed Infrared Thermography,” in *Review of Progress in Quantitative Nondestructive Evaluation: Volumes 12A and 12B*, D. O. Thompson and D. E. Chimenti, Eds. Boston, MA: Springer US, 1993, pp. 1297–1304.
- [15] K. T. Tan, N. Watanabe, and Y. Iwahori, “X-ray radiography and micro-computed tomography examination of damage characteristics in stitched composites subjected to impact loading,” *Compos. Part B Eng.*, vol. 42, no. 4, pp. 874–884, Jun. 2011.
- [16] W. B. Spillman Jr and R. O. Claus, “Sensory phenomena and measurement instrumentation for smart structures and materials,” in *5th Annual International Symposium on Smart Structures and Materials*, 1998, pp. 2–5.
- [17] E. Udd, “Early efforts to initiate the field of fiber optic smart structures at McDonnell Douglas,” 1998, vol. 3330, pp. 12–18.
- [18] C. M. Dry, “Matrix cracking repair and filling using active and passive modes for smart timed release of chemicals from fibers into cement matrices,” *Smart Mater. Struct.*, vol. 3,

- no. 2, pp. 118–123, 1994.
- [19] C. M. Dry, “Smart multiphase composite materials that repair themselves by a release of liquids that become solids,” in *1994 North American Conference on Smart Structures and Materials*, 1994, vol. 2189, pp. 62–70.
 - [20] W. Staszewski, C. Boller, and G. Tomlinson, *Health Monitoring of Aerospace Structures: Smart Sensor Technologies and Signal Processing*. John Wiley & Sons, 2004.
 - [21] C. R. Farrar and K. Worden, “An introduction to structural health monitoring,” *Philos. Trans. R. Soc. A Math. Phys. Eng. Sci.*, vol. 365, no. 1851, pp. 303–315, 2007.
 - [22] B. Glisic and D. Inaudi, *Fibre optic methods for structural health monitoring*. John Wiley & Sons, 2008.
 - [23] D. Balageas, C.-P. Fritzen, and A. Güemes, *Structural Health Monitoring*. London ; Newport Beach, CA: ISTE, 2006.
 - [24] C. Boller, “Ways and options for aircraft structural health management,” *Smart Mater. Struct.*, vol. 10, no. 3, pp. 432–440, 2001.
 - [25] G. Park, H. Sohn, C. R. Farrar, and D. J. Inman, “Overview of piezoelectric impedance-based health monitoring and path forward,” *Shock Vib. Dig.*, vol. 35, no. 6, pp. 451–463, 2003.
 - [26] R. M. Measures, *Structural Monitoring with Fiber Optic Technology*. San Diego, Calif.: Academic Press, 2001.
 - [27] S. Galea and I. Powlesland, “Caribou loads flight survey using a rapid operational loads measurement approach,” in *Materials Forum*, 2008, vol. 33, pp. 100–109.
 - [28] N. Furstenau, D. D. Jansen, and W. Schmidt, “In-flight strain measurements on structurally integrated composite plates using fiber-optic interferometric strain gauges,” *Smart Mater. Struct.*, vol. 2, no. 3, p. 147, 1993.
 - [29] J.-H. Kim, Y. Park, Y.-Y. Kim, P. Shrestha, and C.-G. Kim, “Aircraft health and usage monitoring system for in-flight strain measurement of a wing structure,” *Smart Mater. Struct.*, vol. 24, no. 10, pp. 1–12, 2015.
 - [30] D. Sung, C. Kim, and C. Hong, “Monitoring of impact damages in composite laminates using wavelet transform,” *Compos. Part B Eng.*, vol. 33, no. 1, pp. 35–43, 2002.
 - [31] Y. An, M. K. Kim, and H. Sohn, “Airplane hot spot monitoring using integrated impedance and guided wave measurements,” *Struct. Control Heal. Monit.*, vol. 19, no. 7, pp. 592–604, 2012.
 - [32] C. M. Yeum, H. Sohn, J. B. Ihn, and H. J. Lim, “Instantaneous delamination detection in a composite plate using a dual piezoelectric transducer network,” *Compos. Struct.*, vol. 94, no. 12, pp. 3490–3499, 2012.
 - [33] T. Ogisu, M. Shimanuki, S. Kiyoshima, Y. Okabe, and N. Takeda, “Development of damage monitoring system for aircraft structure using a PZT actuator/FBG sensor hybrid system,” 2004, vol. 5388, pp. 425–436.
 - [34] W. H. Kinard, “Micrometeoroid penetration measuring device,” 1968.
 - [35] K. Hale, “The application of optical fibres to structural integrity monitoring,” in *Oceans* 82, 1982, pp. 344–348.
 - [36] R. Crane, A. Macander, and J. Gagorik, “Fiber Optics for a Damage Assessment System for Fiber Reinforced Plastic Composite Structures,” in *Review of Progress in Quantitative Nondestructive Evaluation*, vol. 2A, D. Thompson and D. Chimenti, Eds. Springer US, 1983, pp. 1419–1430.

- [37] B. Hofer, "Fiber optic damage detection in composite structures," *Composites*, vol. 18, no. 4, pp. 309–316, 1987.
- [38] A. D. Kersey, "A review of recent developments in fiber optic sensor technology," *Opt. Fiber Technol.*, vol. 2, no. 3, pp. 291–317, 1996.
- [39] K. T. V. Grattan and B. T. Meggitt, *Optical Fiber Sensor Technology Advanced Applications - Bragg Gratings and Distributed Sensors*, vol. 5. Springer, 2000.
- [40] S. Y. Yin, Francis T. S., "Overview of Fiber Optic Sensors," *Fiber Opt. Sensors*, p. 495, 2002.
- [41] C. Chang and J. S. Sirkis, "Design of fiber optic sensor systems for low velocity impact detection," *Optimization*, vol. 7, no. 2, pp. 166–177, 1998.
- [42] D.-U. Sung, J.-H. Oh, C.-G. Kim, and C.-S. Hong, "Impact monitoring of smart composite laminates using neural network and wavelet analysis," *J. Intell. Mater. Syst. Struct.*, vol. 11, no. 3, pp. 180–190, 2000.
- [43] N. Elvin and C. Leung, "Feasibility study of delamination detection with embedded optical fibers," *J. Intell. Mater. Syst. Struct.*, vol. 8, no. 10, pp. 824–828, 1997.
- [44] S. Takeda, Y. Okabe, and N. Takeda, "Delamination detection in CFRP laminates with embedded small-diameter fiber Bragg grating sensors," *Compos. Part A Appl. Sci. Manuf.*, vol. 33, no. 7, pp. 971–980, 2002.
- [45] Y. Xu, C. K. Y. Leung, Z. Yang, P. Tong, and S. K. L. Lee, "A new fiber optic based method for delamination detection in composites," *Struct. Heal. Monit.*, vol. 2, no. 3, pp. 205–223, 2003.
- [46] L. Everall, A. Gallon, and D. Roberts, "Optical fibre strain sensing for practical load monitoring," *Sens. Rev.*, vol. 20, no. 2, pp. 113–119, 2000.
- [47] Y. Okabe, S. Yashiro, T. Kosaka, and N. Takeda, "Detection of transverse cracks in CFRP composites using embedded fiber Bragg grating sensors," *Smart Mater. Struct.*, vol. 9, no. 6, pp. 832–838, 2000.
- [48] N. Takeda, T. Kosaka, and T. Ichiyama, "Detection of transverse cracks by embedded plastic optical fiber in FRP laminates," in *Smart Structures and Materials 1999: Sensory Phenomena and Measurement Instrumentation for Smart Structures and Materials*, 1999, vol. 3670, no. May, pp. 248–255.
- [49] D. C. Lee, J. J. Lee, I. B. Kwon, and D. C. Seo, "Monitoring of fatigue damage of composite structures by using embedded intensity-based optical fiber sensors," *Smart Mater. Struct.*, vol. 10, no. 2, pp. 285–292, 2001.
- [50] I. Takahashi, K. Sekine, M. Kume, H. Takeya, Y. Iwahori, S. Minakuchi, N. Takeda, and K. Enomoto, "Structural health monitoring of CFRP airframe structures using fiber-optic-based strain mapping," in *Proc. SPIE 8345, Sensors and Smart Structures Technologies for Civil, Mechanical, and Aerospace Systems 2012*, 2012, vol. 8345, pp. 834531–1.
- [51] K. Hyun-Kyu, P. Jae-Sung, K. Dong-Hoon, K. Cheol-Ung, H. Chang-Sun, and K. Chun-Gon, "Strain monitoring of a filament wound composite tank using fiber Bragg grating sensors," *Smart Mater. Struct.*, vol. 11, no. 6, p. 848, 2002.
- [52] N. Mrad, H. Guo, G. Xiao, B. Rocha, and Z. Sun, "On the use of a compact optical fiber sensor system in aircraft structural health monitoring," in *Proc. SPIE 8368, Photonic Applications for Aerospace, Transportation, and Harsh Environment III*, 2012, vol. 8368, p. 836808.
- [53] A. Panopoulou, D. Roulias, T. H. Loutas, and V. Kostopoulos, "Health monitoring of aerospace structures using fibre Bragg gratings combined with advanced signal

- processing and pattern recognition techniques,” *Strain*, vol. 48, no. 3, pp. 267–277, 2012.
- [54] J.-R. Lee, C.-Y. Ryu, B.-Y. Koo, S.-G. Kang, C.-S. Hong, and C.-G. Kim, “In-flight health monitoring of a subscale wing using a fiber Bragg grating sensor system,” *Smart Mater. Struct.*, vol. 12, no. 1, pp. 147–155, 2003.
 - [55] K. Chandler, S. Ferguson, T. Graver, A. Csipkes, and A. Mendez, “On-line structural health and fire monitoring of a composite personal aircraft using an FBG sensing system,” in *Proc. SPIE 6933, Smart Sensor Phenomena, Technology, Networks, and Systems 2008*, 2008, vol. 6933, pp. 1–6.
 - [56] I. Kressel, A. Handelman, Y. Botsev, J. Balter, P. Guedj, N. Gorbato, M. Tur, A. C. R. Pillai, M. H. Prasad, and N. Gupta, “Evaluation of flight data from an airworthy structural health monitoring system integrally embedded in an unmanned air vehicle,” in *6th European Workshop on Structural Health Monitoring*, 2012, pp. 193–200.
 - [57] J. R. Lee, H. Tsuda, and N. Toyama, “Impact wave and damage detections using a strain-free fiber Bragg grating ultrasonic receiver,” *NDT E Int.*, vol. 40, no. 1, pp. 85–93, 2007.
 - [58] D. Liu and L. E. Malvern, “Matrix cracking in impacted glass/epoxy plates,” *J. Compos. Mater.*, vol. 21, no. 7, pp. 594–609, 1987.
 - [59] S. P. Joshi and C. T. Sun, “Impact induced fracture in a laminated composite,” *J. Reinf. Plast. Compos.*, vol. 19, no. January, pp. 51–66, 1985.
 - [60] J. C. Prichard and P. J. Hogg, “The role of impact damage in post-impact compression testing,” *Composites*, vol. 21, no. 6, pp. 503–511, 1990.
 - [61] A. Tobias, “Acoustic-emission source location in two dimensions by an array of three sensors,” *Non-Destructive Test.*, vol. 9, no. 1, pp. 9–12, 1976.
 - [62] F. Ciampa and M. Meo, “Impact detection in anisotropic materials using a time reversal approach,” *Struct. Heal. Monit.*, vol. 11, no. 1, pp. 43–49, 2012.
 - [63] L. Qiu, S. Yuan, X. Zhang, and Y. Wang, “A time reversal focusing based impact imaging method and its evaluation on complex composite structures,” *Smart Mater. Struct.*, vol. 20, no. 10, p. 105014, 2011.
 - [64] H. Jeong and Y.-S. Jang, “Wavelet analysis of plate wave propagation in composite laminates,” *Compos. Struct.*, vol. 49, no. 4, pp. 443–450, 2000.
 - [65] M. Meo, G. Zumpano, M. Piggott, and G. Marengo, “Impact identification on a sandwich plate from wave propagation responses,” *Compos. Struct.*, vol. 71, no. 3–4, pp. 302–306, 2005.
 - [66] F. Ciampa and M. Meo, “Acoustic emission source localization and velocity determination of the fundamental mode A0 using wavelet analysis and a Newton-based optimization technique,” *Smart Mater. Struct.*, vol. 19, no. 4, p. 45027, 2010.
 - [67] T. Kundu, S. Das, S. A. Martin, and K. V. Jata, “Locating point of impact in anisotropic fiber reinforced composite plates,” *Ultrasonics*, vol. 48, no. 3, pp. 193–201, 2008.
 - [68] B.-W. Jang, Y.-G. Lee, J.-H. Kim, Y.-Y. Kim, and C.-G. Kim, “Real-time impact identification algorithm for composite structures using fiber Bragg grating sensors,” *Struct. Control Heal. Monit.*, vol. 19, no. 7, pp. 580–591, 2012.
 - [69] P. Shrestha, J. H. Kim, Y. Park, and C. G. Kim, “Impact localization on composite wing using 1D array FBG sensor and RMS/correlation based reference database algorithm,” *Compos. Struct.*, vol. 125, pp. 159–169, 2015.
 - [70] J.-H. Kim, Y.-Y. Kim, Y. Park, and C.-G. Kim, “Low-velocity impact localization in a stiffened composite panel using a normalized cross-correlation method,” *Smart Mater.*

Struct., vol. 24, no. 4, p. 45036, 2015.

- [71] M. A. Maseras-Gutierrez, W. J. Staszewski, M. S. Found, and K. Worden, "Detection of impacts in composite materials using piezoceramic sensors and neural networks," in *Proc. SPIE 3329, Smart Structures and Materials 1998: Smart Structures and Integrated Systems*, 1998, vol. 3329, pp. 491–497.
- [72] M. Ruiz, L. E. Mujica, X. Berjaga, and J. Rodellar, "Partial least square/projection to latent structures (PLS) regression to estimate impact localization in structures," *Smart Mater. Struct.*, vol. 22, no. 2, p. 25028, 2013.
- [73] B. Park, H. Sohn, S. E. Olson, M. P. DeSimio, K. S. Brown, and M. M. Derriso, "Impact localization in complex structures using laser-based time reversal," *Struct. Heal. Monit.*, vol. 11, no. 5, pp. 577–588, 2012.
- [74] S. Yuan, Y. Zhong, L. Qiu, and Z. Wang, "Two-dimensional near-field multiple signal classification algorithm-based impact localization," *J. Intell. Mater. Syst. Struct.*, vol. 26, no. 4, pp. 400–413, 2015.
- [75] C. Y. Park, J. H. Kim, S.-M. Jun, and C.-G. Kim, "Localizations and force reconstruction of low-velocity impact in a composite panel using optical fiber sensors," *Adv. Compos. Mater.*, vol. 21, no. February 2013, pp. 1–13, 2012.
- [76] J. Frieden, J. Cugnoni, J. Botsis, and T. Gmür, "Low energy impact damage monitoring of composites using dynamic strain signals from FBG sensors – Part I: Impact detection and localization," *Compos. Struct.*, vol. 94, no. 2, pp. 438–445, 2012.
- [77] E. Kirkby, R. de Oliveira, V. Michaud, and J. A. Månson, "Impact localisation with FBG for a self-healing carbon fibre composite structure," *Compos. Struct.*, vol. 94, no. 1, pp. 8–14, 2011.
- [78] C. Hiche, C. K. Coelho, A. Chattopadhyay, and M. Seaver, "Impact localization on complex structures using FBG strain amplitude information," in *Proc. SPIE 7649, Nondestructive Characterization for Composite Materials, Aerospace Engineering, Civil Infrastructure, and Homeland Security*, 2010, vol. 7649, p. 764903.
- [79] C. Hiche, C. K. Coelho, and A. Chattopadhyay, "A strain amplitude-based algorithm for impact localization on composite laminates," *J. Intell. Mater. Syst. Struct.*, vol. 22, no. 17, pp. 2061–2067, 2011.
- [80] S. O. Park, B. W. Jang, Y. G. Lee, Y. Y. Kim, C. G. Kim, C. Y. Park, and B. W. Lee, "Detection of impact location for composite stiffened panel using FBG sensors," *Adv. Mater. Res.*, vol. 123–125, pp. 895–898, 2010.
- [81] B.-W. Jang, Y.-G. Lee, C.-G. Kim, and C.-Y. Park, "Impact source localization for composite structures under external dynamic loading condition," *Adv. Compos. Mater.*, no. ahead-of-print, pp. 1–16, 2014.
- [82] J.-H. Kim, "Impact Localization and In-flight Strain Measurement of Aircraft Wing Structure Using Fiber Bragg Grating Sensors," PhD Thesis, KAIST, Daejeon, 2016.
- [83] E. Udd, *Fiber Optic Sensors: An Introduction for Engineers and Scientists*. Wiley, 1991.
- [84] K. T. V Grattan and B. T. Meggitt, *Optical Fiber Sensor Technology*, vol. 3. The Netherlands: Kluwer Academic Publishers, 1999.
- [85] A. J. Rogers, "Distributed optical fiber sensing," 1991, vol. 1510, pp. 2–24.
- [86] D. L. Philen, I. A. White, J. F. Kuhl, and S. C. Mettler, "Single-mode fiber OTDR: Experiment and theory," *IEEE J. Quantum Electron.*, vol. 18, no. 10, pp. 1499–1508, 1982.

- [87] D. M. Spirit and L. C. Blank, "Raman-assisted long-distance optical time domain reflectometry," *Electronics Letters*, vol. 25, no. 25. Institution of Engineering and Technology, pp. 1687–1689, 1989.
- [88] X. Bao, D. J. Webb, and D. A. Jackson, "32-km distributed temperature sensor based on Brillouin loss in an optical fiber," *Opt. Lett.*, vol. 18, no. 18, pp. 1561–1563, 1993.
- [89] K. S. C Kuang and W. J. Cantwell, "Use of conventional optical fibers and fiber Bragg gratings for damage detection in advanced composite structures: A review," *Appl. Mech. Rev.*, vol. 56, no. 5, pp. 493–513, 2003.
- [90] H. Guo, G. Xiao, N. Mrad, and J. Yao, "Fiber Optic Sensors for Structural Health Monitoring of Air Platforms," *Sensors*, vol. 11, no. 4. 2011.
- [91] K. O. Hill, Y. Fujii, D. C. Johnson, and B. S. Kawasaki, "Photosensitivity in optical fiber waveguides: Application to reflection filter fabrication," *Appl. Phys. Lett.*, vol. 32, no. 10, pp. 647–649, 1978.
- [92] B. S. Kawasaki, K. O. Hill, D. C. Johnson, and Y. Fujii, "Narrow-band Bragg reflectors in optical fibers," *Opt. Lett.*, vol. 3, no. 2, pp. 66–68, 1978.
- [93] G. Meltz, W. W. Morey, and W. H. Glenn, "Formation of Bragg gratings in optical fibers by a transverse holographic method," *Opt. Lett.*, vol. 14, no. 15, pp. 823–825, 1989.
- [94] K. O. Hill, B. Malo, F. Bilodeau, D. C. Johnson, and J. Albert, "Bragg gratings fabricated in monomode photosensitive optical fiber by UV exposure through a phase mask," *Appl. Phys. Lett.*, vol. 62, no. 10, pp. 1035–1037, 1993.
- [95] Y.-J. Rao, "In-fibre Bragg grating sensors," *Meas. Sci. Technol.*, vol. 8, no. 4, p. 355, 1997.
- [96] FIBERPRO, "High-speed FBG Interrogation System, SFI-710." [Online]. Available: <http://www.fiberpro.com>.
- [97] J. L. Devore, *Probability and Statistics for Engineering and the Sciences*. Brooks/Cole Cengage Learning, 2012.
- [98] P. F. Ribeiro, C. A. Duque, P. M. Ribeiro, and A. S. Cerqueira, *Power Systems Signal Processing for Smart Grids*. John Wiley & Sons, 2013.
- [99] P. Shrestha, J. H. Kim, Y. Park, and C. G. Kim, "Impact localization on composite structure using FBG sensors and novel impact localization technique based on error outliers," *Compos. Struct.*, vol. 142, pp. 263–271, 2016.
- [100] P. Shrestha, Y. Park, and C.-G. Kim, "Low velocity impact localization on composite wing structure using error outlier based algorithm and FBG sensors," *Compos. Part B Eng.*, 2016.
- [101] C. C. Aggarwal, "An Introduction to Outlier Analysis," in *Outlier Analysis*, New York: Springer, 2013, pp. 1–40.
- [102] K. Worden, G. Manson, and N. R. J. Fieller, "Damage detection using outlier analysis," *J. Sound Vib.*, vol. 229, no. 3, pp. 647–667, 2000.
- [103] S. García, J. Luengo, and F. Herrera, *Data Preprocessing in Data Mining*, vol. 72. New York: Springer International Publishing, 2015.
- [104] R. R. Wilcox, *Fundamentals of Modern Statistical Methods: Substantially Improving Power and Accuracy*. Springer New York, 2010.
- [105] R. R. Craig and A. J. Kurdila, *Fundamentals of Structural Dynamics*, 2nd ed. Hoboken, N.J.: John Wiley, 2006.

Acknowledgements

First and foremost, I offer my humble and sincere gratitude to God for all your blessings on me. Everything that I have done so far has only been possible because of your divinity working through me and through the wonderful people that surround me who constantly guide me and steer me in the right direction.

I would like to express my sincere gratitude to my supervisor, Prof. Chun-Gon Kim, for the constant encouragement, motivation, generous guidance and support which enabled me to overcome the many challenges and difficulties that one encounters during the course of the PhD journey. I am most grateful to him for imparting his knowledge and expertise to me which served as a profound cornerstone of my PhD research and has thus made it possible to complete this dissertation. I would also like to thank the dissertation committee members, Prof. Jae-Hung Han, Prof. Jung-Ryul Lee, Dr. Il-Bum Kwon, and Dr. Dong-Hoon Kang, for their valuable comments and suggestions. Also, I would also like to thank KAIST for providing me with the scholarship to pursue PhD degree in Aerospace Engineering.

I have been very fortunate to have met many kind, friendly and warm-hearted personalities who have helped me in one way or the other while I was pursuing my PhD for the past four years at Smart Structures and Composites Laboratory (SSCL). To begin with, I am very thankful for the advice, support and help given to me by the SSCL alumni, Dr. A. Baluch, Dr. W. H. Choi, Dr. J. H. Shin, Dr. T. H. Song, Dr. G. S. Son, Mr. N. J. Young, and Mr. E. Jurado. I would also like to thank the current SSCL members, Ms. M. Y. Park, Mr. Y. H. Kim, Mr. Y. W. Nam, Mr. C. H. Choi, Mr. J. H. Choi, Mr. S. Kumar, Mr. H. O. Park, Mr. J. S. Shin, Mr. M. S. Jang, Mr. F. Wolff, and Mr. V. A. Ankem, for their assistance and support in the day-to-day SSCL activities. I would like to express my heartfelt gratitude and sincere appreciation to the SSCL Fiber Optics Team's past and present members, Dr. J. H. Kim, Mr. Y. Park, Mr. Y. Y. Kim, Mr. H. J. Kwon, and Mr. H. S. Kwon, for their valuable insights and support. I am most grateful to you all for kindly assisting me whenever I needed help.

I would also like to thank Dr. B. Nakarmi, Dr. P. Yadav & family, Mr. D. Liutel, Dr. K. Shrestha, Mr. & Mrs. Chhetri, Mr. S. Manandhar, Mr. K. Dhital, Mr. M. Shrestha and Mr. B. Bhattarai, for providing a home-like atmosphere at KAIST and making my stay here much more joyful and pleasant than I could have wished for. Also, I am very thankful to the many friends and colleagues without whom my PhD journey at KAIST would not have been the same.

A special thanks to my loving parents, Prachanda Man Shrestha and Radhika Dhonju Shrestha, and my adoring sister, Pratibha Shrestha Baidhya, who always keep telling me that there is nothing that I cannot accomplish if I put my mind to it. Thank you for always being there for me, boosting my spirit, guiding me towards new frontiers and helping me achieve what otherwise would have been distant. Also, huge thanks to my *mama*, Karma Lal Dhonkaji, *fufu*, Ambika Shrestha, *vinaju*, Saroj Baidhya, and all family and relatives for always being supportive and encouraging. Last but not the least, I would like to thank Mr. Nimananda Rijal, Mrs. Nilima Bakaya, Mr. Easo Oommen, Mrs. Sakuringwa, Mr. Ganapathy and many other teachers who put their faith in me and encouraged me to do better.

Curriculum Vitae



Name : Pratik Shrestha
Date of Birth : August 4, 1990
Nationality : Nepalese
Address : Maijubahal, Chabahil, Kathmandu, Nepal

Education

2006. 9 – 2010. 6 : Bachelors in Aeronautical Engineering
Nanjing University of Aeronautics and Astronautics
Nanjing, Jiangsu, People's Republic of China
2011. 2 – 2013. 2 : MSc in Aerospace Engineering
Department of Aerospace Engineering
Korea Advanced Institute of Science and Technology
Daejeon, Republic of Korea
2013. 3 – 2017. 2 : PhD in Aerospace Engineering
Department of Aerospace Engineering
Korea Advanced Institute of Science and Technology
Daejeon, Republic of Korea

Research Experience

2011. 2 – 2013. 2 : Graduate Research Assistance
Intelligent Systems and Vibration Control Lab., KAIST
2013. 3 – 2017. 2 : Graduate Research Assistance
Smart Structures and Composites Lab., KAIST

Achievements

- The Best Presentation Award, 2016: 10th Asian-Australian Conference on Composite Materials, Busan
- Outstanding Research Thesis, 2015: International Academic Conference for Graduates, NUAA, Nanjing
- Excellence Paper Award, 2015: 10th Korea-Japan Joint Symposium on Composite Materials, Jeonju
- KAIST Scholarship, 2013 ~ 2017: Scholarship for Doctoral Program
- KAIST Scholarship, 2011 ~ 2013: Scholarship for Master's Program
- Honor of Excellent Performance of Undergraduate International Students, 2008-2009
- Nanjing University of Aeronautics and Astronautics: 2nd Prize Scholarship for Year 2008-2009
- Nanjing University of Aeronautics and Astronautics: 3rd Prize Scholarship for Year 2007-2008
- Nanjing University of Aeronautics and Astronautics: 3rd Prize Scholarship for Year 2006-2007

Research Publications

Theses

- 1) **Pratik Shrestha**, “A Parametric Study on Flutter Characteristics of a Folding Wing,” MSc Thesis, KAIST, Feb. 2013. (Supervisor: Prof. In Lee)
- 2) **Pratik Shrestha**, “Novel Error Outlier Method and FBG Sensor Based Real-Time Low Velocity Impact Monitoring of Composite Wing Structure,” PhD Thesis, KAIST, Feb. 2017. (Supervisor: Prof. Chun-Gon Kim)

Journal Papers

- 1) S.-W. Kim, E.-H. Kim, M.-S. Rim, **P. Shrestha**, I. Lee, and I.-B. Kwon, “Structural performance tests of down scaled composite wind turbine blade using embedded fiber Bragg grating sensors,” Int. J. Aeronaut. Sp. Sci., vol. 12, no. 4, pp. 346–353, 2011.
- 2) **P. Shrestha**, M. S. Jeong, I. Lee, J. S. Bae, and K. N. Koo, “Flutter characteristics of a morphing flight vehicle with varying inboard and outboard folding angles,” Int. J. Aeronaut. Sp. Sci., vol. 14, no. 2, pp. 133–139, 2013.
- 3) **P. Shrestha**, J. H. Kim, Y. Park, and C. G. Kim, “Impact localization on composite wing using 1D array FBG sensor and RMS/correlation based reference database algorithm,” Compos. Struct., vol. 125, pp. 159–169, 2015.
- 4) J.-H. Kim, Y. Park, Y.-Y. Kim, **P. Shrestha**, and C.-G. Kim, “Aircraft health and usage monitoring system for in-flight strain measurement of a wing structure,” Smart Mater. Struct., vol. 24, no. 10, pp. 1–12, 2015.
- 5) J.-H. Kim, Y. Park, Y.-Y. Kim, **P. Shrestha**, and C.-G. Kim, “Aircraft health and usage monitoring system for in-flight strain measurement of a wing structure,” Smart Mater. Struct., vol. 24, no. 10, pp. 1–12, 2015.
- 6) Y. Y. Kim, J. H. Kim, Y. Park, **P. Shrestha**, H. J. and Kwon, and C. G. Kim, “Low-speed impact localization on a stiffened composite structure using reference data method,” Compos. Res., vol. 29, no. 1, pp. 1–6, 2016.
- 7) **P. Shrestha**, J. H. Kim, Y. Park, and C. G. Kim, “Impact localization on composite structure using FBG sensors and novel impact localization technique based on error outliers,” Compos. Struct., vol. 142, pp. 263–271, 2016.
- 8) **P. Shrestha**, Y. Park, and C.-G. Kim, “Low velocity impact localization on composite wing structure using error outlier based algorithm and FBG sensors,” Compos. Part B Eng., 2016.

International Conferences

- 1) J. H. Kim, **P. Shrestha**, Y. Park, and C. G. Kim, "Application of fiber Bragg grating sensors in light aircraft: ground and flight test", OFS2014 23rd International Conference on Optical Fiber Sensors, International Society for Optics and Photonics, 91578V, 2014.
- 2) J. H. Kim, **P. Shrestha**, Y. Park, and C. G. Kim, "Load monitoring of full-scale composite wing structure using fiber Bragg grating sensors", Advances in Structural Health Management and Composite Structures, August 27-29, 2014, Chonbuk National University, Jeonju, South Korea, 2014.
- 3) **P. Shrestha**, J. H. Kim, Y. Park, and C. G. Kim, "Use of FBG sensors for impact localization on composite structure", Advances in Structural Health Management and Composite Structures, August 27-29, 2014, Chonbuk National University, Jeonju, South Korea, 2014.
- 4) Y. Park, J. H. Kim, **P. Shrestha**, H. J. Kwon, and C. G. Kim, "Composite material monitoring under LEO thermal cycling using multi-layer embedded FBG sensor array", Jeonju, Korea, Oct 28-30, 2015.
- 5) **P. Shrestha**, J. H. Kim, Y. Park, and C. G. Kim, "Impact monitoring on composite structures using FBG sensors", The 10th Korea-Japan Joint Symposium on Composite Materials", Jeonju, Korea, Oct 28-30, 2015.
- 6) **P. Shrestha**, J. H. Kim, Y. Park, and C. G. Kim, "Low velocity impact localization on composite wing under simulated operational conditions using FBG sensors", Nanjing, China, Nov 19-20, 2015.
- 7) **P. Shrestha**, J. H. Kim, Y. Park, and C. G. Kim, "Application of 1D array FBG configuration for impact localization on composite wing under simulated noise", 7th Asia-Pacific International Symposium on Aerospace Technology, Queensland, Australia, Nov 25-27 2015.
- 8) Y. Park, **P. Shrestha**, H. S. Kwon, J. H. Kim, H. J. Kwon and C. G. Kim, "Effect of tubing material on conventional and thin FBG sensor for embedded environment impact monitoring of CFRP composites", in Proc. SPIE 9805, Health Monitoring of Structural and Biological Systems 2016, 98052T, April 1, 2016.
- 9) J. H. Kim, Y. Park, **P. Shrestha**, and C. G. Kim, "Impact localization on stiffened composite panel using FBG sensors", Asian Joint Symposium on Aerospace Engineering 2016, May, 2016.
- 10) **P. Shrestha**, Y. Park and C. G. Kim, "Low-velocity impact monitoring of aircraft wing structure using novel error outlier impact localization algorithm", KAIST-NUAA Symposium, Daejeon, Korea, June 2, 2016.
- 11) Y. Park, **P. Shrestha**, H. S. Kwon and C. G. Kim, "Investigation of multi-layer embedded FBG sensor response under simulated LEO environment exposure", ACCM10, Busan, Oct, 2016.
- 12) **P. Shrestha**, Y. Park and C. G. Kim, "Impact monitoring of composite wing using error outlier assessment based impact localization algorithm and FBG sensors", ACCM10, Busan, Oct, 2016.

Domestic Conferences

- 1) **P. Shrestha**, M. S. Jeong, and I. Lee, “Effect of hinge stiffness on flutter characteristics of flat plate wing with flap”, The Korean Society for Aeronautical and Space Sciences Spring 2012 Conference, High1 Resort, Gangwon land, Korea, 2012.
- 2) **P. Shrestha**, M. S. Jeong, E. H. Kim, I. Lee, and J. S. Bae, “Effect of inboard and outboard folding angles on aeroelastic characteristics of a folding wing”, The Korean Society for Aeronautical and Space Sciences Fall 2012 Conference, Ramada Plaza, Jeju, Korea, 2012.
- 3) J. H. Kim, **P. Shrestha**, Y. Park, and C. G. Kim, “Full-scale static test of small aircraft wing structure using low-speed FBG interrogator”, Korea Institute of Military Science and Technology, Jeju, Korea, July 4-5, 2013.
- 4) **P. Shrestha**, J. H. Kim, Y. Park, and C. G. Kim, (2014), “Impact localization on composite structure through use of FBG sensors and reference database impact localization algorithm”, The Korean Society for Aeronautical and Space Sciences Spring 2014 Conference, Wonju, Korea, 2014.
- 5) **P. Shrestha**, J. H. Kim, Y. Park, C. G. Kim, “Impact localization on composite structure under simulated operational noise using FBG sensors and reference database algorithm”, The Korean Society for Aeronautical and Space Sciences Fall 2014 Conference, Jeju, Korea, November 19-21, 2014.
- 6) **P. Shrestha**, J. H. Kim, Y. Park, and C. G. Kim, “Composite structure damage detection using FBG sensor and reference database algorithm”, The Korean Society for Aeronautical and Space Science Spring 2015 Conference, High1 Resort, Gangwon land, South Korea, April 24, 2015.
- 7) Y. Park, H. S. Kwon, **P. Shrestha**, and C. G. Kim, “Experimental study on LEO environment exposure and impact detection using CFRP composite embedded FBG sensors”, 2016 Annual Fall Conference of Korean Society for Nondestructive Testing, Daejeon, Korea, November 3, 2016.
- 8) **P. Shrestha**, Y. Park, and C. G. Kim, “Error outlier method and FBG sensor based low velocity impact localization”, 2016 Annual Fall Conference of Korean Society for Nondestructive Testing, Daejeon, Korea, November 3, 2016.

